A NUMERICAL STUDY OF MICROFLUIDIC DROPLET MOTIONS IN PARALLEL-PLATE ELECTROWETTING-ON-DIELECTRIC (EWOD) DEVICES

by

YIN GUAN

Presented to the Faculty of the Graduate School of
The University of Texas at Arlington in Partial Fulfillment
of the Requirements
for the Degree of

DOCTOR OF PHILOSOPHY

THE UNIVERSITY OF TEXAS AT ARLINGTON
May 2015

Acknowledgements

First and foremost I would like to express my deepest appreciation to my supervising professor, Dr. Albert Y. Tong, for his valuable guidance and great patience during my time in graduate school. I am grateful for him introducing me this great research topic and offering me his trust on this challenging project. I really appreciate his countless hours on discussing my research and his generous help on writing journal papers and this dissertation. I am also very thankful for him being a role model in my life, helping me overcome my own weaknesses through all these years so I can grow up and become a strong man. His genuine passion for scientific research will always be an inspiration in my future career.

Next, I would like to thank my PhD committee members, Dr. Ratan Kumar, Dr. Chaoqun Liu, Dr. Cheng Luo and Dr. Hyejin Moon for their valuable time on reading my dissertation and offering me helpful advices on this work. I especially appreciate Dr. Moon for her broad knowledge on this EWOD topic and her constructive suggestions on my research cases. I also appreciate my group mates, Ashraful Islam, Peter Martinez and Vimal Ramanuj for their time and effort on discussing the numerical program and my research with me. In particular, I thank Jagath Yaddessalage for his help on droplet dispensing cases and his effort in providing useful experimental data.

Moreover, I am really grateful for the assistantship offered by the Mechanical and Aerospace Engineering Department at UTA. This support is essential for me to maintain financial security in all these years without which I could not have completed this work.

Finally, I would also like to thank my family for their constant support, understanding and care.

April 3, 2015

Abstract

A NUMERICAL STUDY OF MICROFLUIDIC DROPLET MOTIONS IN PARALLEL-PLATE ELECTROWETTING-ON-DIELECTRIC (EWOD) DEVICES

Yin Guan, PhD

The University of Texas at Arlington, 2015

Supervising Professor: Albert Y. Tong

Microscale water droplet motions in parallel-plate electrowetting-on-dielectric (EWOD) devices including transport, splitting, merging and dispensing have been numerically studied. The transient governing equations for the microfluidic flow are solved by a finite volume scheme with a two-step projection method on a fixed computational domain. The interface between liquid and gas is tracked by a coupled level set and volume-of-fluid (CLSVOF) method. A continuum surface force (CSF) model is employed to model the surface tension at the interface. Contact angle hysteresis which is an essential component in EWOD modeling is implemented together with a simplified model for the viscous stresses exerted by the two plates at the solid-liquid interface.

The accuracy of the numerical model has been validated with published experimental data and excellent agreement has been achieved between the numerical and experimental results for all four operations. The physics of droplet motions within the parallel-plate EWOD devices has been thoroughly examined. For the transport process, special attention has been focused on some localized areas near the ON/OFF electrode border where the transport process is primarily influenced. A dimensionless curvature has been introduced and a critical value has been identified beyond which the droplet would split during the transport. A parametric study has been performed in which the effects of several crucial parameters including initial droplet shape, static contact angles, contact angle hysteresis, viscous stress, channel height and electrode size on the transport process have been revealed. For the splitting and merging processes, a parametric study has been performed in which the effects of channel height and droplet physical properties on the droplet motions have been investigated. The dispensing process of micro droplets in parallel-plate EWOD devices with various reservoir designs has been simulated. The dispensing mechanism has been carefully examined and droplet volume inconsistency for each design has been investigated. Several key elements which directly affect volume inconsistency have been identified.

Table of Contents

List of Illustrations

List of Tables

Chapter 1

Introduction

1.1 Motivation

The concept of digital microfluidics emerged in the 1990s and it has experienced rapid development due to the remarkable progress of various advanced microelectromechanical systems (MEMS) and Lab-on-a-chip (LOC) devices [1-3]. Numerous well-designed microfluidic devices have been developed to deliberately manipulate the liquid motion at the microscale. Over the past few decades, the investigation of microfluidic liquid behavior has become a popular scientific research field in which the study of discrete droplet motion in microfluidic devices has considerably developed as a significant component of digital microfluidic applications.

For droplets in microscale, surface tension force becomes much more dominant than other physical forces such as inertial force, viscous stress, gravity force *etc.* The surface tension force can be used as the driving mechanism of droplet motion in which it plays the most significant role in the overall fluid behavior. During the past ten years, a number of physical mechanisms have been successfully employed to alter the surface tension force at the gas-liquid interface, which consequently creates a pressure difference across the droplet boundary and serves as the driving force for the droplet motion. These mechanisms include electrostatic force [4], thermocapillary effect [5, 6], electrochemical gradient [7], dielectrophoresis [8], magnetic field [9] and electrowetting effect [10, 11].

The use of electrowetting effect as the driving mechanism for microfluidic droplet motion arose in the early 2000s. Electrowetting refers to the phenomenon whereby the wetting property of a conductive liquid droplet is modified with an applied electrical field at the triple contact line [12-16]. This innovative technique has been widely applied in various micro droplet operations such as transport, splitting, merging and dispensing [2, 10, 11, 17-22], liquid lifting along a vertical column [23], droplet spreading on single-plate EWOD device [24, 25] *etc*. Advanced applications such as microinjection [26] and mass spectrometry [27] are other examples of its outstanding versatility. It has been discovered that the effectiveness of electrowetting devices can be improved by coating the bottom electrodes with a thin dielectric layer [28-30], which leaded to the increasing utilization of electrowetting-on-dielectric (EWOD) devices on microfluidic droplet motions in recent years. In fact, EWOD device has been proven to be an extremely versatile tool and one of the most flexible physical techniques to control the fluid in the microscale since it is capable of manipulating tiny droplet solely by applying appropriate amount of electrical charges at the droplet boundary. With the help of EWOD device, a great deal of effort in constructing complicated physical parts and other micromechanical structures can be saved by simply building single circuit boards and controlling the chips with programmable electric signals.

However, even though the studies of EWOD-based microfluidic droplet motions have been conducted for years, the important physics involved in the droplet behavior is still not fully understood. Specifically, very few explanations have been offered for the commonly observed phenomena, such as the droplet splitting during the transport when the electrical voltage is sufficiently high; the droplet displaying different shapes during the transport as the channel height varies; a satellite droplet formed at the end of the splitting process when the channel height is too small; better droplet volume uniformity achieved in some dispensing devices than in others *etc*. Due to the fact that the droplet experiences rapid displacements and complicated geometrical changes which occur on scale of space and time that are difficult and may even be impossible to perform, it is often challenging to perform experimental study to capture clear droplet motion images at crucial time instants. Other issues including arduous work of EWOD system fabrications and droplet volume measurement are also impediments to exploring the mechanism of droplet motions. Numerical methods, on the other hand, can provide vital information such as the pressure and velocity profiles within the liquid at crucial time instants, which may serve as an excellent alternative for systematically analyzing the droplet behavior. Moreover, clear droplet image and reliable volume data can be directly extracted from the numerical results, which are not readily available in experiments or other means.

The objective of the present study is to numerically investigate four fundamental microfluidic motions in parallel-plate EWOD devices which include droplet transport, splitting, merging and dispensing from a large liquid reservoir. The results obtained from the numerical simulations are compared with the corresponding experimental data reported in the literature [20, 31]. The fluid dynamics and physics of droplet motions are thoroughly examined. A parametric study is performed for transport, splitting and merging processes in which the effects of several key parameters on droplet motions are investigated. The dispensing mechanism is carefully examined for three different reservoir designs. The volume inconsistency of generated droplets is studied for each design and several key elements which directly affect volume inconsistency are identified.

1.2 Organization of Thesis

This thesis is organized as followed. In Chapter 2, the development of fundamental electrowetting-induced microfluidic droplet motions over the last decade is briefly reviewed. The physics of microfluidic droplet motions in parallel-plate EWOD device is described in Chapter 3. A literature review of interface tracking methods and surface tension modeling techniques is provided in Chapter 4. Mathematical formulations of the current numerical EWOD model are presented in Chapter 5 in which the governing equations, interface tracking schemes, surface tension modeling algorithms and the implementation of contact angle hysteresis effect are discussed. In Chapter 6, the numerical results of all four droplet operations are reported in conjunction with the comparison between the numerical results and the corresponding experimental data. The physics of droplet motions is fully examined and the effects of several key parameters on the droplet behavior are demonstrated. Finally, conclusions and some potential future research topics are given in Chapter 7.

Chapter 2

Electrowetting-induced Microfluidic Droplet Operations

2.1 Droplet Transport

Experimental studies of droplet transport in parallel-plate electrowetting-based microfluidic systems have been carried out over the last decade [10, 11, 17, 31-34]. Pollack *et al*. [32] performed a preliminary experimental study on electrowetting-induced discrete micro droplet transport using KCl solution as the working liquid. It was found that a voltage larger than 30V was required to initiate the droplet movement and the voltage was mainly used to overcome the contact angle hysteresis effect. Pollack *et al*. [10] extended that study to four fundamental micro droplet operations including transport, splitting, merging and dispensing with the same liquid and LOC devices. The transport process was successfully conducted with an average velocity exceeding 100mm/s obtained at about 60V beyond which the droplet was found to split during the transport. Cho *et al*. [11] later conducted experiments on deionized (DI) water droplet transport in a parallel-plate EWOD device. Micro droplets were transported after being dispensed from a large liquid reservoir. It was discovered that the minimum voltage for initiating the droplet motion was only 18V and that the average transport speed could go up to 250mm/s with a higher AC voltage. Recently, Yaddessalage [31] carried out EWOD-based droplet transport experiments in a parallel-plate LOC device with DI water as the working liquid. The effect of several parameters including working surface smoothness, electrode size and electrode geometry on the transport speed were examined. It was found that the transport speed was dependent on the working surface material and that a larger transport speed could be obtained when the electrode had a larger size or when the electrode was separated into several strips with equal size.

Due to the great difficulty of conducting experiments at such small scales, micro droplet transport process in parallel-plate electrowetting device has also been simulated with a number of numerical models [22, 35-40]. Mohseni *et al*. [36] carried out numerical simulations of droplet transport in parallel-plate microchannels with the gas-liquid interface tracked by the Volume-of-Fluid (VOF) method. It was reported that the transport speed increased as the channel height became smaller and that the droplet would split during the transport if the actuation voltage was sufficiently high. An energy-based computational algorithm was formulated by Bahadur and Garimella [37] for studying the droplet motion in parallel-plate electrowetting-based fluid actuation systems. It was found that the transport speed was significantly affected by the actuation voltage but had negligible dependence on the channel height. A coupled-electro-hydrodynamic numerical scheme was developed by Arzpeyma *et al*. [38] for investigating the transport process induced by the electrowetting force. It was shown that the contact angle hysteresis was essential for the modeling accuracy and that the transport speed increased with the applied voltage. Keshavarz-Motamed *et al*. [40] recently performed a computational study on droplet transport process in parallel-plate microchannels with a molecular-kinetic energy model. The dynamic behavior of the triple contact line was investigated and the dynamic contact angles during the transport process were calculated. It was discovered that on average both the advancing and receding contact angles had a deflection of 8° compared to the static contact angle.

Several analytical models were also proposed for examining electrowetting-based fluid behavior in parallel-plate microfluidic devices [20, 37, 41]. Governing equations of the droplet motion were theoretically derived with the effects of electrical voltage, viscous stress, contact angle hysteresis, contact line friction force and other relevant terms included.

2.2 Droplet Splitting

Unlike the droplet transport process in which only two electrodes are required, droplet splitting takes at least three electrodes to perform. In the initial condition, a droplet is often placed at the center of the middle electrode with part of the liquid occupying the side electrodes symmetrically. As soon as the side electrodes are activated simultaneously, the droplet interface keeps moving sideways until the droplet is split into two smaller ones with similar sizes staying on the activated electrodes.

Droplet splitting is also one of the fundamental microfluidic operations which have been studied for years. Pollack *et al*. [10] were among the early researchers who conducted experiments on controlled droplet splitting process in a parallel-plate LOC device based on the electrowetting effect. The same experiments were later carried out by Cho *et al*. [11] with similar results reported. It was discovered that the splitting process became more difficult with smaller electrode size and that the droplet failed to split when the channel height was increased to 0.3mm. The physics of splitting process was theoretically analyzed by investigating the pressure difference across the droplet boundary and the explanation for the failure of splitting was subsequently provided. Inspired by Pollack *et al*. [10] and Cho *et al*. [11], Jang *et al*. [17] performed both numerical simulations and experiments for droplet splitting with good agreement achieved between the numerical and experimental results. Walker and Shapiro [19] numerically modeled the splitting process in a parallel-plate EWOD device with the level set method and demonstrated that contact angle saturation and hysteresis were essential for matching the shape and time scale of the simulation with the experiment. Walker *et al*. [20] extended that study with an improved numerical formulation which included a contact line force threshold model for the contact line hysteresis and pinning effects. The splitting processes of both water and glycerin droplets were numerically performed which showed good agreement with the prior experimental data.

2.3 Droplet Merging

Another crucial branch of parallel-plate electrowetting-based microfluidic droplet operations is droplet merging. The investigation of the merging process is very essential for the broad microfluidic droplet applications, especially for the biomedical fields in which the mixing of micro biomedical essays is practically a daily task. Similar to the splitting process, droplet merging takes at least three electrodes to perform. Initially, two droplets are often placed symmetrically on the left and right electrodes with part of its volume occupying the electrode in the middle. As soon as the middle electrode is activated, the droplets move towards each other until they collide and merge into a large one. In general, the merging process consists of a droplet transport process in which the two droplets have no impact on each other and a subsequent merging process as soon as the two droplets collide. It is understood that the shape and speed of the two droplets at the moment of collision play a significant role in the merging process including the merging speed as well as the final shape of merged droplet.

The investigations of droplet merging process are often conducted and reported together with the splitting operations due to the similarities of their experimental devices and microfluidic behavior. However, the studies of merging process are relatively scarce in the literature compared to the other three operations. In recent years, experiments of micro droplet merging process induced by the electrowetting effect have been successfully carried out with a variety of electrowetting-based LOC systems [10, 11, 17, 20]. Walker *et al*. [20] conducted a numerical study on water droplet merging process in which the fluid dynamics of the droplet are modeled by the Hele-Shaw type of equations

[42] with the contact line hysteresis and pinning effects accounted for by a contact line force threshold model. The results obtained from the numerical simulations demonstrated excellent agreement with the experimental data.

2.4 Droplet Dispensing

Microfluidic droplet operations with high volume precision is of paramount importance for many scientific applications such as chemical synthesis, compound separation, drug discovery and quantitative analysis of biomedical assays [43, 44]. The volume precision of a series of micro droplets can be evaluated by droplet volume inconsistency, which is also referred to as droplet volume reproducibility in some literature [41, 43, 45] and defined as the ratio of the standard deviation of a series of droplets to their mean value. It was reported that the inconsistency is preferably between ±5% and needs to be controlled to within ±2% or even less for some particular biomedical requirements [43].

As one of the fundamental microfluidic droplet operations, the investigation of droplet dispensing, which refers to the process of aliquoting a larger volume of liquid into smaller unit droplets for further actions, has been carried out for years due to the increasing demand for droplet volume uniformity [2, 10, 11, 17, 18, 21, 41, 45-47].

Pollack *et al*. [10] were among the early researchers who conducted experiments on micro droplet dispensing in parallel-plate electrowetting-based LOC systems. It was shown that droplets of similar sizes were generated from a large sample drop in the reservoir. Similar dispensing experiment was later performed by Cho *et al*. [11] with deionized (DI) water as the working liquid. Droplets were successfully dispensed from a liquid reservoir in a parallel-plate EWOD device which consists of two small electrodes alongside the main dispensing path. It was found that without these two side electrodes the pinch-off location would not be fixed and the droplet sizes would consequently not be consistent. An experimental method combining electrowetting actuation and built-in capacitance feedback was developed by Ren *et al*. [41] for droplet dispensing from a self-contained LOC device using KCl solution as the working liquid. Smaller volume inconsistency was obtained compared to devices without capacitance feedback and the inconsistency was found to increase with droplet viscosity and production rate. Berthier *et al*. [45] numerically modeled droplet dispensing process based on the surface energy minimization approach. It was demonstrated that decent volume inconsistency could be achieved when the cutting and generating electrodes were of the same size. Fair [2] summarized the recent development of electrowetting-based digital microfluidics and LOC applications. The dispensing mechanism was also examined by investigating the pressure differences across the liquid boundary at critical dispensing stages. It was reported that fewer cutting electrodes were needed for successful dispensing when the device had a smaller channel height and a larger generating electrode size. A real-time feedback control EWOD system was developed by Gong and Kim [18] for on-chip droplet dispensing experiments, in which droplet uniformity was notably improved compared to devices with external pump or open loop control system. Wang *et al*. [21] studied water droplet dispensing from an EWOD-based microfluidic device. It was illustrated that the length of the neck in the cutting stage played a significant role in the volume of generated droplet. Thus, smaller volume inconsistency could be acquired when the cutting electrode was of a small size. Yaddessalage [31] recently carried out experimental studies on micro droplet dispensing from parallel-plate EWOD devices with three different reservoir designs. It was reported that better volume uniformity could be achieved by shortening the length of the neck in the cutting stage.

Chapter 3

Microfluidic Droplet Motion in Parallel-plate EWOD Device

3.1 Parallel-plate EWOD Device

Electrowetting-on-dielectric (EWOD) device consists of a configuration in which the working liquid and actuation electrodes are separated by an insulating layer. A typical experimental parallel-plate EWOD device is given in Figure 3-1 and the schematics of the top and cross-sectional views of a parallel-plate EWOD device are shown in Figure 3-2. Note that the figure is not to scale with a much narrower channel height in the actual device. It consists of two parallel plates with the droplet sandwiched in between. The top electrode is one whole piece which remains grounded at all time while the two disjointed square-shaped electrodes at the bottom can be switched ON and OFF independently as needed.

There are two thin layers one each on the top and bottom plates which are used as the hydrophobic coating between the working liquid and electrodes. These hydrophobic layers are often manufactured with low-energy solid surfaces such as Cytop® and Teflon® due to their property of displaying low contact angle hysteresis values for various kinds of liquid. In other words, liquid motion can be easily initiated with a low electrical actuation on these surfaces.

The dielectric layer on the bottom plate is a thin insulating film which separates the hydrophobic layer from the bottom electrodes and sustains the high electric field at the surface. A thin dielectric layer with high dielectric constant is generally preferred in order to lower the initiating voltage for droplet motion. It has been discovered that the electrowetting device embedded with a dielectric layer allows a larger contact angle change upon the application of electrical voltage and has excellent reversibility and compatibility compared to the traditional device in which the droplet is in direct contact with the conductive surface. More details about the parallel-plate EWOD device can be found in [11, 14, 30, 31, 48].

3.2 Contact Angle Actuation

When a liquid droplet is placed on a plane surface, the relation between the equilibrium contact angle θ and the surface tensions at the three-phase contact line is given by the Young's equation:

$$\sigma_{SG} = \sigma_{SL} + \sigma_{LG} cos\theta \tag{3-1}$$

where subscripts SG, SL and LG denote solid-gas, solid-liquid and liquid-gas interfaces, respectively. This is basically a result of force balance at the triple contact line which was discovered by Lippmann over a century ago [12]. It was found that the capillary force at the solid-liquid interface can be modified by the application of electrostatic charges at the liquid boundary. This modified surface tension at the interface is given by the Lippmann equation as:

$$\sigma_{SL}(V) = \sigma_{SL_{|V=0}} - \frac{C}{2} V^2 \tag{3-2}$$

where C is the specific capacitance of the dielectric layer and V the applied voltage. This electro-capillary phenomenon was not put into practice in electrowetting until Matsumoto and Colgate [49] who designed a microelectrical device and studied the microactuation for fluid systems driven by electrical control of surface tension. This electromechanical effect was later substantiated by various applications of EWOD systems over the last decade. By incorporating Equations (3-1) and (3-2), it can be shown that the contact angle θ at the three-phase contact line is reduced by the addition of an electrical potential which leads to the Young-Lippmann's equation given by [11, 14, 17, 37]:

$$cos\theta(V) = cos\theta_0 + \frac{\epsilon_0\epsilon}{2\sigma_{LG}t}V^2 \tag{3-3}$$

where θ is the contact angle at the triple contact line with non-zero electrical potential, θ_0 the equilibrium contact angle with zero potential, ϵ_0 the permittivity of vacuum, ϵ the dielectric constant of the dielectric layer and t the thickness of the dielectric layer.

3.3 Contact Angle Saturation

The Young-Lippmann equation is reasonably accurate in predicting the contact angle at low voltage. However, it has been discovered that the equation fails after the voltage reaches a certain threshold beyond which the contact angle θ demonstrates only little variation. This effect is referred to as contact angle saturation and has been discussed in a variety of electrowetting problems [11, 14, 24, 50-52]. An example of the contact angle saturation is shown in Figure 3-3, which displays a contact angle saturation of about 80° at around 22V.

To date, no consensus has been reached about the mechanism of contact angle saturation. A number of explanations have been given for this interesting phenomenon in which the real contact angles deviate from the predicted values from the Young-Lippmann equation when a voltage exceeding the critical value is applied [50, 53-56]. Vallet *et al*. [53] discovered that for the liquid with low conductivity the triple contact line was not stable at high voltage, which leaded to the formation of satellite droplets at the neighborhood of the triple contact line and consequently the saturation effect. The same phenomenon was also observed by Mugele and Herminghaus [54] who reproduced the experiment with mixtures of water and glycerol. It was reported that the balance between the surface tension force and the electrostatic repulsion would be upset if the voltage was greater than the threshold value, which caused the formation of satellite droplets.

Verheijen and Prins [55] presented that the surface of insulating layers were charged when the electrical voltage exceeded the threshold value. As a result, the immobilized charge carriers in the insulating layers would partially screen the activated field from the electrode, which finally resulted in a saturated contact angle formed at the triple contact line. Based on this concept, a modified contact angle actuation equation was derived where the effect of the potential of trapped charge layer outside the droplet was included. Another explanation was given by Pekov *et al*. [56] who claimed that Equation (3-3) would lose its accuracy when the effective surface tension at the solid-liquid interface ${\sigma_{sl}}^{eff}$ approached zero since the droplet interface was supposed to have positive energy to remain stable under any circumstance. Shapiro *et al*. [50] conducted a numerical study on the equilibrium shape of a liquid droplet on a single-plate EWOD device under the effect of applied electrical fields. It was found that the observed saturation phenomenon came from the increase of potential drop within the droplet when the contact angle decreased at the triple contact line.

Recently, Papathanasiou and his coworkers [57-59] carried out a series of investigations on diverging electric fields in the vicinity of triple contact line. It was demonstrated that the volume elements in dielectric layer would become conductive when the local electrical field was greater than the breakdown field strength of the material. When the voltage exceeded the critical value, a finger-like structure would be formed at the surface of insulating layer, which screened the electrical charges and consequently suppressed the electrical force at the triple contact line. It was claimed that this explanation appeared to correctly capture the essence of contact angle saturation [51].

All the explanations given above were found to apply favorably on particular experimental data but exhibited some unresolved aspects or their own limitations. The mechanism of contact angle saturation has still not received broad acceptance and a more general explanation is needed to be discovered in the future.

3.4 Electrowetting-induced Pressure Force

Since the contact angle at the triple contact line can be modified by applying electrical potential at the droplet boundary, this will alter the droplet surface curvature and consequently the surface tension induced pressure at the gas-liquid interface according to the Young-Laplace equation [60]:

$$\Delta p = \sigma_{LG}(\kappa_{xy} + \kappa_z) \tag{3-4}$$

where Δp is the surface tension induced pressure at the gas-liquid interface, κ_{xy} and κ_z the mean curvatures on the x-y plane and along the z-direction, respectively. Since the channel height is very small compared to the device dimension, the gas-liquid interface in the z-direction can be approximated as circular which yields

$$\kappa_z = \frac{(-\cos\theta_t - \cos\theta_b)}{H} \tag{3-5}$$

where θ_t and θ_b are the contact angles at the top and bottom plates, respectively and H the channel height between the two parallel plates. See Figure 3-2. Note that θ_t is always constant since the top electrode is grounded, but θ_b varies according to Equation (3-3).

Combination of Equations (3-4) and (3-5) gives the pressure difference at the droplet boundary across the ON and OFF regions as,

$$p_{OFF} - p_{ON} = \sigma_{LG}(\frac{\cos\theta_{b,ON} - \cos\theta_{b,OFF}}{H} + k_{xy,OFF} - k_{xy,ON}) \tag{3-6}$$

As shown in Figure 3-4, when electrical charges are applied on one side of droplet, the surface tension at the interface is reduced due to the decreased contact angle $\theta_{b,ON}$. This reduced surface tension on the electro-wetted side of the droplet leads to an imbalanced pressure force which moves the droplet from the OFF to the ON side.

In the present study, a dimensionless curvature $\tilde{k}$ is introduced, which is defined as,

$$\tilde{k} = \frac{\Delta\kappa_z}{k_{xy}} \tag{3-7}$$

where $\Delta\kappa_z$ is given by

$$\Delta\kappa_z = k_{z,OFF} - k_{z,ON} \tag{3-8}$$

$k_{z,OFF}$ and $k_{z,ON}$ are the z-curvatures of the gas-liquid interfaces on the OFF and ON electrodes, respectively (Figure 3-4). By incorporating the definition of k_{xy} and Equation (3-5), $\tilde{k}$ becomes

$$\tilde{k} = \frac{R}{H}(\cos\theta_{b,ON} - \cos\theta_{b,OFF}) \tag{3-9}$$

where R is the radius of the circular droplet in the x-y plane in the initial condition (Figure 3-2). According to Equation (3-7), $\tilde{k}$ represents the relative significance between $\Delta\kappa_z$ and κ_{xy} in a particular droplet operation, i.e., a larger value of $\tilde{k}$ represents that $\Delta\kappa_z$ has a more dominant effect than κ_{xy} in the droplet motion.

3.5 Contact Angle Hysteresis

An essential element in EWOD modeling is contact angle hysteresis, which refers to the difference in contact angles between the advancing and receding ends when the droplet is in motion [14, 33, 48, 61-63]. As shown in Figure 3-5, a unique contact angle θ_S, referred to as the static contact angle, is formed at the triple contact line when the drop is stationary on a flat plate. As the droplet moves, the contact angle on the advancing side increases while that on the receding side decreases from θ_S and are referred to as advancing and receding contact angles, θ_A and θ_R, respectively. The difference between advancing and receding contact angles is referred to as contact angle hysteresis as,

$$\theta_{hys} = \theta_A - \theta_R \tag{3-10}$$

This hysteresis phenomenon has been observed in many experiments of microfluidic liquid motions [10, 11, 25, 41, 64]. It has been reported in some literature that a threshold voltage was required to compensate the hysteresis effect below which the liquid movement would not be initiated [11, 32]. Also, it was claimed that contact angle hysteresis appears to provide a reasonable explanation of the commonly observed phenomenon that droplet stays stationary on a titled plane of a very small angle: the gravity of the droplet is balanced by the hysteresis effect, which prevents the droplet from sliding downwards. Generally, contact angle hysteresis is an indispensible component in electrowetting-based microfluidic droplet motion, which has been included in many theoretical and numerical studies [19, 20, 38, 40, 62, 65, 66].

It was discovered that contact angle hysteresis has a retarding effect on the fluid motion by reducing the difference between the dynamic contact angles on the advancing and receding sides. As shown in Figure 3-6, when the hysteresis is included, contact angles $\theta_{t,A,hys}$ and $\theta_{b,A,hys}$ on the advancing side become greater than $\theta_{t,A}$ and $\theta_{b,A}$, the contact angles without hysteresis applied, respectively, which results in a larger curvature $\kappa_{z,ON,hys}$ compared to the original curvature $\kappa_{z,ON}$ according to Equation (3-5). On the receding side, contact angles $\theta_{t,R,hys}$ and $\theta_{b,R,hys}$ are smaller than $\theta_{t,R}$ and $\theta_{b,R}$, respectively, which creates a reduced z-curvature $\kappa_{z,OFF,hys}$ on the receding end. This variation in z-curvatures reduces the pressure difference across the droplet boundary according to Equation (3-6), which consequently slows down the droplet moving speed and retards the overall droplet motion. Details of the implementation of contact angle hysteresis into the current EWOD model will be given in Chapter 5.

3.6 Contact Line Friction

Contact line friction, which is also referred to as contact line pinning in some literature, was first proposed by Blake *et al*. [67] in 1969. It was explained as energy dissipation when the liquid is in motion due to the discrete random molecular displacements at the immediate vicinity of the triple contact line. This dissipation can be viewed as an opposing friction force against the droplet motion between the solid surface and the liquid molecules.

It has been reported in some electrowetting-based microfluidic droplet experiments that excess dissipation existed in the droplet motion which could not be justified by the viscous effects between the droplet and the solid plane. Therefore, an additional resistant force referred to as contact line friction force was introduced to account for this extra dissipation, which has been widely discussed in various microfluidic problems [14, 24, 48, 51, 64, 68, 69] and implemented into a number of numerical EWOD models as a significant component [20, 23, 37, 65, 70].

This newly emerged microfluidic concept appears to offer an alternative explanation for the phenomenon that the droplet stays stationary on a titled plane of a very small angle due to the pinning effect of the friction force at the triple contact line. It has been found that this friction force had a threshold value beyond which the sliding motion would take place when the plane was tilted over a critical angle and the gravity of the droplet eventually dominated the friction force. For the droplet interface at low speed, the magnitude of the friction force was proportional to the velocity and the length of the interface element with the direction being opposite to the interface moving direction [23, 65, 70].

Even though the nature of contact line friction is not fully understood and its mechanism is still under debate, a widely accepted idea is that the friction effect has an inseparable relationship with contact angle hysteresis. Since these two physical components both possess the same retarding effect on droplet motion at the triple contact line, the implementation of both components into the EWOD model appears to be redundant. In the present study, only the hysteresis effect is applied for simulating microfluidic droplet motions in parallel-plate EWOD devices.

3.7 Viscous Stress Exerted by the Parallel Plates

The viscous force exerted by the two parallel plates is another crucial component in EWOD modeling without which the droplet motions cannot be accurately described. In recent years, the viscous stress involved in electrowetting-based droplet motions has been closely examined in both experimental and numerical studies [19, 23, 37, 65, 70].

Since the channel heights of the EWOD devices used in the current study are much smaller than the droplet dimensions in the x-y domain (H ≤ 0.1mm), it is fairly reasonable to make an assumption that the flow can be modeled by a two-dimensional flow field. As a consequence, the electrowetting-induced pressure is expected to be uniform in the z-direction and the velocity component in the z-direction is negligible [42]. The microfluidic flow can be approximated as a plane flow in the x-y plane and the Couette flow model can be used for analyzing the variation of velocities u and v in the z-direction if the flow were fully developed. However, since the droplet motions involve time-varying movement of the fluid and the flow is by no means steady in the present study, the viscous stress equations from the Couette flow model are modified with the incorporation of a multiplication factor λ_{vs}, which are given by:

$$\tau_{zx} = \lambda_{vs} * \mu * \frac{u}{H} \tag{3-11}$$

$$\tau_{zy} = \lambda_{vs} * \mu * \frac{v}{H} \tag{3-12}$$

where μ is the dynamic viscosity, u and v the average velocities in the x- and y-direction respectively. Equations (3-11) and (3-12) are used to approximated the viscous stress exerted by the parallel plates at the solid-liquid interface as the liquid is in motion. More details about λ_{vs} including the values for each droplet operation will be given in Chapter 6.

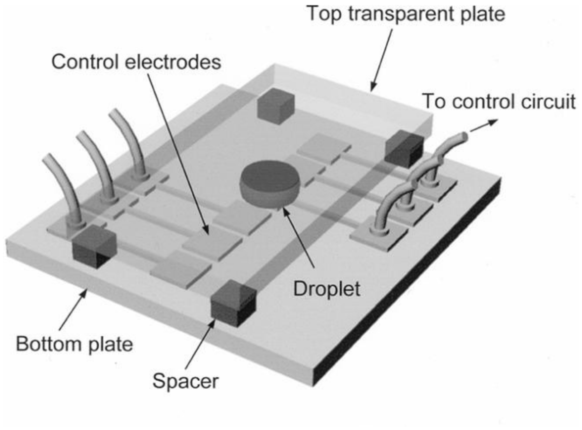

Figure 3-1 A Typical Experimental Parallel-plate EWOD Device [11]

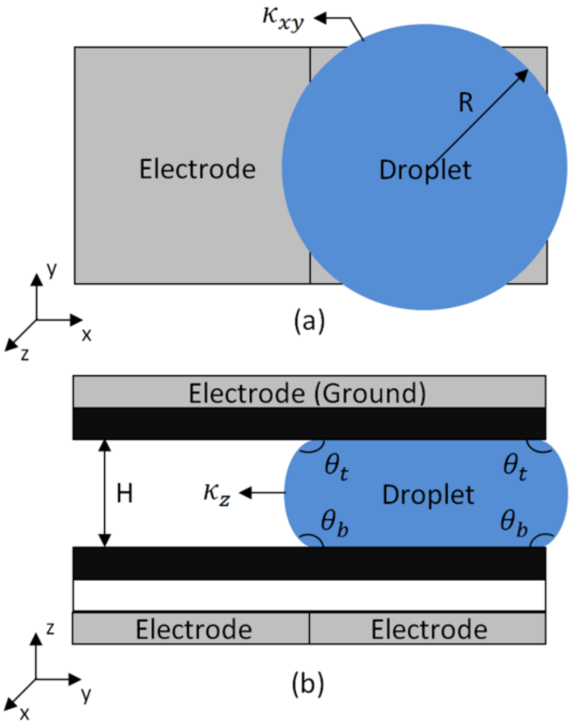

Figure 3-2 The Schematics of Parallel-plate EWOD Device: Top (a) and Cross-sectional (b) Views (The Top Plate is Transparent in the Top View)

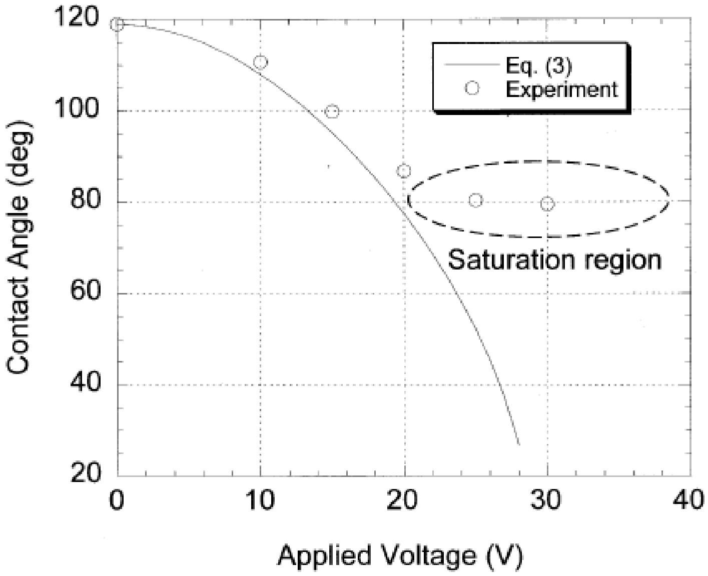

Figure 3-3 Contact Angle Saturation Effect [11]

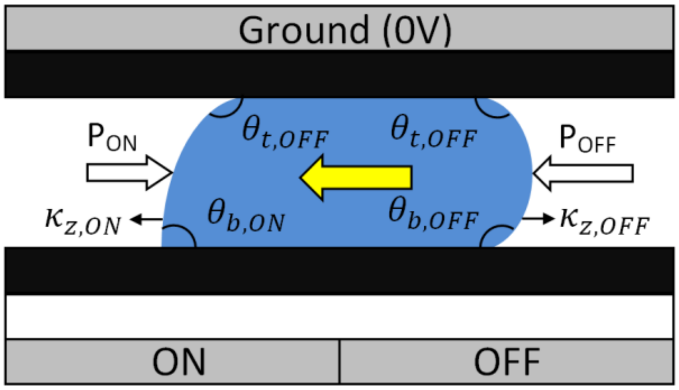

Figure 3-4 Pressure Difference across the Droplet Boundary Induced by the Electrical Actuation

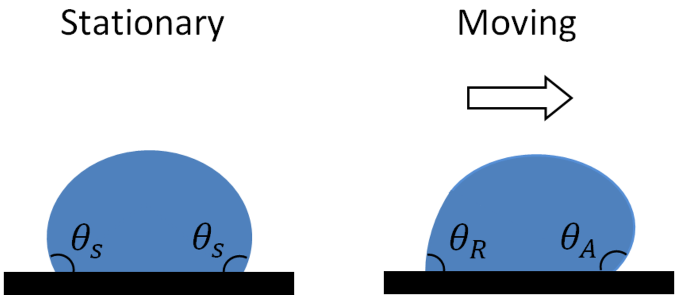

Figure 3-5 Contact Angle Hysteresis Effect: θ_S, θ_R and θ_A are Static, Receding and Advancing Contact Angles Respectively

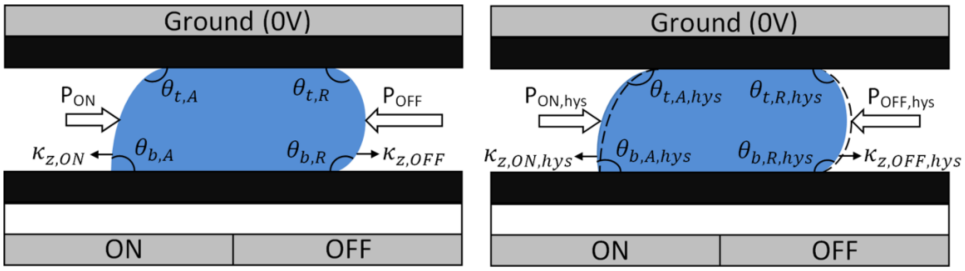

(a) (b)

Figure 3-6 Retarding Effect of Contact Angle Hysteresis: Without Hysteresis (a); With Hysteresis (b) (Dashed Lines Represent the z-curvatures When the Hysteresis is not Applied)

Chapter 4

Interface and Surface Tension Modeling

4.1 Interface Tracking Methods

Several computational methods have been devised for interface modeling over the past few decades [71, 72]. These methods are divided into two distinctive categories, Lagrangian or Eulerian methods, based on the way the interface is followed as well as the type of numerical domains opted.

For the Lagrangian methods, the interface is maintained as a discontinuity and is defined as a series of discrete points which are tracked explicitly. Lagrangian methods are preferred for fluid problems with small interfacial deformations due to the precise representation of interface locations. For the Eulerian methods, the interface is captured implicitly, which is represented by appropriate field functions on a fixed numerical domain. Specific advection techniques are usually required to preserve the sharpness of the interfacial front. Eulerian methods are generally more suitable for fluid flows with complex interfacial deformations and topological changes. A brief discussion is given in the following for the numerical methods widely utilized for tracking the interface under the categories of Lagrangian and Eulerian methods.

4.1.1 Lagrangian Methods

Since the interface is explicitly tracked in the Lagrangian methods, the exact location of the interface can be obtained by solving the following motion equation:

$$\frac{d\vec{x}_i}{dt} = \vec{u}_i \qquad (4\text{-}1)$$

where $\vec{x}_i$ is the position vector of the interface and $\vec{u}_i$ the velocity vector. This category contains front tracking, moving grid, particle-based and boundary integral methods.

4.1.1.1 Front Tracking Method

The front tracking method originates from the marker-and-cell (MAC) method [73] and the subsequent extension proposed by Daly [74]. The interface is represented by Lagrangian markers connected to form a front which moves through a stationary Eulerian domain. Due to the high-order interpolation polynomials used to represent the interface, the front tracking method has excellent accuracy in explicitly tracking the interface locations. However, this method suffers from some shortcomings including the failure of mass conservation and the artificial handling of topological variations. The applications of front tracking method have been discussed in various interfacial flow problems [75-78].

4.1.1.2 Moving Grid Method

In the moving grid methods, the interface is technically a boundary between two sub-domains in a Lagrangian grid where the interface is automatically tracked by the grid when it moves with the fluid. This method has been applied in a large number of finite-element methods with decent robustness demonstrated and has been found especially effective for modeling weakly deformed bubbles and small amplitude waves [79-81]. In general, the moving grid method can produce very accurate results for interfacial flows with regular topologies and small deformation. However, for the flow problem with large interface deformations, the results may suffer from serious numerical errors when the element connectivity rules are violated, which could lead to the termination of numerical simulations. Applications of the moving grid method can be found in [82-84].

4.1.1.3 Particle-Based Method

In the particle-based methods, the fluid is represented by a number of discrete particles which carry mass, momentum and energy and the interface is tracked by identifying the position of each individual particle. Particle-based methods eliminate the grid either partially, such as in the particle-in-cell (PIC) method [85], or completely, such as in the smoothed particle hydrodynamics (SPH) method [86, 87].

Topological changes in fluid can be easily handled in the particle-based methods since individual particle can move freely in the domain. By using particle motion to approximate the advection terms, the numerical diffusion across the interfaces can be fully eliminated. Another merit of particle-based methods is that it is simple and straightforward to extend the implementation from 2-D to 3-D fluid flow. However, the particle-based methods are highly expensive in terms of CPU time and memory requirements, which are their major weaknesses to practical applications.

4.1.1.4 Boundary Integral Method

Boundary integral methods can be readily applied to some special flow problems such as creeping or inviscid flows. For creeping flows, one boundary integral method has been used by Stone and Leal [88, 89] to investigate the deformation, relaxation and breakup processes of a viscous droplet in which the inertia of the flow was neglected. For inviscid flows, the Navier-Stokes equation is reduced to the Euler equation in which the interface is treated as a vortex sheet as well as a free boundary between phases [90]. The development of the flow is deduced from the discrete points on the interface.

The main benefits of the boundary integral methods are that the fluid problem can be reduced by one dimension and the results are still sufficiently accurate if the flow has a regular topology. However, it is very challenging to apply this method to 3-D flow problems. Besides, when the flow undergoes some severe topological changes, artificial manipulation is required for local interface transformation.

4.1.2 Eulerian Methods

In the Eulerian methods, the interface is represented by a field function, which is advanced by solving the following advection equation:

$$\frac{DC}{Dt} = \frac{\partial C}{\partial t} + (\vec{u} \cdot \nabla)C = 0 \tag{4-2}$$

where C is the field function and $\vec{u}$ the velocity vector. The interface is implicitly captured and can be reconstructed from the updated field functions. Continuum advection, volume tracking and level set schemes are included in this category.

4.1.2.1 Continuum Advection Method

The continuum advection methods refer to the traditional difference methods for solving Equation (4-2), which is a simple hyperbolic type that can be solved with a variety of approaches such as first-order upwind, high-order monotonic van Leer [91] and PPM [92] schemes. These schemes are developed upon the premise that the field function C is varying smoothly. However, when C is discontinuous, such schemes encounter interface diffusion problems if the convection term is approximated by standard spatial differences of C directly across the interface. Even with higher-order approximations, the numerical diffusion still broadens the interface to an unacceptable width of as many as four to eight cells. One way to fix this problem is to transform the discontinuous C function into a smooth function ϕ, then solve Equation (4-2) with ϕ and eventually transform ϕ back to C, which provides the basic theory of the level set (LS) method [93].

4.1.2.2 Volume-of-Fluid (VOF) Method

The Volume-of-Fluid (VOF) method emerged in the early 1970s and now has become the most widely used Eulerian interface tracking technique [94, 95]. In the VOF method, the interface is captured by the VOF function $F(\vec{x}, t)$ which represents the volume fraction occupied by the liquid in each computational cell. The VOF function is usually advected by non-diffusive and geometric schemes in order to keep the interface sharp. Over the last few decades, several developments have been made to improve the VOF method [96], in which a very accurate interface reconstruction scheme, the piecewise linear interface construction (PLIC) method, has been employed [97, 98]. One of the most favorable merits of the VOF method is the excellent property of mass conservation. However, the calculations of curvature and interface normal are not very accurate due to the discontinuous spatial derivatives of the VOF function near the interface.

4.1.2.3 Level Set (LS) Method

The LS method was first introduced by Osher and Sethian [99], the application of which has expanded from interface tracking scheme to grid generation, image enhancement, computer recognition, *etc*. [100, 101]. In the LS method, the interface is described by the LS function $\phi(\vec{x}, t)$, which is defined as a signed distance function. Its magnitude is the distance from the cell center to the nearest interface with its sign being negative inside the interface and positive outside of the interface; the function has a zero value when the cell center is at the interface.

The LS function is advanced by the following advection equation:

$$\frac{\partial \phi}{\partial t} = -(\vec{u} \cdot \nabla)\phi \tag{4-3}$$

The discretization of the advection equation is straightforward since the LS function is smooth and continuous. However, it has been found that the LS function will fail to be a distance function after being advanced by Equation (4-3) and thus a reinitialization process [102] is needed for its return to a distance function. Generally, the reinitialization process is not mass conserved, which is the main disadvantage of the LS method.

4.2 Surface Tension Modeling Methods

It is well known that the cohesive forces for the molecules within the liquid are balanced in all directions. However, for the molecules at or near the gas-liquid interface, the intermolecular forces are unbalanced due to the greater attraction of liquid molecules to each other than to the molecules in the air. As shown in Figure 4-1, the unbalanced forces for the liquid molecules near the interface lead to the surface tension effect, which causes liquid to behave as if its surface were covered with a stretched elastic membrane. The surface tension force is essential for some important interfacial flow problems such as droplet and bubble deformation, liquid ligament breakup, microfluidic droplet operations, *etc*.

The robustness of the surface tension modeling algorithm is found to play an extremely significant role in the accuracy of the numerical study of interfacial flows, which is also strongly dependent on the computational scheme used for tracking the interface. A brief discussion on surface tension modeling methods associated with various interface tracking approaches is given in the following, which include surface tensile force, boundary and jump condition and continuum surface force methods.

4.2.1 Surface Tensile Force Method

For the fluid problems using the front tracking methods, the surface tension force is calculated directly on the Lagrangian domain [103-105] and then distributed to the fixed Eulerian grid. If the exact location of the interface is known, it is the most convenient way to treat the surface tension as a surface tensile force which is pulling along the interface.

As shown in Figure 4-2, the surface tension on an element of the interface in the two-dimensional case can be written as:

$$\overrightarrow{F_s}(\vec{x}_s) = \int_1^2 \sigma d\vec{t} = \sigma(\vec{t}_2 - \vec{t}_1) \tag{4-4}$$

where $\vec{x}_s$ is the position vector at the interface, σ the surface tension coefficient and $\vec{t}_1$ and $\vec{t}_2$ the unit tangent vectors at the ends of an interface element. In this method, the sum of the surface tension forces around a closed surface is identically equal to zero so that the conservation property is exactly preserved.

The surface tensile force method is commonly used with the front tracking method [103] via which the interface can be explicitly represented with discrete points and elements. This model may not be applicable for the Eulerian-based interface tracking methods since the exact locations of the interface are unavailable.

4.2.2 Boundary and Jump Condition Method

The surface stress condition in the normal direction at the interface between two immiscible fluids is given by

$$p_v - p + \sigma\kappa = -2\mu n \frac{\partial u}{\partial n} \tag{4-5}$$

where p_v is the gas pressure, σ the surface tension coefficient, κ the local free surface curvature, μ the dynamic viscosity, n the free surface normal and u the velocity. For interfacial flows, the surface tension effect serves as an internal jump condition for the pressure at the interface. However, direct application of this jump condition is found to be very challenging which requires the solution of a complicated elliptic problem [106]. For free surface flows, it is much easier since the viscous effects at the free surface can be neglected and Equation (4-5) is reduced to the following Laplace's formula:

$$p - p_v = \sigma\kappa \tag{4-6}$$

If p_v is taken as constant in the above equation, the surface tension effect becomes a Dirichlet pressure boundary condition which can be simply applied at the free surface. This method is quite suitable for a variety of moving and adaptive grid methods [71] and the applications for free surface flows can be found in [107, 108].

4.2.3 Continuum Surface Force Method

The continuum surface force (CSF) method has been substantially used with the VOF and LS methods to model the surface tension force since it was first introduced by Brackbill *et al*. [109]. In the CSF method, the surface tension effect is treated as a body force distributed within a transition region of finite thickness in the neighborhood of the interface. The fluid properties are assumed to change continuously from one fluid to another across the transition region. This body force located at the grid points acts on every fluid element in the transition region. Since the surface tension force is not exerted exactly at the interface, the exact interface location is no longer needed for the computation. The continuum treatment of the discontinuous change of the surface tension force at the interface eases the implementation of the surface tension effect where only the VOF function or the LS function is needed.

The CSF method has demonstrated outstanding robustness and versatility in fluid problems with complex topological variation and interface deformation over the traditional surface tension modeling approaches. However, this method has been found to generate "spurious currents" in the neighborhood of the interface [98, 110, 111]. These vortex-like currents may lead to disastrous instabilities at the interface in surface tension dominant problems as shown in Figure 4-3, which may also result in failure of convergence upon grid refinement.

It should be noted that this review of interface tracking and surface tension modeling approaches is only at an introductory level. Detailed and comprehensive discussions on each method can be found in the relevant references provided above.

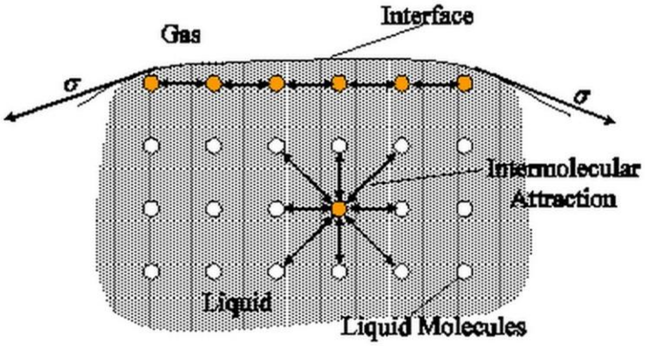

Figure 4-1 Molecular Forces and Surface Tension

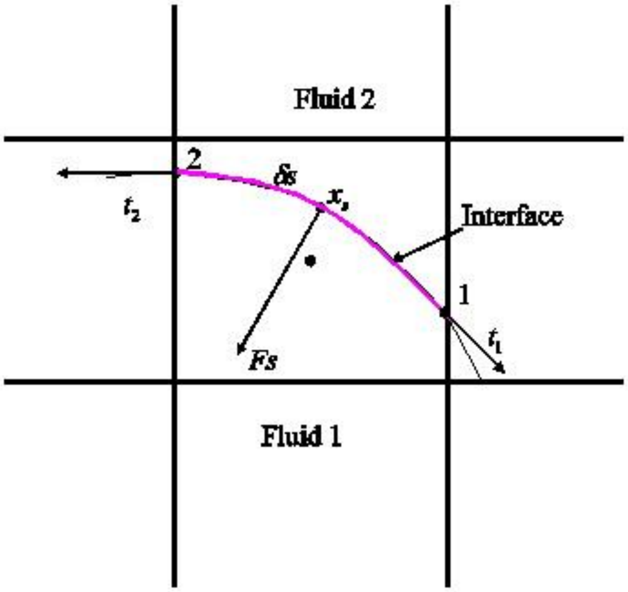

Figure 4-2 Surface Tensile Force Exerted at a Point $\vec{x}_s$ on an Interface Element δS

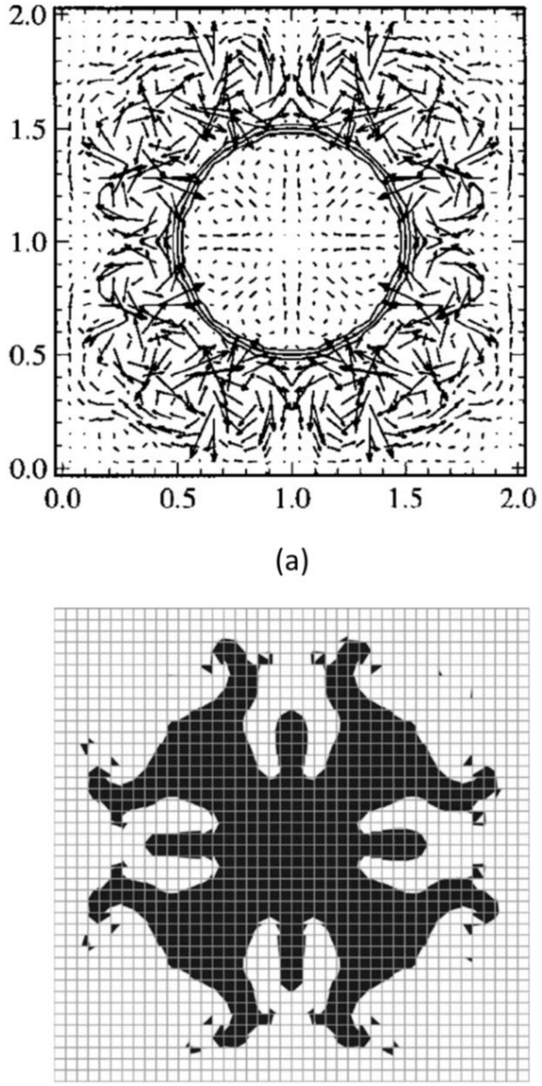

(a)

(b)

Figure 4-3 Spurious Currents in the Neighborhood of the Interface in the CSF Method: Spurious Currents Arising Around a Droplet (a); a Typical Deformed Shape of a Droplet at the End of the Simulation (b) [111]

Chapter 5

Numerical Formulation

5.1 Governing Equations

For incompressible, immiscible fluids which are separated by a moving interface, the motion of both fluids can be described by the continuity and the Navier-Stokes equations, which are given by

$$\nabla \cdot \vec{u} = 0 \tag{5-1}$$

$$\frac{\partial \vec{u}}{\partial t} + \vec{u} \cdot \nabla \vec{u} = -\frac{1}{\rho} \nabla P + \frac{1}{\rho} \nabla \cdot \tau + \vec{g} + \frac{\vec{F}_b}{\rho} \tag{5-2}$$

where $\vec{u}$ is the velocity, ρ the density, P the pressure, τ the viscous stress tensor, $\vec{g}$ the gravitational acceleration and $\vec{F}_b$ the body force. It should be noted that a free surface flow model is adopted in this study in which the dynamic effect of the air is neglected. For Newtonian fluids, the viscous stress tensor τ can be written as:

$$\tau = 2\mu S \tag{5-3}$$

where μ is the dynamic viscosity and S the strain rate tensor given by

$$S = \frac{1}{2}[(\nabla \vec{u}) + (\nabla \vec{u})^T] \tag{5-4}$$

Equation (5-2) is approximated in the finite-difference form as,

$$\frac{\vec{u}^{n+1}-\vec{u}^{n}}{\delta t} = -\vec{u}^{n} \cdot \nabla \vec{u}^{n} - \frac{1}{\rho^{n}} \nabla P^{n+1} + \frac{1}{\rho^{n}} \nabla \cdot \tau^{n} + \vec{g}^{n} + \frac{1}{\rho^{n}} \overrightarrow{F_b}^{n} \tag{5-5}$$

where the superscripts n and $n+1$ represent the value of the variable at consecutive time steps. Gravity, advection, surface tension and viscosity are approximated with old time t^n values and pressure is the only implicit term in the above equation.

A two-step projection algorithm is used where Equation (5-5) is decomposed into the following two equations:

$$\frac{\vec{u}^{*}-\vec{u}^{n}}{\delta t} = -\vec{u}^{n} \cdot \nabla \vec{u}^{n} + \frac{1}{\rho^{n}} \nabla \cdot \tau^{n} + \vec{g}^{n} + \frac{1}{\rho^{n}} \overrightarrow{F_b}^{n} \tag{5-6}$$

and

$$\frac{\vec{u}^{n+1}-\vec{u}^{*}}{\delta t} = -\frac{1}{\rho^{n}} \nabla P^{n+1} \tag{5-7}$$

where $\vec{u}^{*}$ represents an intermediate velocity. In the first step, $\vec{u}^{*}$ is computed from Equation (5-6) which accounts for incremental changes resulting from viscosity, advection, gravity and body forces. The second step involves taking the divergence of Equation (5-7) while projecting the velocity field, $\vec{u}^{n+1}$, to a zero-divergence vector field for mass conservation. This results in a single Poisson equation for the pressure field given by:

$$\nabla \cdot \left[\frac{1}{\rho^{n}} \nabla P^{n+1}\right] = \frac{\nabla \cdot \vec{u}^{*}}{\delta t} \tag{5-8}$$

which can be solved by using an incomplete Cholesky conjugate gradient (ICCG) solution technique [112] and the results are used to obtain $\vec{u}^{n+1}$ from Equation (5-7).

5.2 Interface Tracking Methods

The main complexity of the numerical simulation is the dynamics of a rapidly moving free surface, the location of which is unknown and is needed as part of the solution. The selection of the interface tracking scheme is based on the physical problem under consideration. As mentioned in Chapter 1, the problems of interest in the current study are capillarity-dominant free surface flows with large topological changes and flow distortions, for which the Eulerian-based methods are more suitable.

The volume-of-fluid (VOF) method [95-98, 113] and the level set (LS) method [102] have been substantially utilized as two Eulerian-based interface tracking methods over the decades. The interface is tracked implicitly by the phase functions in these two methods: volume fraction for the VOF method and distance function for the LS method. One of the most favorable advantages offered by these methods is the convenience of handling flow problems with large interface deformations and topological variations, which include droplet elongation and breakup, liquid ligament relaxation, bubble merging and bursting, and microfluidic droplet motions.

As discussed in Chapter 4, both the VOF and LS methods have their own merits and limitations. The VOF method has the desirable property of mass conservation. However, due to the discontinuous spatial derivatives of the VOF function near the interface, it lacks accuracy on the normal and curvature calculations. This may lead to convergence problems [71, 110, 111, 114] especially in the surface tension dominant problems. As for the LS method, the normal and curvature can be calculated accurately from the continuous and smooth distance functions. However, one major shortcoming of the LS method is the frequent violation of mass conservation.

In order to overcome such weaknesses of the LS and VOF methods, a coupled level set and volume-of-fluid (CLSVOF) method has been explored [115-120]. This innovative interface tracking approach combines the strengths of the VOF and LS methods and offers much improved accuracy on the surface curvature and normal calculations while maintaining mass conservation. In the CLSVOF method, the interface is reconstructed via a piecewise linear interface construction (PLIC) scheme from the VOF function and the interface normal vector is computed from the LS function. Based on the reconstructed interface, the LS functions are re-distanced via a geometric procedure for achieving mass conservation. By taking advantage of both the VOF and LS methods, the CLSVOF method is capable of achieving mass conservation while obtaining accurate results of the surface curvature and normal computations. A flow chart for the CLSVOF algorithm is shown in Figure 5-1. The coupling of the VOF and LS methods occurs at the interface reconstruction and the re-distancing of the LS function.

It should be noted that the implementation of the PLIC scheme is not unique and a number of implementation schemes have been presented. Also, various implementation algorithms have been reported for re-distancing the LS functions in the CLSVOF method. In the present study, the PLIC scheme devised by Rudman [97, 98] is followed for the VOF method and the re-distance algorithm presented by Son and Hur [117] is adopted for the LS functions. A brief discussion of the VOF and LS methods is given next, followed by the CLSVOF algorithm.

5.2.1 Volume-of-Fluid (VOF) Method

In the VOF method, the interface is tracked by the VOF function which is defined as the liquid volume fraction in a numerical cell. The magnitude of VOF function is zero and one in air and liquid respectively and between zero and one in a cell with an interface, i.e.,

$$F(\vec{x},t)=\begin{cases}1 & \text{in the fluid}\\ 0<F<1 & \text{at free interface}\\ 0 & \text{external to fluid}\end{cases} \tag{5-9}$$

The VOF function data corresponding to a circle are shown in Figure 5-2. The number in each cell represents the volume fraction occupied by the liquid. The VOF functions are advanced by the following advection equation:

$$\frac{\partial F}{\partial t}+(\vec{u}\cdot\nabla)F=0 \tag{5-10}$$

Equation (5-10) is rewritten in the conservative form in order to preserve mass:

$$\frac{\partial F}{\partial t}+\nabla\cdot(\vec{u}F)=F(\nabla\cdot\vec{u}) \tag{5-11}$$

It is discretized temporally and decomposed into two fractional steps for the two-dimensional case, given by:

$$\frac{F^{*}-F^{n}}{\delta t}+\frac{\partial}{\partial x}(uF^{n})=F^{*}\frac{\partial u}{\partial x} \tag{5-12}$$

$$\frac{F^{n+1}-F^{*}}{\delta t}+\frac{\partial}{\partial y}(vF^{*})=F^{n+1}\frac{\partial v}{\partial y} \tag{5-13}$$

where F^* is the intermediate VOF function. As shown in Figure 5-3, the VOF function, F, is located at the cell center on the staggered grid along with the LS functions ϕ and the pressure P while the velocities, u and v, are stored at the cell edges. Discretizing Equations (5-12) and (5-13) spatially and integrating them over the computational cell (i, j) yields:

$$F^*{}_{i,j} = \frac{F_{i,j}^n \delta x_i \delta y_j - \delta t \delta y_j (flux_{i+\frac{1}{2},j} - flux_{i-\frac{1}{2},j})}{\delta x_i \delta y_j - \delta t \delta y_j (u_{i+\frac{1}{2},j} - u_{i-\frac{1}{2},j})} \tag{5-14}$$

$$F_{i,j}^{n+1} = \frac{F^*{}_{i,j} \delta x_i \delta y_j - \delta t \delta x_i (flux_{i,j+\frac{1}{2}} - flux_{i,j-\frac{1}{2}})}{\delta x_i \delta y_j - \delta t \delta x_i (v_{i,j+\frac{1}{2}} - v_{i,j-\frac{1}{2}})} \tag{5-15}$$

where $flux_{i\pm\frac{1}{2},j} = (uF^n)_{i\pm\frac{1}{2},j}$ and $flux_{i,j\pm\frac{1}{2}} = (vF^*)_{i,j\pm\frac{1}{2}}$, which denote VOF fluxes across the edges of the computational cell. However, the VOF functions $F_{i\pm\frac{1}{2},j}$ and $F_{i,j\pm\frac{1}{2}}$ at the cell edges are not explicitly defined. Direct arithmetic interpolation from the neighboring cell-centered values may lead to serious numerical errors since the VOF function F is not smoothly distributed across the interface. Therefore, a geometric calculation procedure, referred to as interface reconstruction, is necessarily implemented to evaluate the VOF flux across the surface cell.

5.2.2 Level Set (LS) Method

The LS function, ϕ, is defined as a signed distance function whose value equals the shortest distance from the cell center to the interface. Its sign is determined as:

$$\phi(\vec{x}, t) \begin{cases} > 0 & \text{outside of the interface} \\ = 0 & \text{at the interface} \\ < 0 & \text{inside of the interface} \end{cases} \tag{5-16}$$

i.e., negative in the liquid, positive in the air, and zero at the interface. The zero level set contours are used to represent the interface. The LS function is initialized as a distance function because of its important property, $|\nabla\phi| = 1$, which can be used to make a number of simplifications. An example for the LS functions representing a circle is shown in Figure 5-4 in which all the LS values located at the cell center are assigned as the shortest distance to the interface.

After initialization, the LS function is advanced by following propagating equation:

$$\frac{\partial\phi}{\partial t} + \vec{u} \cdot \nabla\phi = 0 \tag{5-17}$$

The discretization of Equation (5-17) is straightforward since the LS function is smooth and continuous and some simple advection schemes can be used. However, the LS function will fail to be a distance function (i.e., $|\nabla\phi| \neq 1$) after being advanced by Equation (5-17), which leads to the irregular fluid interface after some period of time as shown in Figure 5-5. The local gradient is increased in some regions due to the level sets pining up on each other, while in other regions, the gradient are flattened out since the level sets separate from each other. In order to reduce the numerical errors and restore it to a distance function, the LS function must be reinitialized by obtaining a steady-state solution of the following reinitialization equation [102]:

$$\frac{\partial\phi}{\partial t} = \frac{\phi_0}{\sqrt{{\phi_0}^2 + h^2}}(1 - |\nabla\phi|) \tag{5-18}$$

where ϕ_0 is the LS function at the previous time step, t the artificial time, and h the grid spacing. Equation (5-18) can be re-written as:

$$\frac{\partial\phi}{\partial t} + (\vec{w}\cdot\nabla)\phi = \frac{\phi_0}{\sqrt{{\phi_0}^2+h^2}} \tag{5-19}$$

where $\vec{w}$ is the propagating velocity normal to the interface with unity magnitude, given by:

$$\vec{w} = \frac{\phi_0}{\sqrt{{\phi_0}^2+h^2}}\left(\frac{\nabla\phi}{|\nabla\phi|}\right) \tag{5-20}$$

The zero level set is propagated both inwards and outwards in the normal direction.

The level set function will return to a distance function after the reinitialization process. However, it is generally acknowledged that the advection and reinitialization processes do not guarantee mass conservation. The LS functions must be re-distanced prior to being used, which can be accomplished by geometrically computing the distance from the cell center to the reconstructed interface after the interface reconstruction process.

5.2.3 Interface Reconstruction

In the CLSVOF method, the interface is located from the discrete VOF and LS functions via a specific reconstruction procedure, which serves two purposes: one is to compute the VOF fluxes across each numerical cell with an interface, and the other is to re-distance the LS function for achieving mass conservation. As mentioned earlier, a piecewise linear interface construction (PLIC) algorithm presented by Rudman [97, 98] is adopted for the interface reconstruction scheme in the current study. The interface within each cell is approximated by a straight line segment and the orientation of the line is given by the normal vector. The properly oriented interface is then located in the cell with the area (volume) determined from the VOF function. A brief discussion of the PLIC scheme is given here.

The normal vector to the interface is estimated from the smooth LS function as:

$$\vec{n} = \frac{\nabla\phi}{|\nabla\phi|} = \nabla\phi \tag{5-21}$$

which is different from the VOF method where discontinuous VOF functions in the neighboring cells are used to obtain the normal vector [121]. The interface curvature, also computed from the LS function, is given by

$$\kappa = \nabla \cdot \left(\frac{\nabla\phi}{|\nabla\phi|}\right) \tag{5-22}$$

The orientation angle of the interface is defined as:

$$\alpha = tan^{-1}\left(\frac{n_y}{n_x}\right)\ (0 < \alpha < 2\pi) \tag{5-23}$$

where α is the angle that the outward-pointing unit normal makes with the positive x-axis. As shown in Figure 5-6, the multitude of possible interface configurations are reduced to only four cases by rotating each interfacial cell such that α lies in the range of $0 \leq \alpha \leq \pi/2$. Once the angle of the normal is determined, the line segment is moved along the normal direction to fit the shadow area (volume) with the VOF value in the cell. The shadow area (volume) can be calculated by the following n-sided area (volume) formula for the two-dimensional case:

$$A_{xy} = \frac{1}{2}\sum_{i=1}^{n}(x_i y_{i+1} - x_{i+1} y_i) \qquad (5\text{-}24)$$

Once the calculated area (volume) matches the VOF value at the cell, the coordinates of endpoints of the line segment are determined, which marks the completion of the interface reconstruction process. Then, the fluxes for the VOF advection can be evaluated based on the reconstructed interface. Details of this procedure can be found in [97] and are not discussed here.

5.2.4 Re-distancing of the LS Function

After the interface reconstruction, the LS functions need to be re-distanced in order to achieve mass conservation. The re-distancing process includes initial determination of the sign of the LS function and the subsequent computation of the distance from the cell centers to the nearest reconstructed interface through a geometric procedure.

First, the sign of the LS function, S^{ϕ}, is given by:

$$S^{\phi} = sign(0.5 - C) \qquad (5\text{-}25)$$

where $sign$ denotes a function that returns the sign of the numeric argument and C the VOF function for the two-dimensional case. It is understood that the LS function has the negative sign when $C > 0.5$ and the cell center will be located inside of the liquid, and vice versa.

Next, the most significant step of the re-distancing process is to determine the magnitude of the LS function. The basic idea is to find the closest point on an interfacial cell to the neighboring cell centers. Even though various configurations of the reconstructed interface exist, in general, all the interfacial cells can be simply divided into two categories: single-phase cells (i.e., $F = 0 \; or \; 1$) and interfacial cells (i.e., $0 < F < 1$). For two adjoining cells (i, j) and (i’, j’), the closest point on cell (i’, j’) to the center of cell (i, j) will always either be at the cell corner or the centroid of the cell edges. Therefore, these points have the first priority when calculating the nearest distance between two adjoining cells. When cell (i’, j’) contains a line segment, the closest point on the segment will be either the endpoint or the projection point of the center of cell (i, j). As a result, the possible closest points on cell (i’, j’) to cell (i, j) can be the corners and edge centers on the cell faces, or the endpoints and projection points on the line segment.

An example for the three possible configurations of the interface for the re-distancing process is shown in Figure 5-7. As shown in Figure 5-7a, when the cell (i’, j’) is a liquid cell, the shortest distances are calculated by simply connecting the centers of the neighboring cells to the corners or face centroids of cell (i’, j’). In Figure 5-7b, when the cell (i’, j’) contains an interface, the nearest point on the shadowed area to point A is its projection point onto the line segment within cell (i’, j’). For a more general case, as shown in Figure 5-7c, the nearest point from the interface to cell A or B is from the cell center to the projection point; the shortest distance from the interface to cell C or D is the endpoint of the segment; and for all other cells, the closest points on cell (i’, j’) are either at corners or at face centroids.

Specifically, the LS function is re-distanced based on the algorithm presented by Son and Hur [117]. The logic procedure is given as:

1. Set the magnitude of the LS function, $|\phi|$, to a large value and discard all the old values.

2. For each computational cell (i', j'), the following procedures are applied:

(a) If the cell (i', j') is a single-phase cell (i.e., $F_{i',j'} = 0\ or\ 1$) and has an adjoining cell (i'', j'') where $|i'' - i'| \leq 1$ and $|j'' - j'| \leq 1$, satisfying $S^{\phi}_{i'',j''} \neq S^{\phi}_{i',j'}$ (Figure 5-7a):

For each neighbor cell (i, j), where $|i' - i| \leq 4$ and $|j' - j| \leq 4$, satisfying $S^{\phi}_{i,j} \neq S^{\phi}_{i',j'}$, $|\phi_{i,j}|$ is assigned to be the shortest distance between cell center $\vec{x}_{i,j}$ and the points $\vec{x}_{i'+\frac{m}{2},j'+\frac{n}{2}}$ on the faces and vertices of cell (i', j'), where $m = max[-1, min(1, i - i')]$ and $n = max[-1, min(1, j - j')]$, as shown in Figure 5-7a.

(b) If $0 < F_{i',j'} < 1$ (Figures 5-7 b, c):

(1) Determine the distance from any neighboring cell center to the line segment which is evaluated as $d(\vec{x}) = \vec{n} \cdot (\vec{x} - \vec{x}_{s1})$ or $d(\vec{x}) = \vec{n} \cdot (\vec{x} - \vec{x}_{s2})$, where $\vec{x}_{s1}$ and $\vec{x}_{s2}$ are the end points of the interface obtained in the interface reconstruction process.

(2) For each neighboring cell (i, j), $|\phi_{i,j}|$ is assigned to be the shortest distance between the cell center $\vec{x}_{i,j}$ and the line segment or the points $\vec{x}_{i'+\frac{m}{2},j'+\frac{n}{2}}$ on the faces of cell (i', j'):

If $S^{\phi}_{i,j} \neq sign[d\left(\vec{x}_{i'+\frac{m}{2},j'+\frac{n}{2}}\right)]$, (point E of Figure 5-7c),

$|\phi_{i,j}| = min(|\phi_{i,j}|, \left|\vec{x} - \vec{x}_{i'+\frac{m}{2},j'+\frac{n}{2}}\right|)$

Else if the point $\vec{x}_{i,j} - \vec{n}d(\vec{x}_{i,j})$, which is projected from $\vec{x}_{i,j}$ onto the interface, is inside the cell ((i', j') (point A and B in Figure 5-7c),

$|\phi_{i,j}| = min(|\phi_{i,j}|, |d(\vec{x}_{i,j})|)$

Otherwise (point C and D of Figure 5-7c),

$|\phi_{i,j}| = min(|\phi_{i,j}|, |\vec{x}_{i,j} - \vec{x}_{s1}|, |\vec{x}_{i,j} - \vec{x}_{s2}|)$

It should be noted that the above re-distance process is not performed on the cells several layers away from the interface since only the LS values at the vicinity of the interfacial cells are needed for the computations of the surface curvature and normal vector.

The superiority of the CLSVOF methods over the VOF and LS methods has been clearly demonstrated by the advection tests in which the weakness of LS method has also been presented. The results are given in [122] and will not be discussed here.

5.3 Surface Tension Modeling Scheme

The accuracy of the surface tension modeling is extremely crucial to the current study since the microfluid flow is driven by the electrowetting-induced surface tension force. The surface tension at the gas-liquid interface is modeled with the continuum surface force (CSF) method. The basic idea of the CSF method is that the volume integral of the body force equals to the surface integral of the surface tensile force in the limit of infinitesimally small transition region with thickness h:

$$\lim_{h\to 0} \int_{\delta V} \vec{F}_b(\vec{x})dV = \int_{\delta S} \vec{F}_{sa}(\vec{x}_s)dS \tag{5-26}$$

where $\vec{x}_s$ is the position vector at the interface and $\vec{F}_{sa}$ the surface force per unit interfacial area given by:

$$\vec{F}_{sa} = \frac{d\vec{F}_s}{ds} = \sigma \frac{d\vec{t}(\vec{x}_s)}{ds} = \sigma\kappa(\vec{x}_s)\vec{n}(\vec{x}_s) \tag{5-27}$$

where σ is the coefficient of surface tension, κ the mean curvature and $\vec{n}$ the normal to the surface. The body force is given by:

$$\vec{F}_b = \sigma\kappa(\vec{x})\vec{n}(\vec{x})\delta(\vec{x}) \tag{5-28}$$

where $\delta(\vec{x})$ is a delta function concentrated at the interface defined by:

$$\delta(\vec{x}) = \begin{cases} (1 + \cos(2\pi\phi/3h))\,/3h & \mathit{if}\ \ |\phi| \leq 1.5h \\ 0 & \mathit{otherwise} \end{cases} \tag{5-29}$$

where ϕ is the level set function and h the grid spacing. The body force $\vec{F}_b$ is included in Equation (5-2) as a source term. The derivation which demonstrates that the identity in Equation (5-26) is satisfied by Equations (5-27) and (5-28) is given in [109]. A sketch of a sample CSF distribution is shown in Figure 5-8a. Non-zero body forces are only located in the transition regions outside of which no body force exists. The magnitude of the body force exhibits a bell-shaped profile along the interface normal as shown in Figure 5-8b.

As discussed in Chapter 3, there are two types of curvature, κ_{xy} and κ_z, involved in the current microfluidic problems, both of which are indispensable components in the current EWOD model and required in the surface tension force equation. By incorporating Equations (3-4) and (3-5), Equation (5-28) becomes:

$$\vec{F}_b = \sigma\left(\kappa_{xy} + \frac{-cos\,\theta_t - cos\theta_b}{H}\right)\vec{n}(\vec{x})\delta(\vec{x}) \tag{5-30}$$

Therefore, Equation (5-30) is the updated surface tension equation for modeling the microfluidic flow in the present study.

5.4 Contact Angle Hysteresis Modeling

As mentioned earlier, contact angle hysteresis has an overall effect of retarding droplet motions and its physics is still not completely understood. The fact that dynamic contact angles are influenced not only by the manufacturing material of hydrophobic layer [64], but also by other factors such as temperature, ambient pressure, droplet properties, plate surface smoothness makes prediction of dynamic contact angles very challenging. In order to properly implement the hysteresis effect into the current EWOD model without losing its essential mechanism, the following scheme is adopted in which the dynamic contact angles are assumed to be constant at all time.

First, the following equation is used to determine whether the interface is advancing or receding at each time step before the dynamic contact angles are applied,

$$\vec{n}\cdot\vec{u}\begin{cases}<0 & \text{Receding interface}\\ >0 & \text{Advancing interface}\end{cases} \tag{5-31}$$

Once the direction is determined, the dynamic contact angles are computed by the following equations,

$$\text{top receding angle} \qquad \theta_{t,R}=\theta_t-\Delta_R \tag{5-32}$$

$$\text{bottom receding angle} \qquad \theta_{b,R}=\theta_b-\Delta_R \tag{5-33}$$

$$\text{top advancing angle} \qquad \theta_{t,A}=\theta_t+\Delta_A \tag{5-34}$$

$$\text{bottom advancing angle} \qquad \theta_{b,A}=\theta_b+\Delta_A \tag{5-35}$$

where Δ_R and Δ_A are the deflections of the receding and advancing contact angles from the static contact angle. By replacing θ_t and θ_b in Equation (5-30) with the obtained dynamic contact angles from Equations (5-32) to (5-35), the hysteresis effect is properly implemented.

As discussed previously, Keshavarz-Motamed *et al*. [40] recently performed a numerical study on the effects of dynamic contact angles on electrowetting-based micro droplet transport in parallel-plate microchannels. It was reported that on average the advancing contact angle had an increase of 8° while the receding contact angle had a decrease of 8° as well compared to the static contact angle. Since the numerical setup used in that study has a similar design to the parallel-plate EWOD devices used here, 8° was first used as the value for both Δ_R and Δ_A in all four droplet operations. However, the comparison between the preliminary numerical results and corresponding experimental data showed that agreement was only achieved in the splitting and merging processes when 8° was applied, which was not suitable for the dispensing or transport process. Due to lack of information on dynamic contact angles for the experiments, Δ_R and Δ_A are assumed to have the same value for the dispensing and transport simulations. Optimum values of Δ_R and Δ_A are subsequently determined by matching the droplet shape of the numerical results with the corresponding experiments. More details about the dynamic contact angles in each droplet operation will be given in Chapter 6.

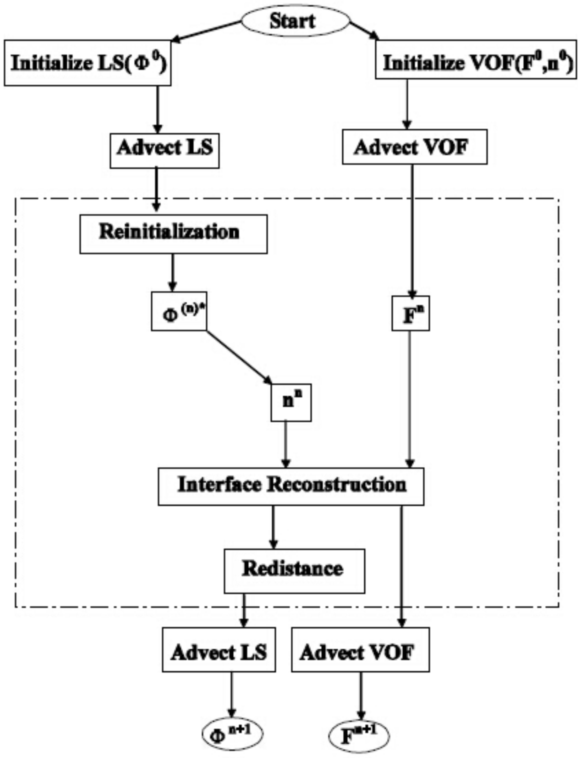

Figure 5-1 Flow Chart for the CLSVOF Scheme: Coupling Process in the Dashed Box

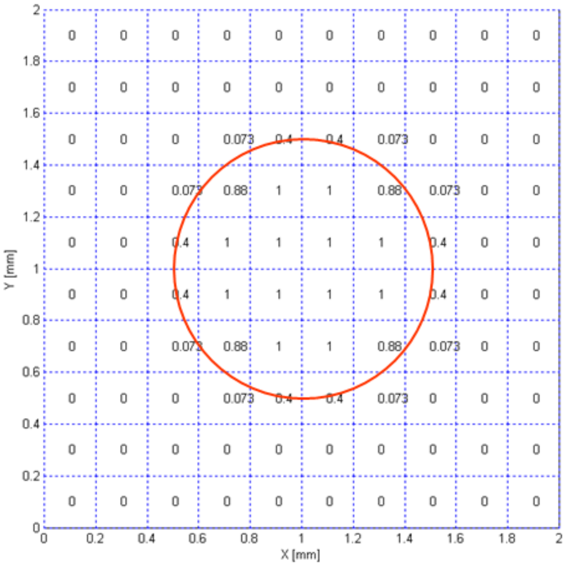

0	0	0	0	0	0	0	0	0	0
0	0	0	0	0	0	0	0	0	0
0	0	0	0.073	0.4	0.4	0.073	0	0	0
0	0	0.073	0.88	1	1	0.88	0.073	0	0
0	0	0.4	1	1	1	1	0.4	0	0
0	0	0.4	1	1	1	1	0.4	0	0
0	0	0.073	0.88	1	1	0.88	0.073	0	0
0	0	0	0.073	0.4	0.4	0.073	0	0	0
0	0	0	0	0	0	0	0	0	0
0	0	0	0	0	0	0	0	0	0

Figure 5-2 VOF Function Values Corresponding to a Circle over a Square Grid

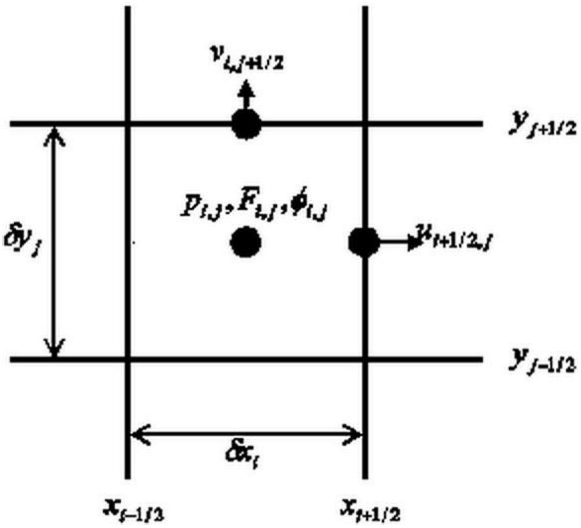

Figure 5-3 The Locations of Variables on a Numerical Cell

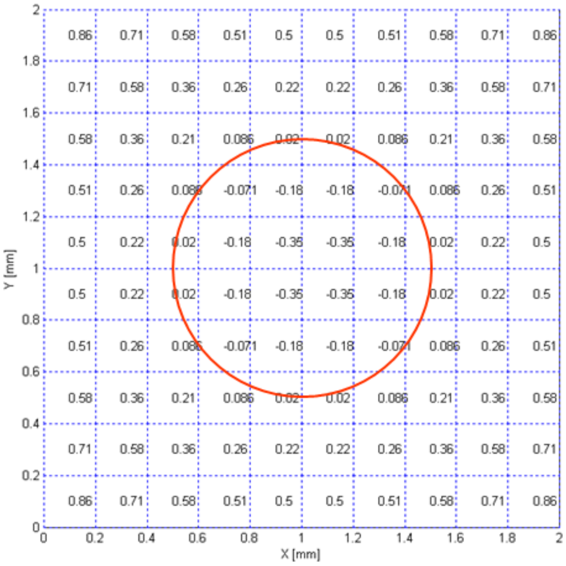

0.86	0.71	0.58	0.51	0.5	0.5	0.51	0.58	0.71	0.86
0.71	0.58	0.36	0.26	0.22	0.22	0.26	0.36	0.58	0.71
0.58	0.36	0.21	0.086	0.02	0.02	0.086	0.21	0.36	0.58
0.51	0.26	0.086	-0.071	-0.18	-0.18	-0.071	0.086	0.26	0.51
0.5	0.22	0.02	-0.18	-0.35	-0.35	-0.18	0.02	0.22	0.5
0.5	0.22	0.02	-0.18	-0.35	-0.35	-0.18	0.02	0.22	0.5
0.51	0.26	0.086	-0.071	-0.18	-0.18	-0.071	0.086	0.26	0.51
0.58	0.36	0.21	0.086	0.02	0.02	0.086	0.21	0.36	0.58
0.71	0.58	0.36	0.26	0.22	0.22	0.26	0.36	0.58	0.71
0.86	0.71	0.58	0.51	0.5	0.5	0.51	0.58	0.71	0.86

Figure 5-4 LS Function Values Corresponding to a Circle over a Square Grid

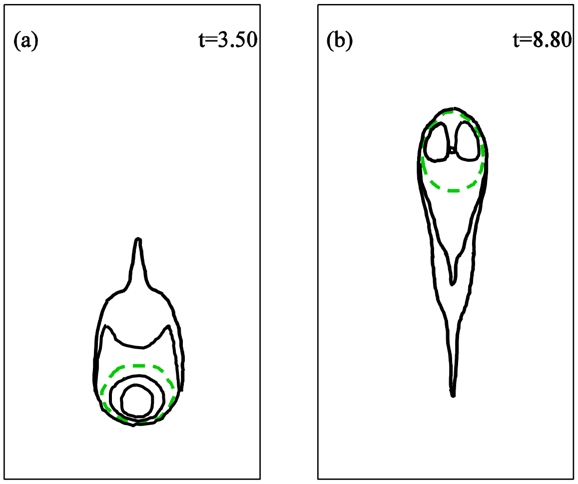

Droplet Bubble

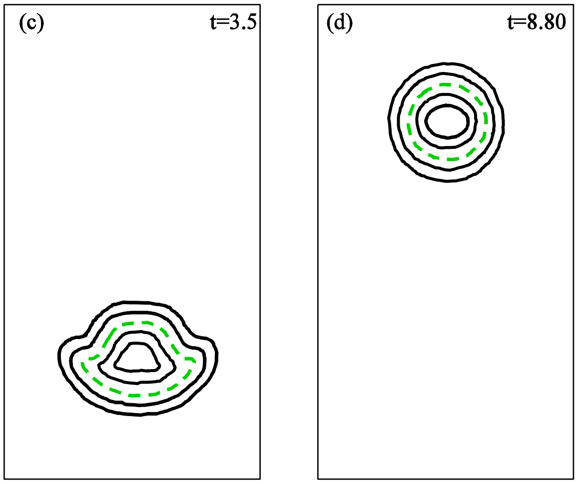

Droplet Bubble

Figure 5-5 Level Sets of a Falling Droplet and a Rising Bubble: Without Reinitialization (top); With Reinitialization (bottom); Contours Shown from -0.5 to 0.5 by 0.25, Dashed Line is the Zero Contour [102]

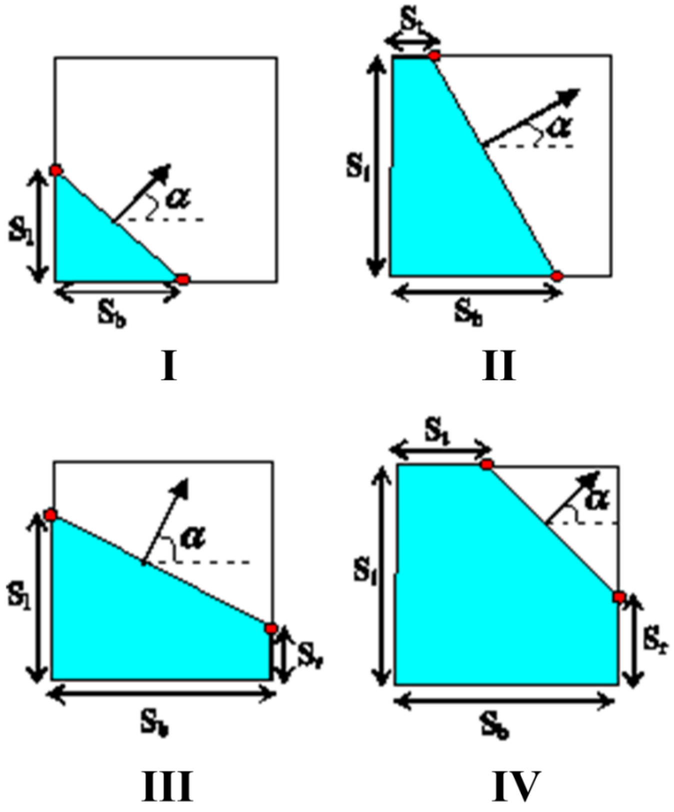

Figure 5-6 Possible Configurations for the Interface Reconstruction

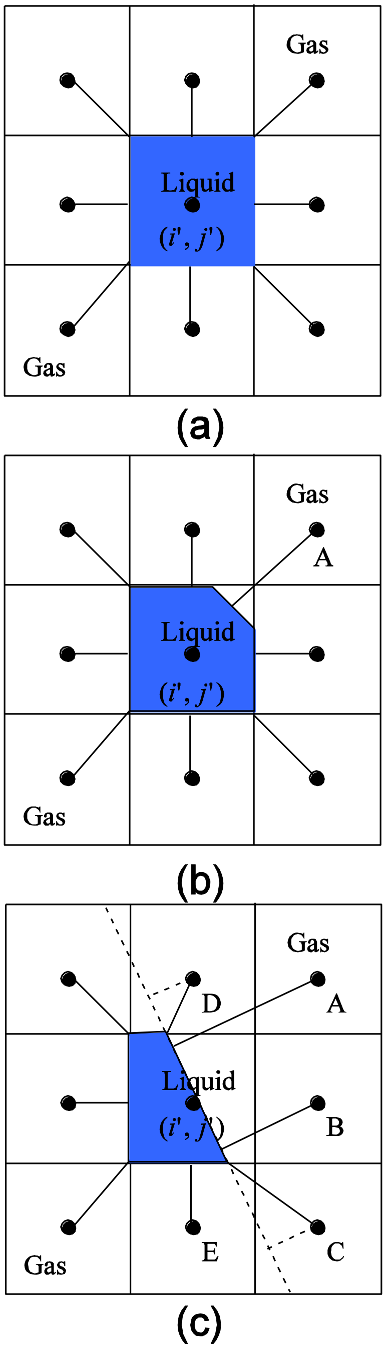

Figure 5-7 Possible Configurations of the Interface for the Re-distancing of the LS Function

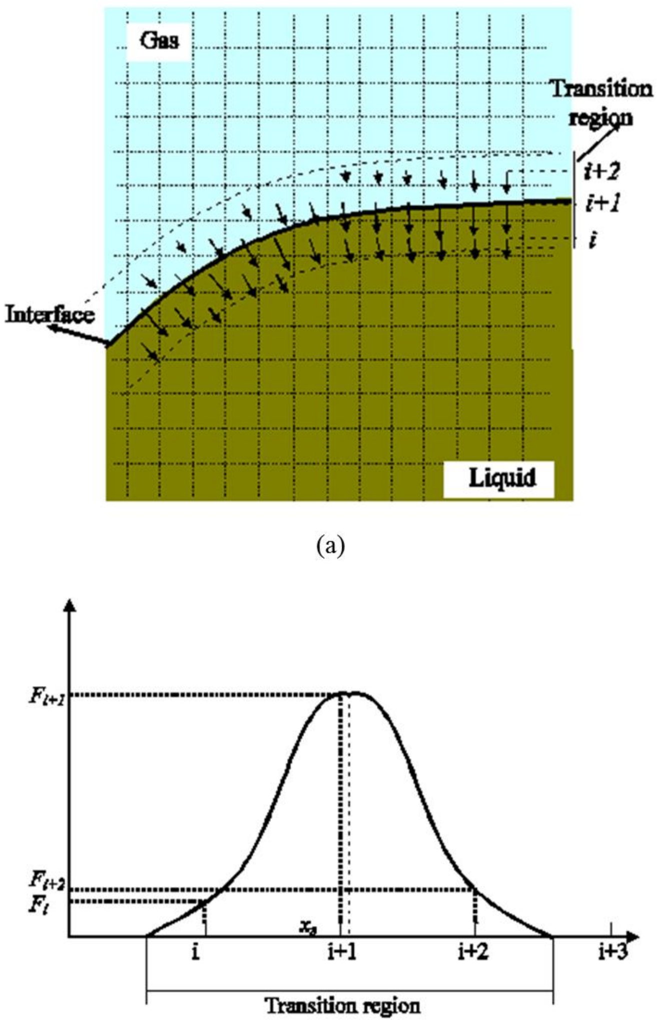

(a)

(b)

Figure 5-8 Distribution of Surface Tension Forces in the CSF Model (a); Variation of the Magnitude of the Body Force across the Transition Region (b)

Chapter 6

Results and Discussion

6.1 Introduction

In this chapter, the numerical results of four fundamental microfluidic droplet operations in parallel-plate EWOD devices including transport, splitting, merging and dispensing are presented. The dispensing processes are simulated with three different reservoir designs, namely 'conventional reservoir', 'stripped reservoir' and 'TCC reservoir' designs. The accuracy of the numerical EWOD model is verified by comparing the numerical results with the corresponding experimental data. The robustness and versatility of the computational code are confirmed. Deionized (DI) water is used as the working liquid for all operations without including any other liquid as the medium filler. All relevant data are given in Table 6-1 in which the numerical configurations for each operation are also included.

The computational domains used for the present study are shown in Figure 6-1. For droplet transport, splitting and merging processes, the entire droplet is modeled since the numerical domains have small dimensions. Uniform square mesh with 0.05mm grid spacing is used for the three operations based on the results of their own grid convergence studies. As shown in Figure 6-2 (a)-(c), computations are performed with three different mesh sizes for the grid convergence tests. The results obtained from the three different grid sizes are very close, which indicates that grid convergence has been achieved. No-slip boundary conditions are implemented at all sides of the domain for all three operations. It should be noted that since the droplets are, by design, not expected to reach the boundary of the computational domains, the nature of the boundary condition is of no consequence.

For the dispensing process, larger numerical domains are used due to the large size of initial drop in the reservoir. The computational domain used for the dispensing process in the ‘conventional reservoir’ design is shown in Figure 6-1 (d). In order to conserve computational resources, symmetry is assumed and only half of the drop is modeled with computations performed on a domain of dimensions 30mm × 12mm. As shown in Figure 6-2 (d), calculations have also been conducted with three different grid sizes for the grid refinement study for the ‘conventional reservoir’ design. The results obtained from the three different grid sizes are very similar, which indicates that grid convergence has been achieved. Based on the results of the grid refinement study, uniform square mesh with 0.2mm grid spacing is adopted for the dispensing studies for all three designs. Similar computational domains are used for the ‘stripped reservoir’ and ‘TCC reservoir’ designs as well. Free-slip boundary conditions are implemented at all sides of the domain except for the left side where a continuative outflow boundary condition is used for droplet discharge. It should be noted that since the droplet is, by design, not expected to reach the top and right boundaries of the computational domain, the nature of the boundary condition is of no consequence. The bottom side is a symmetric axis where the free-slip boundary condition is applied.

The time step for the numerical computations is automatically adjusted during the course of calculations, which is taken as the minimum of the time step constraints for numerical stability of capillarity, viscosity and the Courant condition [109, 121, 123].

Droplet splitting and merging processes in the present study are mainly motivated by Walker and Shapiro [19] and Walker *et al*. [20], in which a Hele-Shaw type of flow model was used to solve the problem numerically. Due to the reason that the Reynolds number is small and the gap distance between the plates are much smaller than the droplet dimension, the convective terms were neglected from the Navier-Stokes equation, which, along with the continuity equation, were reduced to a Hele-Shaw type of equations as the governing equations for their numerical EWOD model [19]. The next study by Walker *et al*. [20], used identical Hele-Shaw governing equations to investigate droplet splitting, merging and transport processes in parallel-plate EWOD devices. The obtained numerical results demonstrated excellent match with the experimental data. However, since the original Navier-Stokes equations are used as the governing equations without neglecting the convective terms for the current study, it is fairly reasonable to believe that the current model could obtain even more accurate results than the studies in [19] and [20].

6.2 Dimensional Analysis

A dimensional analysis has been performed to assist the investigation of the fluid dynamics of microfluidic droplet motions in parallel-plate EWOD devices. Certain key non-dimensional groups have been evaluated with the values listed in Table 6-1. It is understood that certain aspects of microfluidic droplet motions can be characterized by these non-dimensional numbers.

The variables closely associated with the current microfluidic problems include droplet density ρ, dynamic viscosity μ and surface tension coefficient at the gas-liquid interface σ, U_R the reference velocity which makes the maximum non-dimensional velocity close to unity, H the channel height between the parallel plates and g the gravity acceleration. The microfluidic flow is laminar since the Reynolds numbers ($Re = \rho U_R H/\mu$) are small (between 1.12 and 11.2) for all droplet operations. The Capillary number ($Ca = \mu U_R/\sigma$), the Weber number ($We = \rho {U_R}^2 H/\sigma$) and the Ohnesorge number ($Oh = \mu/\sqrt{\rho\sigma H}$) are all much smaller than unity, which indicates that the surface tension force is much more dominant than the viscous and inertia forces. It is also found that the Bond numbers ($Bo = \rho g H^2/\sigma$) are much smaller than unity. Consequently, the gravity force is neglected and the surface tension force is the sole constituent of body force term in the Navier–Stokes equations.

6.3 Droplet Transport

Numerical simulations of micro droplet transport in a parallel-plate EWOD device have been performed. The numerical setup and droplet physical properties given in Table 6-1 are same as the experiment [31]. The channel height between the two parallel plates is 0.1mm unless specified otherwise. The computational domain used for the transport process is shown in Figure 6-1 (a) with dimensions 4.8mm × 2.8mm. Due to lack of static contact angle values in the experimental results, 117° is used for $\theta_{b,OFF}$ following a previous electrowetting-based droplet splitting study [20]. The optimum value of $\theta_{b,ON}$ is subsequently set to 54° by matching the droplet shape in the numerical simulation with the experiment.

The transport process with snapshots at various time instants is shown in Figure 6-3. Two square electrodes of 2×2mm^2 are set as ON and OFF from left to right for the entire transport process except for the initial condition in which the electrodes are set reversely instead to prevent the droplet from returning to circular shape (Figure 6-3 (a)). With the electrowetting force pinning the interface at the four corners, the droplet was stretched into square shape except the small curves at the corners as shown in the experiment. Since this quasi-square shape is difficult to prescribe as the initial condition in the numerical simulation, a square droplet with 2mm length is used with the gas-liquid interface aligning with the electrode boundary and the size comparable to the experiment.

As soon as the left electrode is activated together with the right electrode deactivated simultaneously, the gas-liquid interface starts to deform due to the pressure difference across the droplet boundary as indicated by Equation (3-6). The interfaces at the corners first develop into smooth curves instantaneously due to the extremely large surface tension force in the x-y plane. After the droplet deforms into circular shape, the interface on the left side starts moving towards the activated electrode due to the surface tension force induced by the electrowetting effect. Meanwhile, the interface close to the border of the two electrodes gradually changes from convex to concave shape, which leads to the formation of a neck (Figure 6-3 (b)). It is of great importance to note that the difference between curvatures $\kappa_{z,OFF}$ and $\kappa_{z,ON}$ not only creates the internal pressure gradient which drives the droplet from the OFF to the ON region, but also results in a pressure jump where the droplet interface cuts the ON/OFF electrode border. This pressure jump may lead to the formation of two localized areas, one on each side, adjacent to the border with a larger pressure gradient induced (Figure 6-3 (b) and Figure 6-4). These localized areas directly determine the direction and speed of the fluid flow moving towards the activated electrode and consequently play a dominant role in the droplet deformation throughout the transport process. As the transport process continues, the liquid is gradually filling up the ON electrode with the droplet leading edge becoming wider than the trailing edge (Figure 6-3 (c) and (d)). With more liquid flowing to the activated electrode, a rapid increase of curvature κ_{xy} takes place at the tip of the trailing edge, which creates a larger pressure gradient and consequently a higher flow speed there (Figure 6-3 (e)). The fluid motion finally ceases when the liquid has completely settled on the ON electrode, which marks the end of the transport process (Figure 6-3 (f)). As shown in Figure 6-3, the numerical results are in excellent agreement with the experiment.

There are three adjustable parameters in the numerical model: Δ_R, Δ_A and λ_{vs}. Due to lack of information on contact angle hysteresis for the experiments, Δ_R and Δ_A are assumed to have the same value. The optimum hysteresis angles which best match the experiments are reported in Table 6-1. Optimum λ_{vs} is subsequently determined by matching the time scale of the numerical simulation with the experimental results.

It is discovered that the droplet shape has little variation if the initial condition is set as circular with identical droplet volume instead (Figure 6-5). Unlike the square-shape case in which the curvature κ_{xy} has an extremely large magnitude at the corners, κ_{xy} is uniform with a much smaller magnitude for the circular-shape case. However, it is found that the difference in κ_{xy} in the initial conditions only affects the opening stage of transport due to a much more dominant effect of κ_z on the transport process. Since $\Delta\kappa_z$ is completely independent of initial droplet shape and has identical magnitude in these two cases, the pressure fields within the droplets have almost the same distributions (Figure 6-6), which consequently leads to the very similar droplet shapes throughout the transport process.

A parametric study has been conducted in which the effects of static contact angles, contact angle hysteresis, viscous stress, channel height, electrode size and droplet physical properties on the transport process have been investigated. Droplets of circular shape are used as the initial conditions of all cases for the purpose of eliminating the non-uniformity of κ_{xy} when square or other non-circular shapes are applied. As a consequence, the droplet motion is primarily controlled by $\Delta\kappa_z$ at the opening stage of transport process.

According to Equation (3-5), the magnitude of κ_z can be modified by varying the static contact angles at the bottom plate, which will alter droplet shape and moving speed during the transport process (Figure 6-7). When the static contact angles at the bottom plate are set as 44° and 127° for the ON and OFF electrodes, respectively, both $\Delta\kappa_z$ and the pressure jump at the ON/OFF electrode border become larger than the reference case with 54° and 117° for $\theta_{s,ON}$ and $\theta_{s,OFF}$, respectively. This change in static contact angles creates greater internal pressure gradient and more curved pressure contours in the localized areas as soon as the transport takes place (Figure 6-8 (a)). On the other hand, the pressure gradient away from the localized areas is much smaller, which results in a much slower flow speed at the trailing edge. As a consequence, the liquid flowing towards the activated electrode mostly comes from the area adjacent to the ON/OFF electrode border where a much higher flow speed is also induced. At the opening stage of transport, the interface near the ON/OFF electrode border keeps shrinking towards the center and swiftly deforms from convex to concave shape while the interface at the trailing edge experiences only a slight deformation (Figure 6-7 (a) and Figure 6-8 (b)). As the transport process continues, the liquid near the ON/OFF electrode border maintains a much larger moving speed than the trailing edge. A neck is gradually formed at the ON/OFF electrode border with plenty of liquid trailing within the OFF electrode (Figure 6-7 (b) and (c)) which ultimately breaks off and splits the droplet into two small ones staying separately on the ON and OFF electrodes (Figure 6-7 (d)). The pressure and velocity profiles at key time instants are shown in Figure 6-8, which provides some vital information for this transport process.

When $\theta_{s,ON}$ and $\theta_{s,OFF}$ are set as 74° and 97° respectively, the magnitude of $\Delta\kappa_z$ is significantly reduced and κ_{xy} becomes more dominant. This switch of dominance from $\Delta\kappa_z$ to κ_{xy} considerably alters the pressure distributions within the droplet as well as the direction and speed of the fluid flow. As shown in Figure 6-9 (a), the pressure contours near the ON/OFF electrode border are much less curved than the 44°/127° case at the opening stage of transport. As a result, the localized areas are absent here and the liquid flowing towards the ON electrode primarily comes from the center of the droplet rather than the area adjacent to the ON/OFF electrode border. This change in flow direction offers adequate explanations for the phenomenon that the droplet has an elliptical shape during the transport without the formation of a neck (Figure 6-7 (i)). As the transport process continues, the leading edge gradually becomes wider than the trailing edge where κ_{xy} has a larger magnitude than that at the droplet front (Figure 6-7 (j)). Since the transport process is primarily controlled by κ_{xy} in this case, the fluid flow at the trailing edge now has a larger speed (Figure 6-9 (c)), which rapidly pulls the interface remaining on the OFF electrode towards the activated area (Figure 6-7 (k)). With more fluid flowing onto the ON electrode, the droplet finally fills the activated area without splitting (Figure 6-7 (l)). Note that the transport process takes as long as 160ms due to a much reduced pressure gradient within the droplet when the difference between $\theta_{s,OFF}$ and $\theta_{s,ON}$ is as small as 23°. The pressure and velocity profiles at key time instants are shown in Figure 6-9.

The transport process has also been carried out with different combinations of $\theta_{s,ON}$ and $\theta_{s,OFF}$ while keeping all other parameters unchanged. The results are given in Table 6-2 and the transport time versus dimensionless curvature $\tilde{k}$ is shown in Figure 6-10 in which $\tilde{k}$ is computed from Equation (3-9). It has been found that the droplet experiences a larger deformation as $\tilde{k}$ increases and that a critical value of $\tilde{k}$ exists somewhere between 12.612 and 13.240 beyond which splitting occurs during the transport. When $\tilde{k}$ is smaller than this critical value, the transport time decreases as $\tilde{k}$ increases from 4.485 to 10.934; then slightly increases with $\tilde{k}$ when $\tilde{k}$ varies from 10.934 to 12.612. The reduction in the transport time when $\tilde{k}$ is between 4.485 and 10.934 mainly results from the increasing pressure difference across the droplet boundary as the difference between $\theta_{s,OFF}$ and $\theta_{s,ON}$ becomes larger, which accelerates the transport speed. When $\tilde{k}$ increases from 10.934 to 12.612, the slight increase in the transport time is primarily due to the narrower neck formed in the middle of the transport process (Figure 6-11), which creates a smaller bottleneck for the flow trailing from the OFF electrode and consequently lengthens the transport time. When $\tilde{k}$ further increases to beyond the critical value, $\Delta\kappa_z$ becomes much more dominant than κ_{xy} and splitting occurs as a result of a much larger pressure gradient and more curved pressure contours in the localized areas as explained previously.

The results of transport time versus static contact angle in the current study are in general agreement with the findings reported in the literature in which the droplet transport velocity was found to increase with the applied electrical voltage [10, 22, 37, 38, 41]. Since a higher voltage applied at the droplet boundary generally produces a smaller value of $\theta_{s,ON}$ and therefore a greater difference between $\theta_{s,ON}$ and $\theta_{s,OFF}$, the same conclusion can be drawn from these findings that the transport speed increases with the difference between $\theta_{s,ON}$ and $\theta_{s,OFF}$. Furthermore, the present results agree especially with the phenomena observed by Lu [22] that the average transport velocity would increase with the applied voltage and then slightly decreased after the voltage was beyond a threshold value. It was also found in Lu's simulations that the droplet shape experienced a larger deformation as the voltage increased. Additionally, it was discovered by Pollack *et al*. [10] that the droplet would split apart when the voltage is beyond 60V, which is also consistent with the results obtained in the present study.

The effect of contact angle hysteresis on the transport process has been studied by altering the hysteresis angles in Equations (5-32)-(5-35) while keeping the assumption that Δ_R and Δ_A have the same value. In general, the difference between the receding and advancing contact angles will be decreased (or increased) if a larger (or smaller) hysteresis angle is applied, which will affect the pressure gradient within the droplet and eventually the overall transport process. However, as shown in Figure 6-12, it has been found that the hysteresis has only slight effects on both the droplet shape and time scale of the transport process since the hysteresis angle is much smaller than the static contact angles and therefore only plays a minor role in the transport process.

The viscous stress exerted by the two parallel plates can be varied by adjusting the multiplication factor λ_{vs} in Equations (3-11) and (3-12). The transport processes for λ_{vs}=9, 18 (reference case) and 72 are shown in Figure 6-13, which shows that the transport time increases with viscous stress but the droplets display the same pattern during the entire process. Since both κ_{xy} and $\Delta\kappa_z$ are independent of the viscous force, the pressure distributions within the droplet are not affected by the variation of viscous stress (Figure 6-14) even though the transport times differ by a factor of 6. The transport process has also been carried out with various viscous stress coefficients between 9 and 72 and it has been found that the transport time increases almost linearly with λ_{vs} as shown in Figure 6-15.

The channel height is expected to affect the pressure gradient within the droplet as well as the viscous force exerted by the plates according to Equations (3-6), (3-11) and (3-12). The transport processes for H=0.06mm, 0.1mm (reference case) and 0.2mm are shown in Figure 6-16. When the channel height is reduced to 0.06mm, both $\Delta\kappa_z$ and the pressure jump at the ON/OFF electrode border increase according to Equation (3-6). The pressure contours in the localized areas become more curved than the reference case, which further alters the speed and direction of the fluid flow adjacent to the ON/OFF electrode border (Figure 6-17 (a)). Even though the viscous force also becomes larger when channel height is reduced, the droplet shape is independent of the wall shear stress which only has the retarding effect on transport time as demonstrated previously. Therefore, similar to the case with 44°/127° static contact angles, the droplet interface experiences a large deformation at the localized areas during the transport (Figure 6-16 (a)-(c)), which eventually leads to the splitting at 37ms (Figure 6-16 (d)). The entire transport process takes 40ms, twice as long as the 44°/127° case due to the increased viscous force. The pressure and velocity profiles at key time instants are shown in Figure 6-17.

On the other hand, the droplet transports with an elliptical shape when the channel height is 0.2mm instead (Figure 6-16 (i)), resulting from the less curved pressure contours within the droplet (Figure 6-18 (a)). The pressure gradient is also smaller near the ON/OFF electrode border due to a reduced pressure jump across the border when the channel height increases. The transport process is similar to the case with 74°/97° static contact angles except that the entire transport process only takes 20ms since the viscous stress is significantly reduced (Figure 6-16 (l)). The pressure and velocity profiles at key time instants are shown in Figure 6-18.

Additional channel heights have been studied for the 2×2mm^2 electrode size and the results of transport time versus channel height are given in Figure 6-19. It has been found that the splitting does not occur when the channel height is greater than a certain critical value between 0.08mm and 0.09mm. Beyond this critical value, the pressure jump is insufficient to bend the pressure contours near the ON/OFF electrode border to create the localized areas. When splitting is absent, the transport speed increases with the channel height due to the reduced viscous stress. Even though the pressure difference across the droplet boundary is also reduced as channel height increases, the decrease in wall shear stress is apparently more significant than the reduction in pressure difference. The transport time is found to reduce from 59ms to 18ms as the channel height increases from 0.09mm to 0.25mm. However, the decrease in transport time becomes very minimal when H is larger than 0.2mm, which agrees with the findings of Bahadur and Garimella [37] that the transport speed was of negligible dependence on the channel height when H

varied between 0.3mm and 0.7mm. Moreover, it is discovered that the droplet shape experiences a larger deformation when the channel height is reduced, which is consistent with the results obtained by Pollack *et al*. [34].

When the electrode size is altered with the droplet diameter maintained at the same ratio with the electrode length, the magnitude of κ_{xy} will vary reversely with the droplet size. The magnitude of κ_z, however, remains the same since neither the contact angles nor the channel height are modified. As a result, the effect of κ_z on the transport process becomes more (or less) dominant when the electrode size increases (or decreases), which changes the pressure distributions within the droplet and consequently affects the droplet shape. The transport processes for 1×1mm^2, 2×2mm^2 (reference case), 3×3mm^2 and 4×4mm^2 electrode sizes are shown in Figure 6-20. When the electrode size increases from 1×1mm^2 to 4×4mm^2, $\Delta\kappa_z$ becomes increasingly dominant which results in more curved pressure contours in the localized areas and eventually the splitting for the same reason given for the 44°/127° and H=0.06mm cases. The localized areas which exist for the 3×3mm^2 and 4×4mm^2 electrode sizes are absent for the 1×1mm^2 case due to a more dominant effect of κ_{xy} as shown in Figures 6-21-6-23 respectively, which eventually leads to the elliptical shape during the transport.

The transport processes are also conducted with various channel heights for 1×1mm^2, 3×3mm^2 and 4×4mm^2 cases. The results of transport time versus channel height are shown in Figures 6-24-6-26 and the details are given in Table 6-3 along with the results for 2×2mm^2 electrode size. It has been found that the splitting does not occur when the channel height is larger than 0.045mm, 0.14mm and 0.19mm for 1×1mm^2, 3×3mm^2 and 4×4mm^2 electrode sizes, respectively. The results of transport time versus dimensionless curvature based on the above numerical data are shown in Figure 6-27. It has been found that the critical $\tilde{k}$ value is around 13 for all electrode sizes, which is consistent with the value previously found in the parametric study of static contact angles. Below the critical $\tilde{k}$ value, the transport time increases with $\tilde{k}$ for all electrode sizes due to the increasing viscous stress as the channel height decreases.

The results of the parametric study on droplet physical properties are shown in Figure 6-28. It has been found that increase in density or viscosity reduces droplet speed and consequently delays the transport process since it is more difficult to move a droplet with the same pressure force if the fluid is heavier or more viscous. On the other hand, the capillary induced pressure difference across the droplet boundary increases with the surface tension coefficient which accelerates the droplet motion and reduces the transport time. The droplet shape does not appear to vary much with density, viscosity or surface tension.

6.4 Droplet Splitting

Numerical simulations of droplet splitting in a parallel-plate EWOD device have been performed and the numerical configurations given in Table 6-1 are same as the experiment [20]. The droplet splitting process with snapshots at various time instants is shown in Figure 6-29. Three electrodes, 1.4 mm in length, are set at 25V, 0V and 25V from left to right for the entire splitting process with a channel height of 0.07mm. Initially, the droplet with a radius of 0.990mm is placed at the middle electrode with all three electrodes set at 0V (a). As soon as the electrodes on the left and right are activated to 25V simultaneously, a pressure difference is created within the droplet between the OFF and ON regions as indicated by Equation (3-6) and the gas-liquid interface starts to deform. The interfaces on the left and right of the droplet move sideways filling the 25V electrodes due to the reduced surface tension force there while the interfaces at the top and bottom shrink towards the center with the curvatures decreasing from a positive to a negative value as the interfaces turn from convex to concave. Meanwhile, the curvatures on the left and right sides experience only a small increase as they move towards the activated regions (b). As more fluid fills the 25V electrodes, a neck starts to develop at the center of the 0V electrode and the interfaces at the top and bottom continue shrinking (c-d). With more liquid going sideways, the neck eventually breaks off resulting in the formation of two smaller droplets of similar size (e). During pinch-off, there is a rapid change of curvature at the tips which creates a large pressure gradient and consequently a higher flow speed there. The fluid motion continues until the liquid has completely left the 0V region and settles on the 25V electrodes, which marks the end of the splitting process (f). As shown in the figure, the results are in excellent agreement with the experiment. The flow and pressure fields at selected instants are shown in Figures 6-30 and 6-31 respectively.

A parametric study has been performed in which the effects of channel height and several other parameters on the splitting process have been studied. The channel height H is expected to affect the surface tension induced pressure as well as the viscous force exerted by the plates according to Equations (3-6), (3-11) and (3-12). The droplet motion could be either accelerated or retarded depending on which effect being more dominant. For H in the range of 0.045mm and 0.1mm, the splitting process displays the pattern shown in Figure 6-29 except that the splitting time increases with H. The splitting time versus channel height is plotted in Figure 6-32 which shows a dramatic increase in splitting time when H goes beyond 0.09mm and splitting ultimately ceases at 0.105mm. The increase in channel height leads to a reduction of pressure difference at the droplet boundary, which has a more dominant effect than the reduction in wall shear stress. Consequently, the interface moves at a lower speed and the splitting time becomes longer.

When the channel height varies between 0.03 and 0.04mm, a satellite droplet would be formed at the end of the splitting process as shown in Figure 6-33 for H = 0.035mm. Similar to the droplet transport case, the localized areas with larger pressure gradient are created near the ON/OFF electrode border when H is of a small value (Figure 6-34), which determine the direction of fluid flow moving towards the activated electrodes and play a dominant role in the droplet deformation throughout the splitting process. When H is reduced from 0.07mm to 0.035mm, greater internal pressure gradients and more curved pressure contours are created at the localized areas due to the increased pressure jump at the ON/OFF electrode border, which consequently alters the direction of the fluid flow in the localized areas and gives the liquid a larger moving speed (Figure 6-35). As shown in Figure 6-33, the interface near the ON/OFF electrode border swiftly deforms from a convex into a concave shape at the opening stage of splitting while the interface at the top and bottom of droplet experiences only a slight deformation (Figure 6-33 (b)). As the splitting process continues, a long neck of nearly uniform width is formed on the OFF electrode, which is completely different from the neck when H = 0.07mm. With more liquid flowing onto the ON electrodes, the fluid close to the ON/OFF electrode border is finally depleted, which results in two pinch-off locations and the subsequent formation of a satellite droplet at the center of the OFF electrode. It is important to note that the mechanism for the satellite droplet formation is identical to that for the splitting in the transport cases, both of which is due to the more curved pressure gradient in the localized areas when the channel height is reduced.

When H is increased to 0.15mm, the pressure difference across the droplet boundary will be reduced according to Equation (3-6) and the spitting will not occur as shown in Figure 6-36. During the splitting process, $k_{xy,OFF}$ keeps decreasing as the interfaces at the top and bottom of the droplet turn from convex into concave shape while

$k_{xy,ON}$ remains almost constant as the liquid fills the activated electrodes. As a result, the pressure difference across the droplet keeps decreasing. When the channel height increases to a certain value, the pressure difference will eventually reach zero during the splitting process according to Equation (3-6) and the interface movement will stop. This is in general agreement with the findings of [11] in which a critical channel height value between 0.07mm and 0.15mm has been reported.

The results of the parametric study on the physical properties are shown in Figure 6-37. It has been found that increase in density or viscosity will reduce droplet speed and consequently delay the splitting process since it is more difficult to move a droplet with the same pressure force if the fluid is heavier or more viscous. On the other hand, the capillary induced pressure gradient across the droplet boundary increases with the surface tension coefficient which accelerates the droplet movement and reduces the splitting time. The droplet shape does not appear to vary much with density, viscosity or surface tension.

6.5 Droplet Merging

Numerical simulations of droplet merging in a parallel-plate EWOD device have been conducted and the numerical configurations given in Table 6-1 are same as the experiment [20]. The droplet merging process with snapshots at various time instants is shown in Figure 6-38. Three electrodes, 1.5 mm in length, are set at 0V, 65V and 0V from left to right during the entire process with a channel height of 0.1mm. It should be mentioned that the initial droplets in the experiment are non-circular with slightly uneven size which is difficult to prescribe as initial conditions in the numerical simulation. Instead, the end result of a splitting process is used which consists of two droplets aligned symmetrically with the sizes comparable to the experiment (a). As soon as the middle electrode is activated, a pressure imbalance is created at the droplet boundary and the two droplets start to move towards each other (b-c). The merging of the two droplets occurs as soon as they collide and continues due to the existing pressure difference across the droplet boundary (d-e). The movement eventually ceases when the 65V electrode is filled up with liquid (f). Again, as shown in the figure, the results are in good agreement with the experiment. The flow and pressure fields at selected instants are shown in Figures 6-39 and 6-40 respectively.

A parametric study has also been conducted to investigate the effects of channel height and droplet physical properties on the merging process. It has been found that droplet merging always occurs regardless of the channel height although at a faster pace when H is increased. Apparently, the decrease in wall shear stress is more significant than that of the reduction in pressure difference across the droplet boundary as the channel height increases. Thus the droplet has a higher transport speed which expedites the merging process as shown in Figure 6-41. Furthermore, the droplet experiences a smaller deformation as it moves towards the middle electrode as H increases, which results from the less curved pressure contours in the localized areas near the ON/OFF electrode border as explained previously in the study of droplet transport process. As shown in Figure 6-42, the droplet has a more rounded contour before the merging takes place when H= 0.6mm. The results of the parametric study on the physical properties are shown in Figure 6-43, which are similar to the findings for the splitting process that altering the density, viscosity or surface tension only changes the time scale of merging process with negligible effect on droplet shape.

6.6 Droplet Dispensing

Numerical simulations of micro droplet dispensing in parallel-plate EWOD devices with three different reservoir designs, namely 'conventional reservoir' (Figure 6-44), 'stripped reservoir' (Figure 6-45) and 'TCC reservoir' (Figure 6-46), have been performed alongside an experimental study [31]. For each design, fifty droplets are consecutively dispensed from the reservoir. The channel height between the two parallel plates is 0.1mm and the size of the generating electrode is $2\times2\text{mm}^2$ for all three designs. The ‘conventional reservoir’ design has been used in many microfluidic droplet dispensing experiments in which the reservoir site consists of one single electrode of rectangular or square shape [17, 18, 21, 45]. The electrical voltage is applied throughout the reservoir whenever the reservoir electrode is activated. Two electrodes with squared shape and much smaller sizes are located on one side of the reservoir, which serve as the droplet generating and cutting sites. Each of these three electrodes can be switched ON and OFF independently. The 'Stripped reservoir' design is similar to the ‘conventional reservoir’ design except that the reservoir electrode is divided into ten strips of equal size. Each of these ten strips can be switched ON and OFF independently as needed. The 'TCC reservoir' design consists of a T-shape electrode as the cutting site and several C-shape electrodes as the reservoir. Each electrode can also be switched ON and OFF independently to move the droplet towards the cutting and generating sites step by step and complete the dispensing process. In the special design of the 'TCC reservoir', a much shorter cutting length can be achieved with a much narrower range of pinch-off locations. It was hoped that with the pinch-off position under control, droplet volume is hardly affected by the shape and volume of the liquid in the reservoir, which would lead to a smaller droplet volume inconsistency. Furthermore, the droplet generated from the ‘TCC reservoir’ design has a similar size to the generating electrode since the liquid added to the generated droplet after the pinch-off is much reduced. More details of these three designs can be obtained from Yaddessalage [31].

A typical dispensing process has three essential stages: (1) Filling stage: liquid in the reservoir flows into the generating and cutting electrodes until the two electrodes are filled up; (2) Cutting stage: the gas-liquid interface shrinks towards the center of the cutting electrode until the neck pinches off with a small droplet created on the generating electrode. (3) Discharging stage: the droplet generated on the cutting electrode is discharged from the EWOD device. Since it is rather difficult to ascertain that the filling stage has reached the steady state by simply observing the motion of liquid interface, the duration for the filling stage is set to a relatively large value in both experiments and numerical simulations in order to minimize the interference due to insufficient filling time on the dispensing process.

For the dispensing process in the ‘conventional reservoir’ design, a large drop of irregular shape is initially placed in the reservoir with the liquid boundary marginally touching the cutting electrode in the experiment (Figure 6-44 (a)). Droplets are then dispensed consecutively from the reservoir by running the cycles of filling, cutting and discharging stages repeatedly (Figure 6-44 (b)-(e)) until all fifty droplets have been generated. It should be mentioned that this irregular shape is difficult to prescribe as the initial condition in the numerical simulation. Instead, a droplet of circular shape is used with the size comparable to the experiment. It is believed that the effect of the initial condition on the dispensing process is negligible.

The numerical and experimental results of a typical dispensing process for the ‘conventional reservoir’ design are shown in Figure 6-47. As given by Equation (3-6), a pressure difference is created across the liquid boundary when the cutting and generating electrodes are switched ON with the reservoir electrode switched OFF simultaneously. Liquid in the reservoir then moves into the two activated electrodes until they are filled up (a)-(b). When the cutting electrode is switched OFF as the reservoir electrode is turned back ON simultaneously, the menisci at the exterior corners of the cutting electrode shrink towards the center with a small neck developed due to the pressure gradient within the liquid (c). As more liquid in the neck flows back to the reservoir, the neck finally pinches off with a small droplet produced on the generating electrode (d).

As shown in Figure 6-47, liquid interface on the generating and cutting electrodes appears to have excellent agreement between the numerical and experimental results. However, there are two noticeable distinctions in the dispensing process. First, the liquid in the reservoir has a rounded shape in the experiment while the shape is non-circular in the numerical simulation. It is found that this non-circular shape is inherent in the numerical device and is already formed at the end of the filling stage of the 1st droplet (Figure 6-48 (b)). Since the generating and cutting electrodes have much smaller sizes compared to the reservoir where a large drop of a circular shape is situated as the initial condition, as soon as the filling stage takes place, the pressure contours within the droplet rapidly develop into a radial distribution as shown in Figure 6-49. It is of great significance to mention that the difference between curvatures $\kappa_{z,OFF}$ and $\kappa_{z,ON}$ not only creates the internal pressure gradient which drives the liquid from the OFF to the ON regions, but also results in a pressure jump at the points where the droplet interface cuts the border of the ON and OFF electrodes. This pressure jump leads to the formation of some localized areas where a much larger pressure gradient is induced than the rest areas, which directly determines the direction and speed of the fluid flow as well as the deformation of the liquid in the reservoir. As indicated by the pressure gradient, the liquid close to the cutting electrode has a larger moving speed towards the activated areas while the speed is much smaller elsewhere within the liquid. As a consequence, the interface in the localized areas shrinks towards the reservoir center in the filling stage, which rapidly shapes the interface into a flat line. Simultaneously, the liquid at the droplet trailing edge flows towards the top area as demonstrated by the pressure and flow fields, which results in the flat interface at the northeast corner of the droplet. It is observed that the radial distribution of the pressure contours sustains the entire filling stage which eventually results in the non-circular shape of the liquid in the reservoir.

The second distinction is the additional liquid accumulated at the exterior corners of the cutting electrode at the end of filling stage in the numerical simulation (Figure 6-47 (b)), which is absent in the experiment. This distinction appears to be a result of surface smoothness and contact angle hysteresis effect. It is known that the surface smoothness and the hysteresis angle are non-uniform which depend on the time and location in the experiment. When the generating and cutting electrodes are activated, the smoothness and the hysteresis effect of these two activated electrodes could be even more distinct than the non-activated areas, which might prevent the liquid from spreading outside the cutting electrode in the filling stage. The non-uniformity of the smoothness and hysteresis effect can be illustrated by the unsmooth contour of the generated droplet in the experimental results (Figure 6-47). In the numerical simulation, on the other hand, the surface smoothness is uniform and the hysteresis angle is constant and equal for Δ_R and Δ_A. After the generating and cutting electrodes are filled up, the effect of $\Delta\kappa_z$ is greatly reduced while κ_{xy} takes over the filling stage instead (Figure 6-50 (a)). Due to the concave shape of the liquid interface at the exterior corners of the cutting electrode where the magnitude of κ_{xy} is smaller than the rest areas, the liquid in the reservoir accumulates there to flatten the concave interface and compensate the imbalanced pressure force at the liquid contour (Figure 6-50 (b)).

The five stages of droplet dispensing for the ‘stripped reservoir’ design are given in Figure 6-45 (b)-(f) and the numerical and experimental results are shown in Figure 6-51. Similar to the ‘conventional reservoir’ design, a large droplet of irregular shape is placed in the reservoir initially. Prior to the start of filling stage for the 1^{st} droplet, the few stripped electrodes on the cutting electrode side are activated, which enables the filling of the left side of the reservoir with liquid (Figure 6-45 (a)). This special arrangement is a crucial step for the ‘stripped reservoir’ design which needs to be performed before every filling stage (Figure 6-45 (b)). After the liquid fills the first few stripped electrodes (Figure 6-51 (a)), the filling stage is initiated by activating the generating, cutting and first stripped electrode while keeping the rest deactivated. As a result, a long liquid-gas interface is created at the left reservoir boundary which sustains throughout the entire filling stage (Figure 6-51 (b)). After the generating and cutting electrodes are filled with liquid, the cutting electrode is then turned OFF and the entire ten stripped electrodes are turned ON. The liquid on the cutting electrode then flows back to the reservoir with a neck formed of the same shape as in the ‘conventional reservoir’ design (Figure 6-51 (c)). The neck finally pinches off with a small droplet produced on the generating electrode (Figure 6-51 (d)). Good agreement is achieved between the numerical and experimental results except for the accumulated liquid at the exterior corners of the cutting electrode for the same reason explained previously.

The five stages of droplet dispensing for the ‘TCC reservoir’ design are given in Figure 6-46 (b)-(f) and the numerical and experimental results are shown in Figure 6-52. Excellent agreement is achieved between the numerical and experimental results except for the liquid shape in the reservoir, which results from the same reason explained for the ‘conventional reservoir’ design.

Volume inconsistency of generated droplets has been examined both numerically and experimentally for all three designs. The details of the experimental results will be presented in a forthcoming paper. As shown in Figure 6-53, the ‘conventional reservoir’ design offers decent volume uniformity with volume reproducibilities of 0.744% and 0.740% for experimental and numerical results, respectively. However, all volumes are in the range of 0.52-0.55mm^3, which are at least 30% larger than the volume of the generating electrode (0.4mm^3). As discussed earlier, this additional volume primarily comes from the long neck formed in the cutting stage.

Different from the findings in some literature that the pinch-off location was responsible for the volume variation of the generated droplet [11, 21, 31], it has been found in the current numerical results that the pinch-off locations are fairly stable among droplets for the ‘conventional reservoir’ design (Figure 6-54 (a)). Instead, the section of liquid interface which cuts the left reservoir boundary at the end of filling stage varies and appears to play a significant role in the volume variation (Figure 6-54 (b)). As the droplet being dispensed, the liquid in the reservoir is accumulated at the left side since the pressure gradient close to the cutting electrode is much larger than the rest areas in the cutting stage (Figure 6-55). As a result, the intercept of the liquid interface at left reservoir boundary at the end of filling stage is found to move up for the first thirty five droplets as the slope of the interface increases progressively. The intercept then moves down for the last fifteen droplets due to the liquid in the reservoir getting depleted (Figure 6-56). The variation of intercept locations alters the pressure fields on the cutting electrode at the beginning of the cutting stage among droplets. Given the pressure fields within the generating electrode is relatively stable, the pressure gradient on the cutting electrode is actually in charge of the deformation of the neck in the cutting stage and eventually determines the amount of liquid adding to the generated droplet after the pinch-off.

Therefore, the pressure fields on the cutting electrode at the beginning of the cutting stage are extremely crucial for the volume of generated droplet.

To substantiate this point, the numerical results of a larger (11th) and a smaller droplet volume (31st) are shown in Figure 6-57. It is found that the intercepts are located at different places at the end of the filling stage due to the different slopes of interface section as discussed earlier. As soon as the cutting stage takes place, a larger pressure gradient is created on the cutting electrode for the 11th droplet since the intercept is closer to the cutting electrode and squeezes the pressure contours ((b) and (c)). The larger pressure gradient for the 11th droplet results in a slightly different neck right before the pinch-off (g) and eventually a droplet with a slightly larger volume than the 31st droplet (h). This correlation between the pressure gradient on the cutting electrode and the volume of generated droplet is also illustrated by the pressure fields at the beginning of the cutting stage for the 1st, 11th, 21st, 31st, 41st and 50th droplet (Figure 6-58). It is demonstrated that the pressure gradients on the cutting electrode are larger for the 1st, 11th, 21st and 50th droplet, which results in slightly larger volumes compared to the 31st and 41st droplet. In summary, when the intercept location at the end of the filing stage is closer to the cutting electrode, a larger pressure gradient will be formed on the cutting electrode at the beginning of the cutting stage, which leads to the generation of a droplet with slightly larger volume and vice versa. Note that the intercept location is not the sole factor controlling the droplet volume which can also be affected by some other elements such as the pinch-off location and the liquid volume remaining in the reservoir. Therefore, the variation of droplet volume does not necessarily have an exactly inverse relationship with the intercept location as shown in Figure 6-54 (b).

As for the ‘stripped reservoir’ design, the volume inconsistency is 0.437% for the experiment versus 0.426% for the numerical results (Figure 6-59). The improvement of volume inconsistency is mainly contributed from the long liquid-gas interface at the left reservoir boundary during the entire filling and cutting stages. This liquid-gas interface eliminates the intercept in the ‘conventional reservoir’ design and stabilizes the curvatures at the exterior corners of the cutting electrode at the end of the filling stage (Figure 6-60). Consequently, the pressure fields on the cutting electrode at the beginning of the cutting stage become steady among droplets which greatly reduce the volume variation. The numerical results of the 11th and 31st droplet are shown in Figure 6-61. It is found that the pressure fields on the cutting electrode at the beginning the cutting stage are very similar for these two droplets ((c) and (f)), which results in the overlapping curvatures before the pinch-off (g) and eventually the similar droplet volumes (h).

An interesting phenomenon in both the experimental and numerical results is that the volumes demonstrate a noticeable increase in the last few droplets (Figure 6-59). A comparison of the pressure fields between the 1st, 11th, 21st, 31st, 41st and 50th droplet shows that the pressure gradients on the cutting electrode are of similar patterns for the 1st, 11th, 21st and 31st droplet (Figure 6-62 (a)-(d)). However, as the liquid in the reservoir is almost depleted for the last few droplets, the gas-liquid interface becomes very close to the left boundary of the reservoir, which squeezes the pressure contours on the cutting electrode (Figure 6-62 (e)-(f)). Consequently, the pressure gradient becomes greater for the last few droplets and eventually leads to the increase of droplet volumes for the same mechanism given for the ‘conventional reservoir’ design.

To substantiate this point, another dispensing case has been performed for the ‘stripped reservoir’ design in which the initial liquid volume is increased by 12%. As shown in Figure 6-59, the new case has a smaller inconsistency of 0.326% without the noticeable increase in the last few droplets. It is shown in Figure 6-63 that that the pressure gradients on the cutting electrode display very similar patterns for the 31st, 41st and 50th droplet, which suggests that the liquid volume in the reservoir has negligible effect on the droplet as long as the reservoir is sufficiently filled.

As shown in Figure 6-64, the volume reproducibilities for the 'TCC reservoir' design are 0.333% and 0.331% for the experimental and numerical results, respectively. The pressure fields on the cutting electrode, shown in Figure 6-65, are very similar for the 11th and 31st droplet ((c) and (f)), which results in their similar volumes. A comparison of the pressure fields between the 1st, 11th, 21st, 31st, 41st and 50th droplet shows that the pressure fields on the cutting electrode display very similar patterns (Figure 6-66). Note that the reservoir is also almost depleted for the last few droplets but the pressure fields for the 41st and 50th droplet still display almost the same patterns, which suggests that the ‘TCC reservoir’ design is hardly affected by the liquid volume in the reservoir and has the best volume uniformity among the three designs. Another notable difference between the ‘TCC reservoir’ and the other two designs is that all volumes are within the range of 0.40-0.42mm^3, less than 5% over the generating electrode size (0.4mm^3). The numerical results appear to demonstrate the advantages of ‘TCC reservoir’ over the other two designs, which are especially favorable for the biomedical applications in which both the volume uniformity and controllability are of paramount importance.

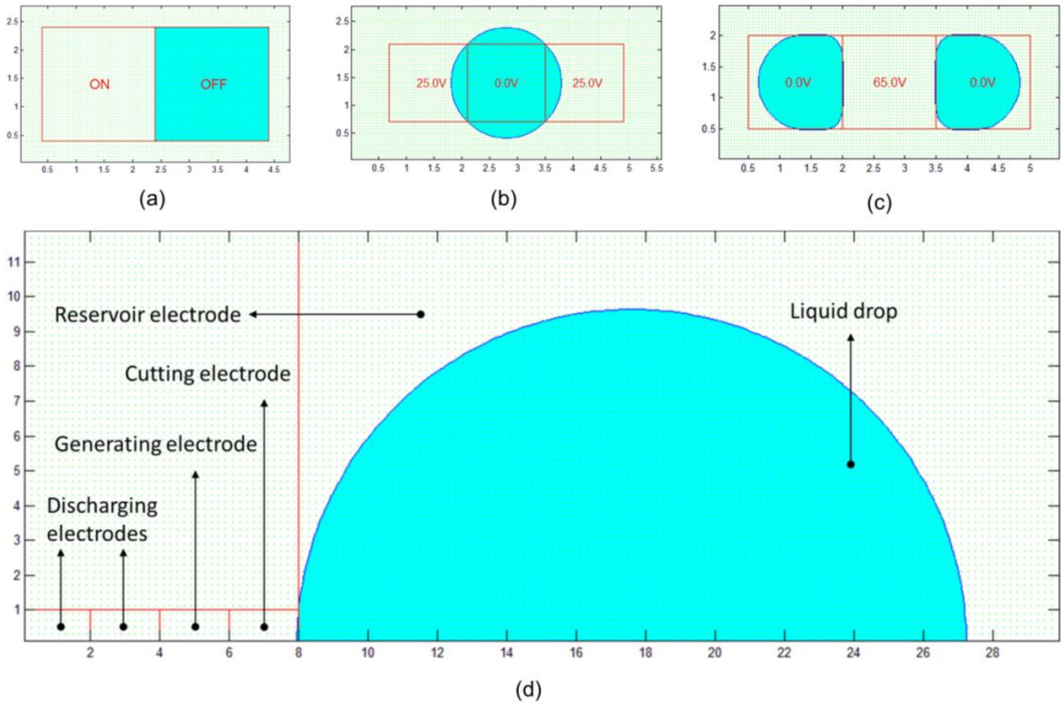

(a) (b) (c)

(d)

Figure 6-1 Computational Domains for Droplet Transport (a); Splitting (b); Merging (c) and Dispensing (d)

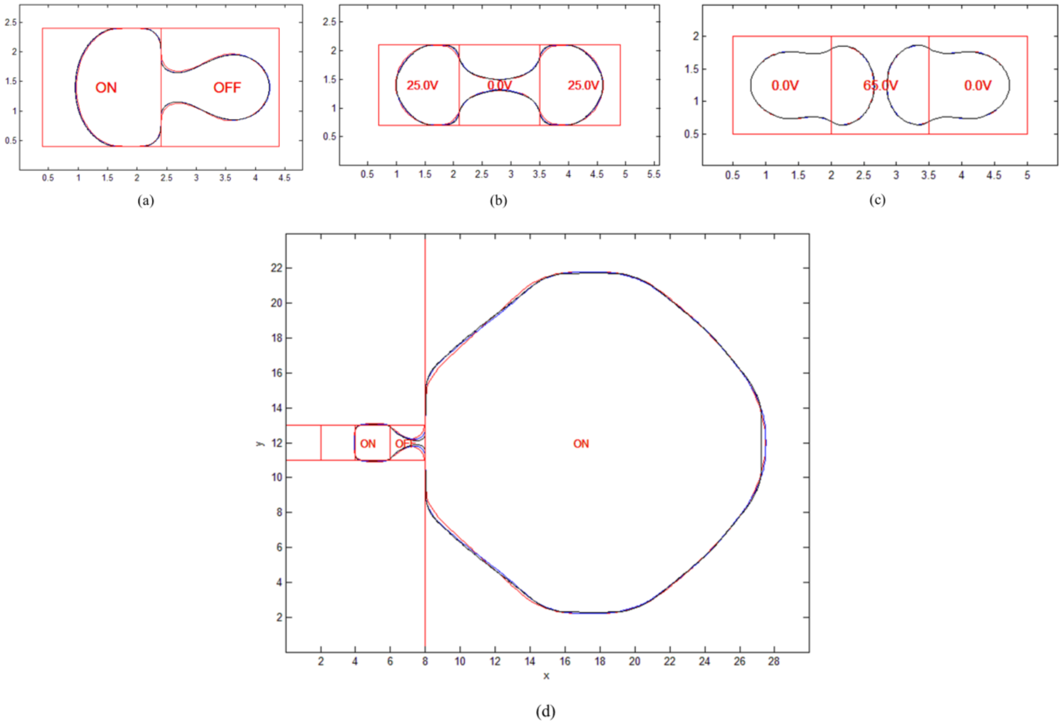

(a) (b) (c)

(d)

Figure 6-2 Grid Convergence Studies for Droplet Transport (a); Splitting (b); Merging (c) and Dispensing (d) with Different Grid Sizes: Red: 0.05×0.05; Blue: 0.025×0.025; Black: 0.0125×0.0125

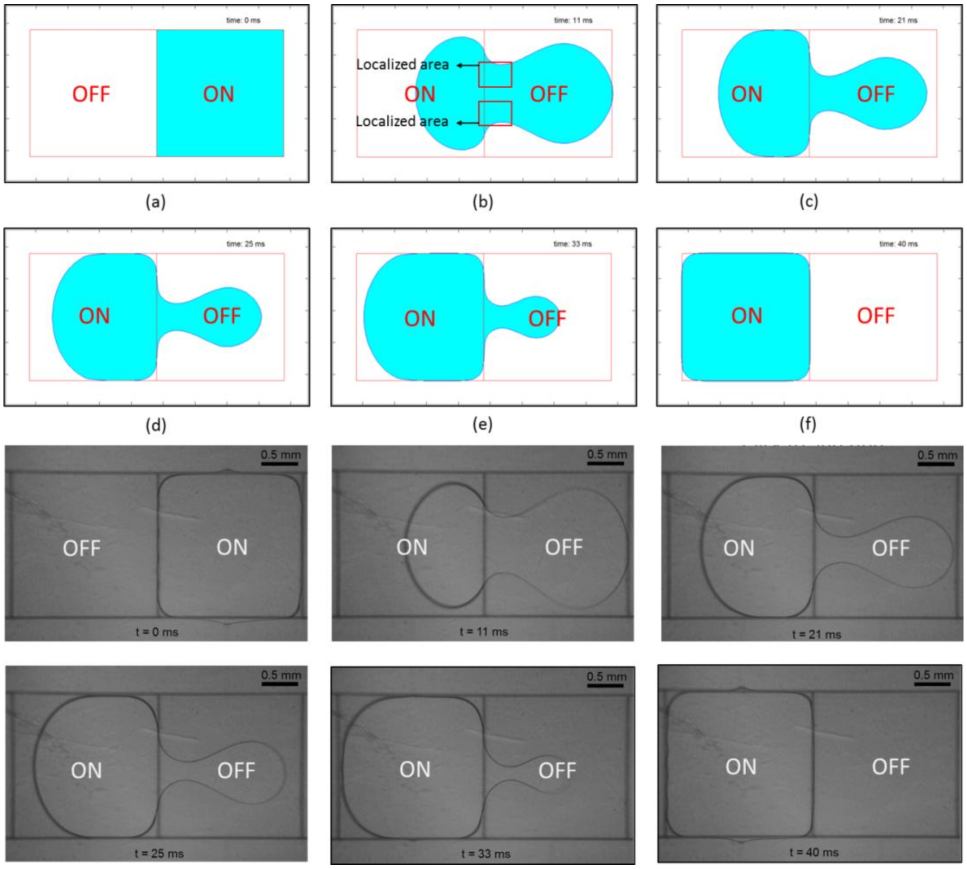

Figure 6-3 Droplet Transport: Numerical (Top) at t=0ms (a); t=11ms (b); t=21ms (c); t=25ms (d); t=33ms (e); t=40ms (f); Experimental (Bottom) [31]

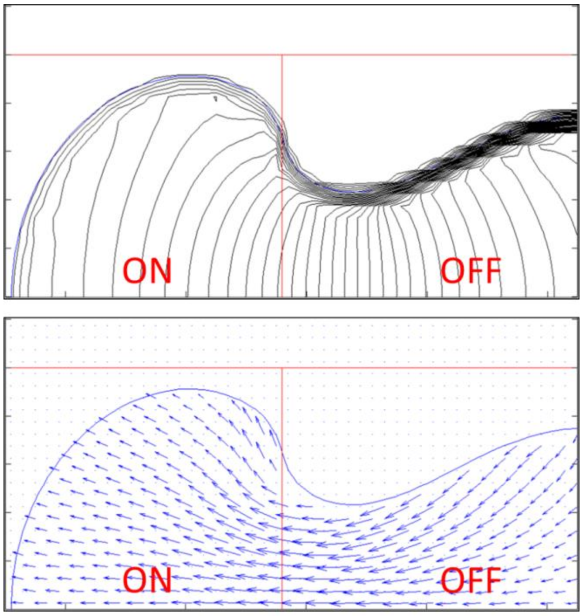

Figure 6-4 Pressure (top) and Velocity Fields (Bottom) at t=11ms (Only Top Half of the Droplet is Shown)

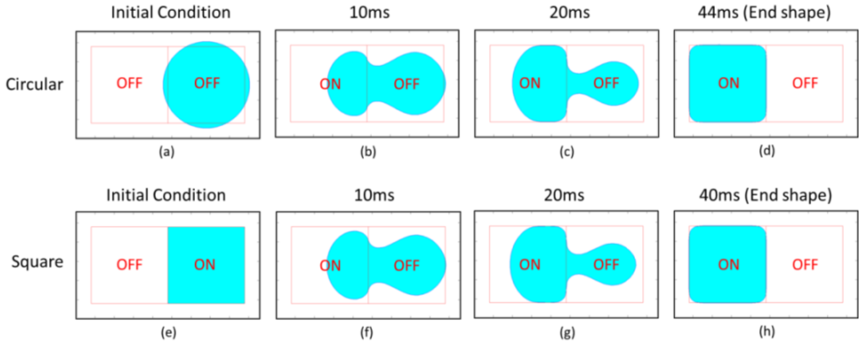

Figure 6-5 Droplet Transport with Different Initial Conditions: Circular Shape (a)-(d); Square Shape (e)-(h)

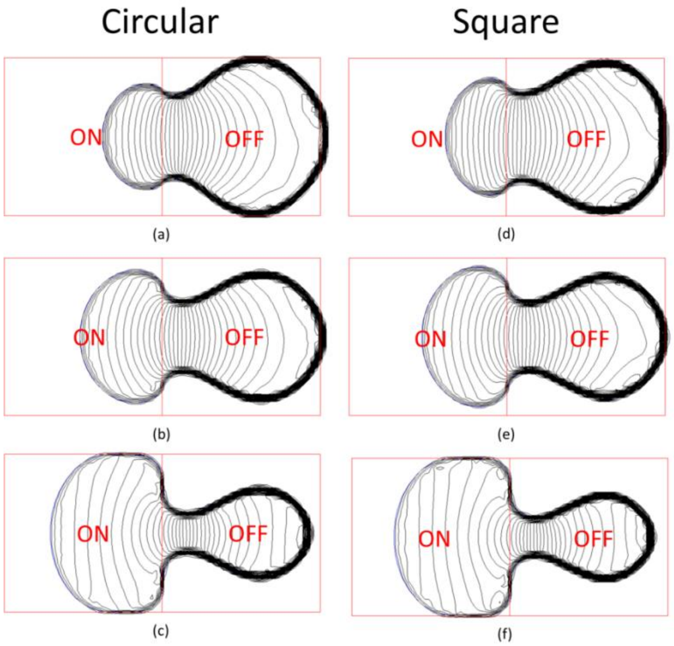

Figure 6-6 Pressure Fields for Different Initial Conditions: Circular Shape at t=5ms (a); t=10ms (b); t=20ms (c); Square Shape at t=5ms (d); t=10ms (e); t=20ms (f)

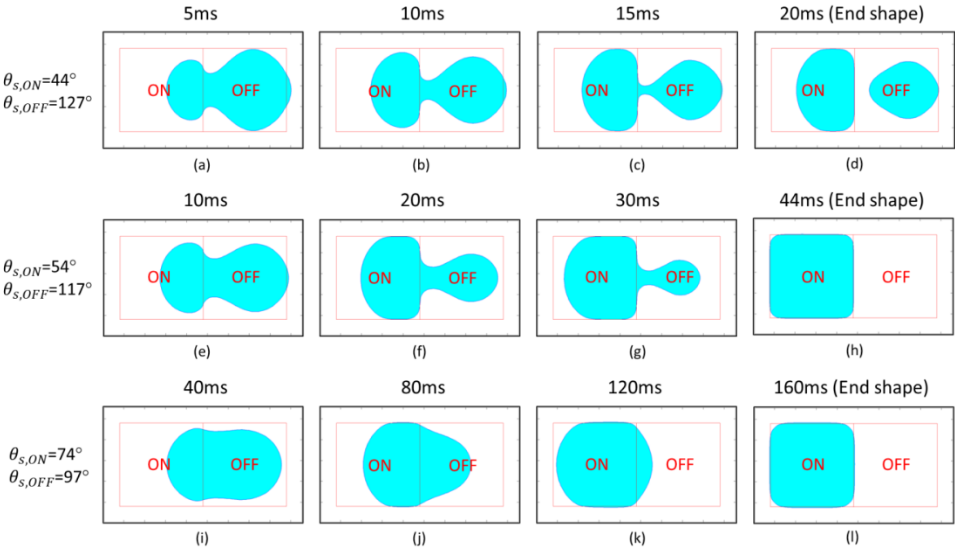

Figure 6-7 Droplet Transport with Different Static Contact Angles: $\theta_{s,ON}$=44° and $\theta_{s,OFF}$=127° (a)-(d); $\theta_{s,ON}$=54° and $\theta_{s,OFF}$=117° (e)-(h); $\theta_{s,ON}$=74° and $\theta_{s,OFF}$=97° (i)-(l)

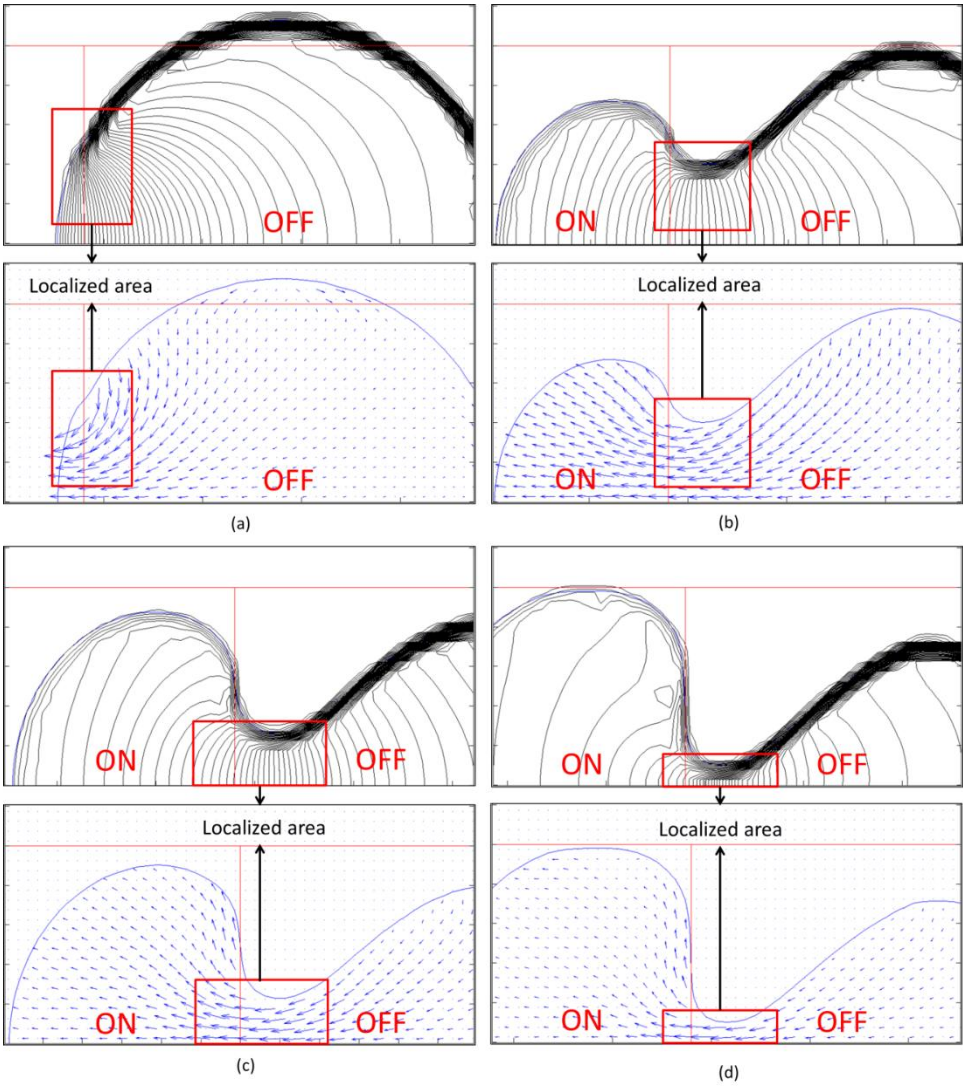

Figure 6-8 Pressure (Top) and Velocity Fields (Bottom) for $\theta_{s,ON}$=44° and $\theta_{s,OFF}$=127° at t=0.1ms (a); t=5.0ms (b); t=10.0ms (c); t=15.0ms (d)

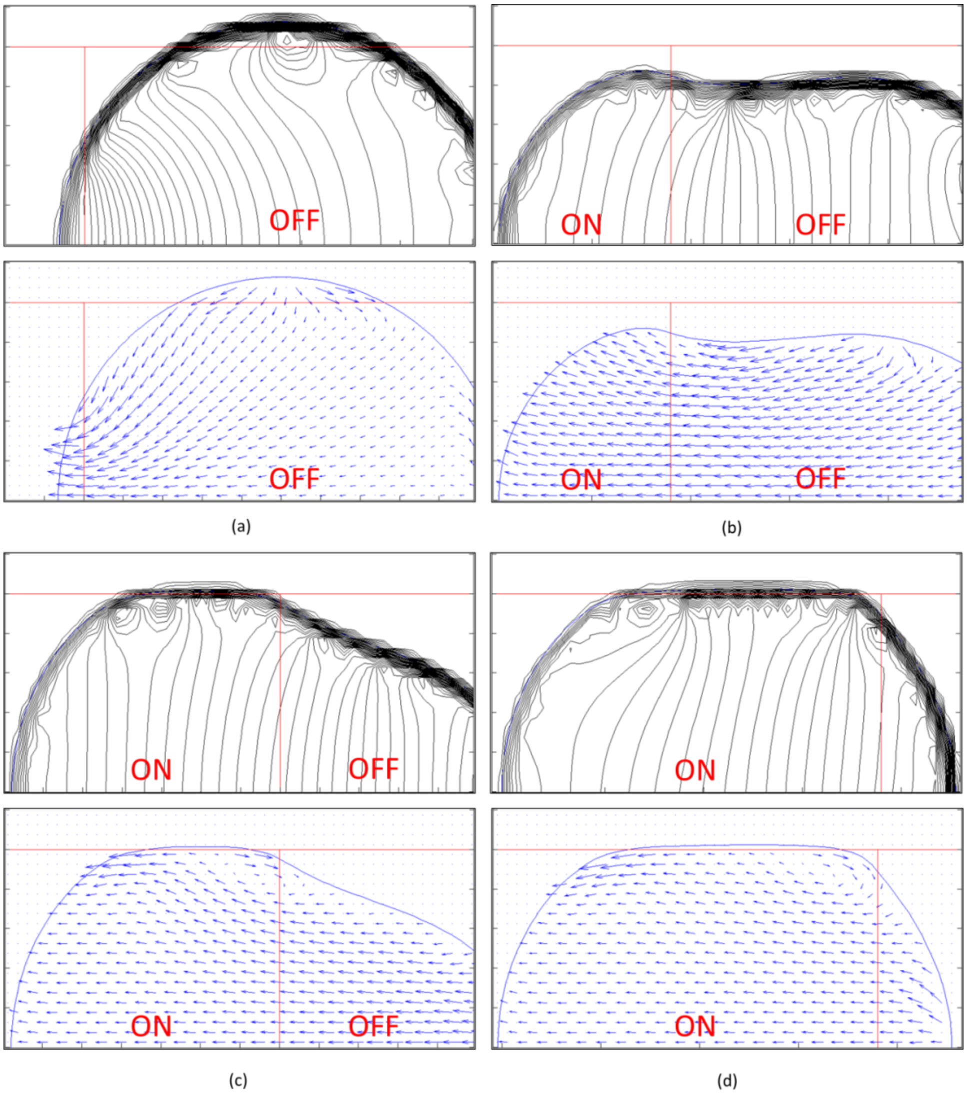

(a) (b)

(c) (d)

Figure 6-9 Pressure (Top) and Velocity Fields (Bottom) for $\theta_{s,ON}$=74° and $\theta_{s,OFF}$=97° at t=0.1ms (a); t=40.0ms (b); t=80.0ms (c); t=120.0ms (d)

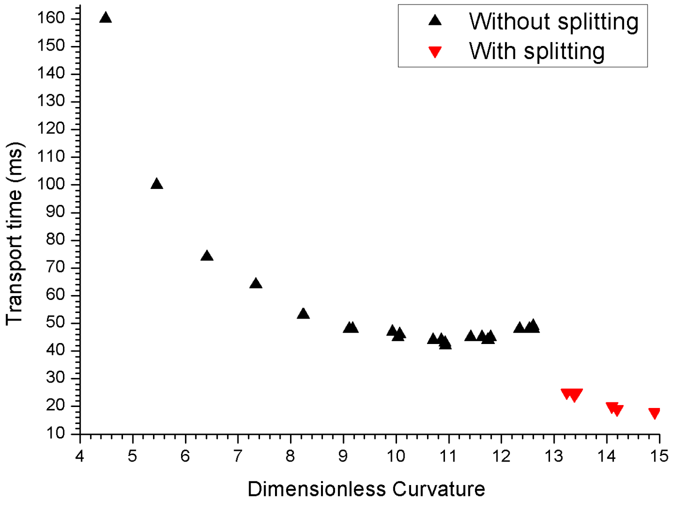

Figure 6-10 Droplet Transport Time versus Dimensionless Curvature for the Parametric Study of Static Contact Angles

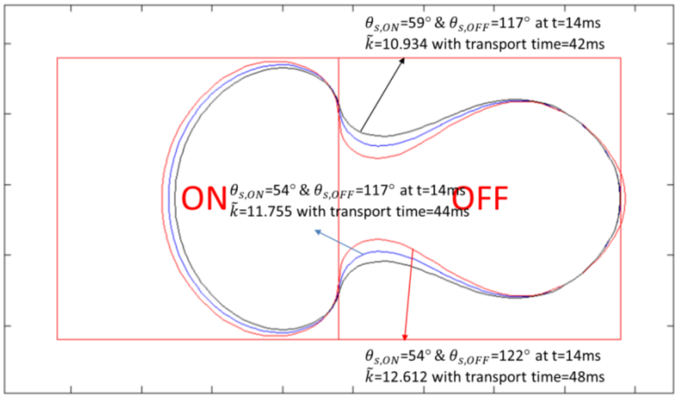

Figure 6-11 Comparison of the Necks for Different Static Contact Angles

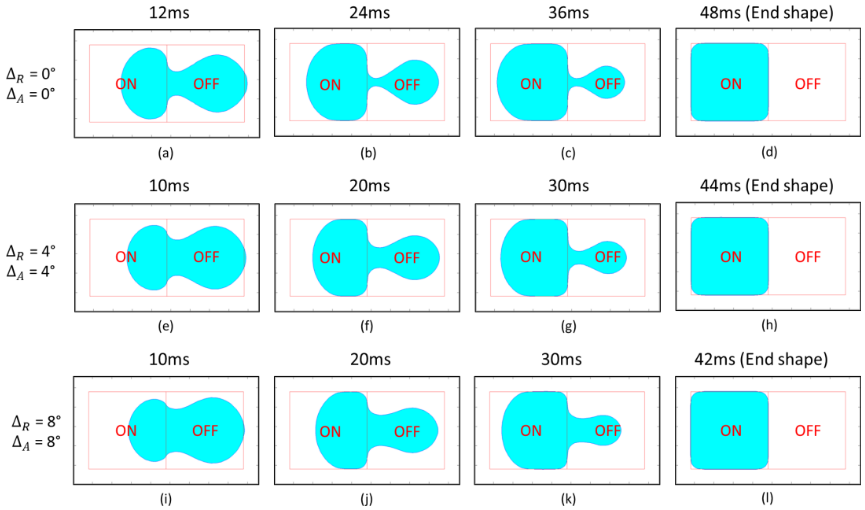

Figure 6-12 Droplet Transport with Different Hysteresis Values: Δ_R=Δ_A=0° (a)-(d); Δ_R=Δ_A=4° (e)-(h); Δ_R=Δ_A=8° (i)-(l)

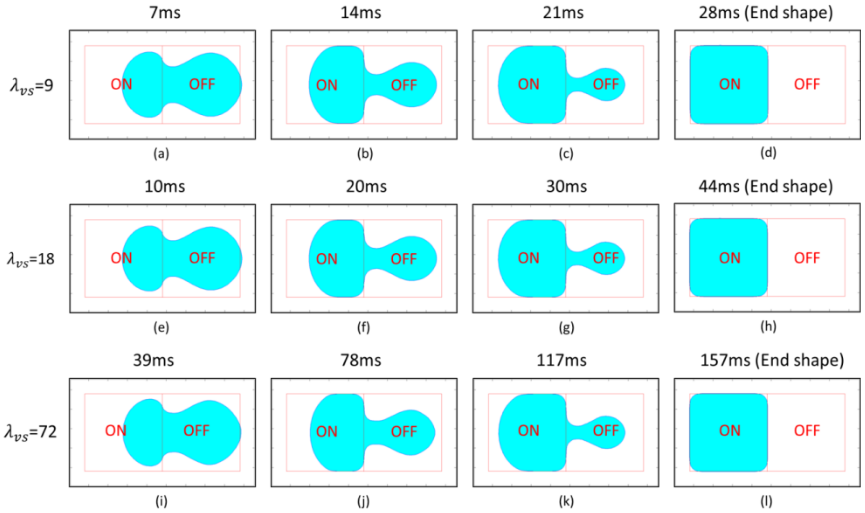

Figure 6-13 Droplet Transport with Different Viscous Stress Coefficients: λ_{vs}=9 (a)-(d); λ_{vs}=18 (e)-(h); λ_{vs}=72 (i)-(l)

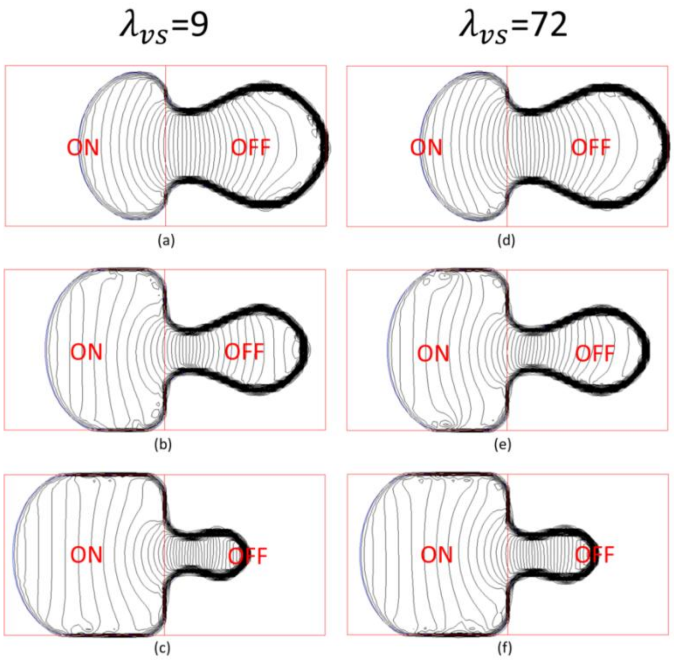

Figure 6-14 Pressure Fields for Different Viscous Stress Coefficients: λ_{vs}=9 at t=7ms (a); t=14ms (b); t=21ms (c); λ_{vs}=72 at t=39ms (d); t=78ms (e); t=117ms (f)

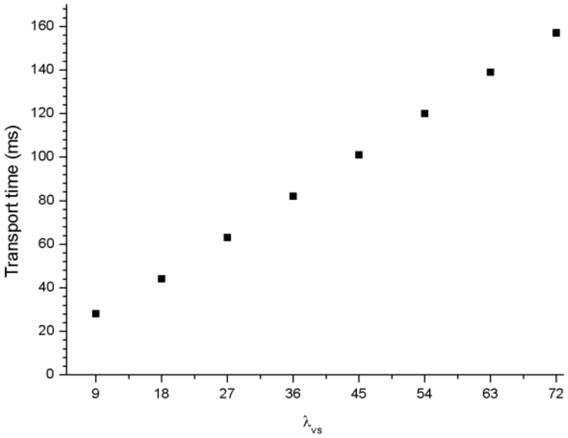

Figure 6-15 Droplet Transport Time versus Viscous Stress Coefficient λ_{vs}

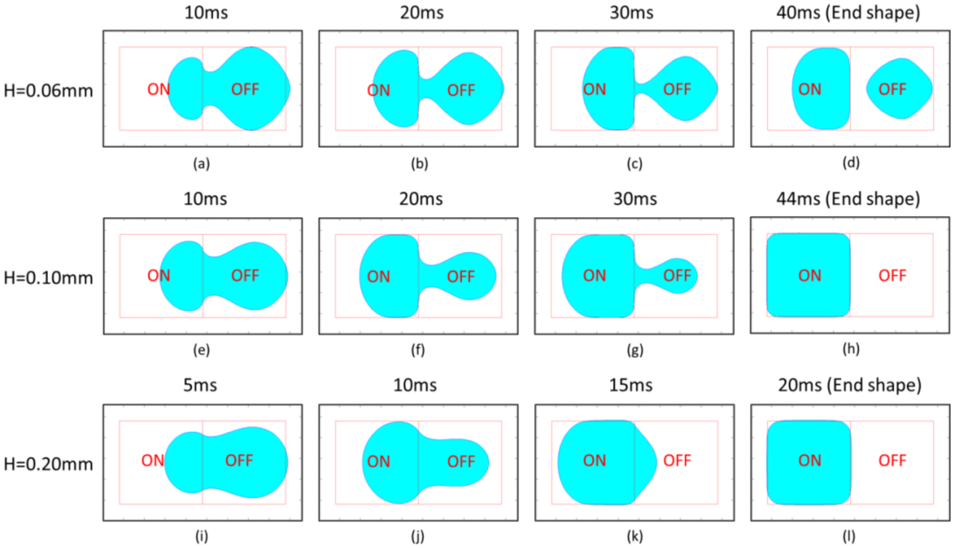

Figure 6-16 Droplet Transport with Different Channel Heights: H=0.06mm (a)-(d); H=0.10mm (e)-(h); H=0.20mm (i)-(l)

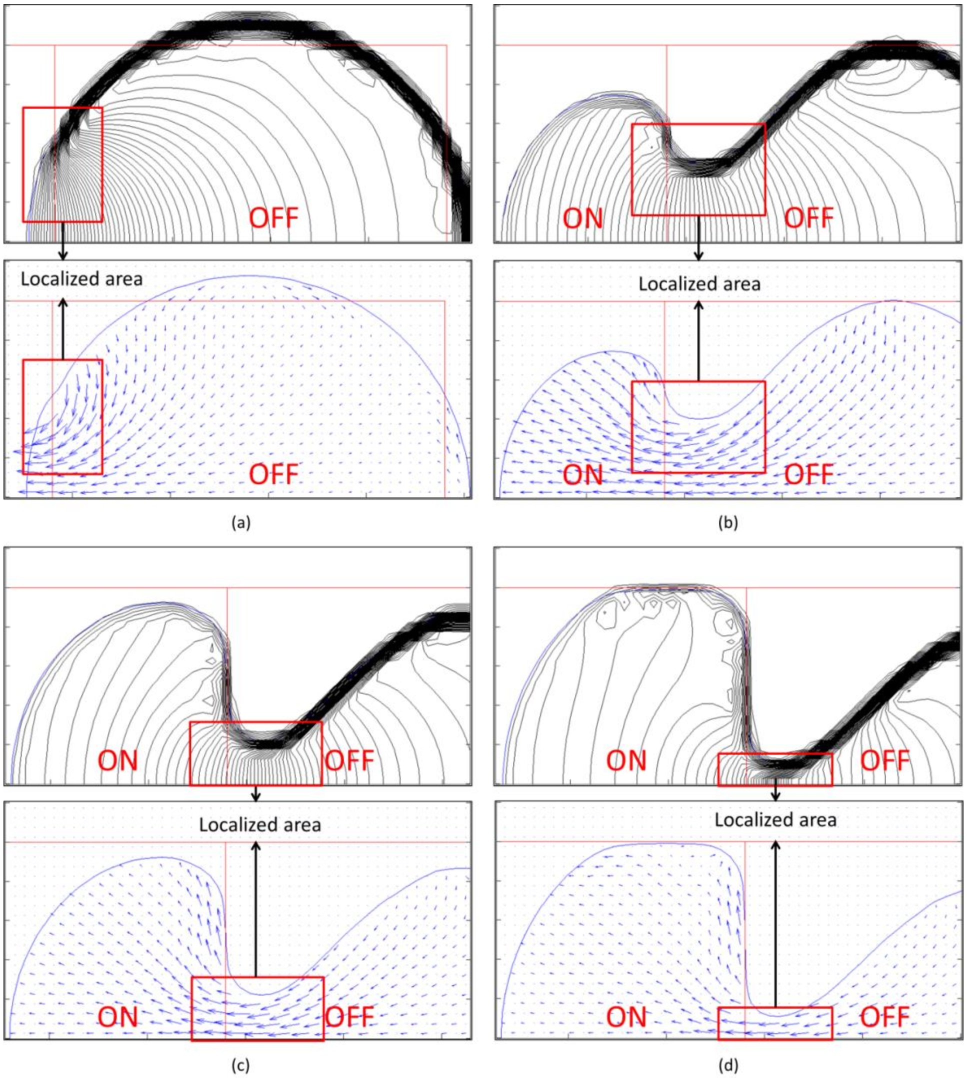

Figure 6-17 Pressure (Top) and Velocity Fields (Bottom) for H=0.06mm at t=0.1ms (a); t=10.0ms (b); t=20.0ms (c); t=30.0ms (d)

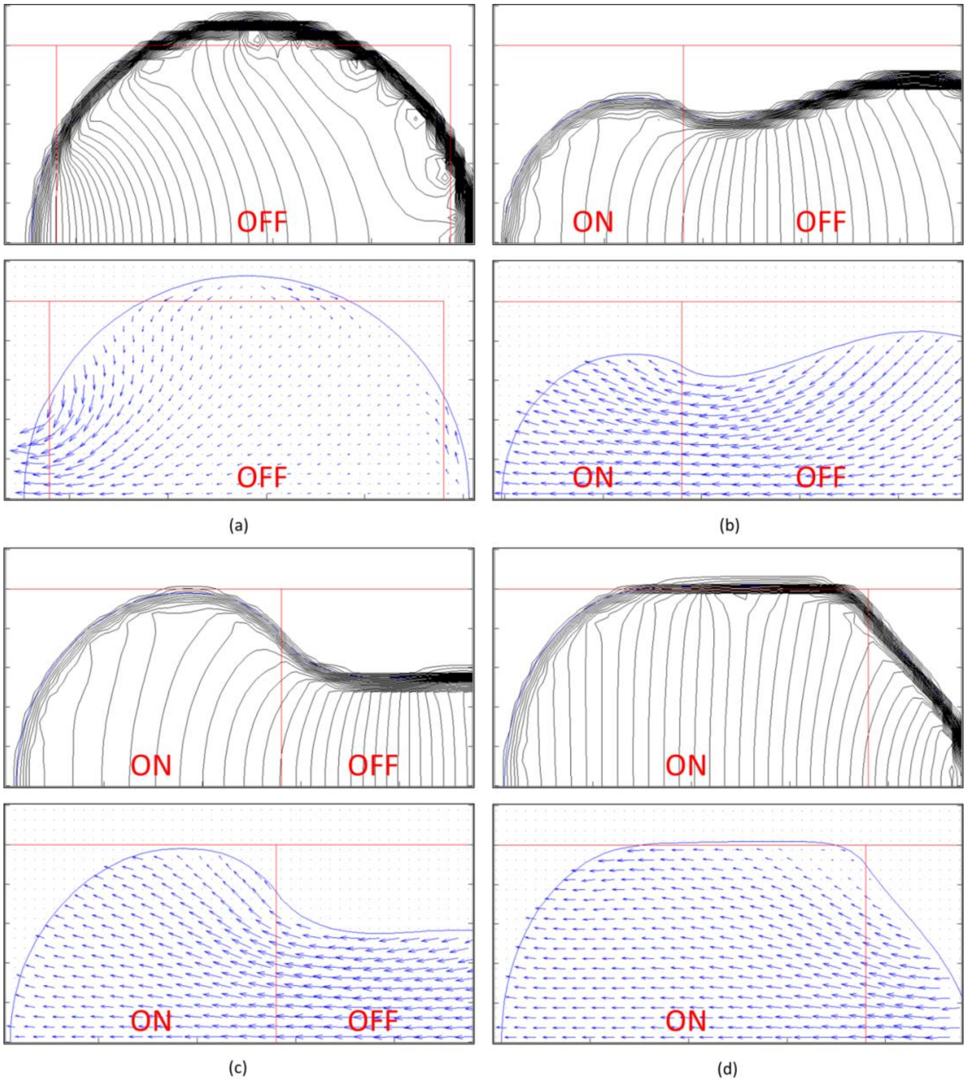

Figure 6-18 Pressure (Top) and Velocity Fields (Bottom) for H=0.20mm at t=0.1ms (a); t=5.0ms (b); t=10.0ms (c); t=15.0ms (d)

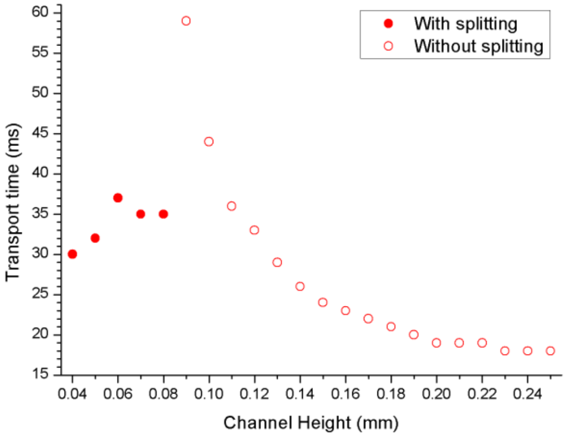

Figure 6-19 Droplet Transport Time versus Channel Height for 2×2mm^2 Electrode Size

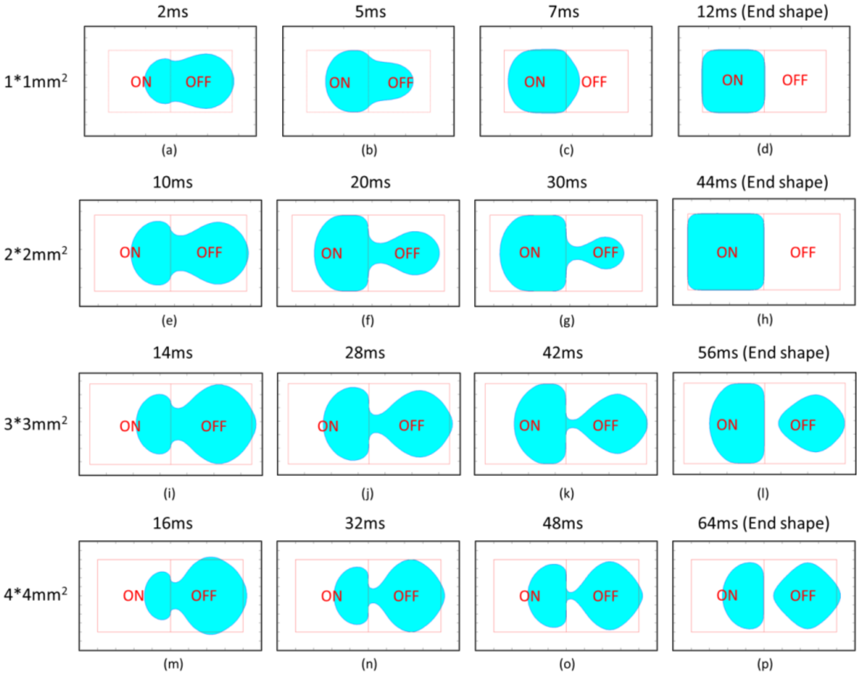

Figure 6-20 Droplet Transport with Different Electrode Sizes: 1×1mm^2 (a)-(d); 2×2mm^2 (e)-(h); 3×3mm^2 (i)-(l); 4×4mm^2 (m)-(p)

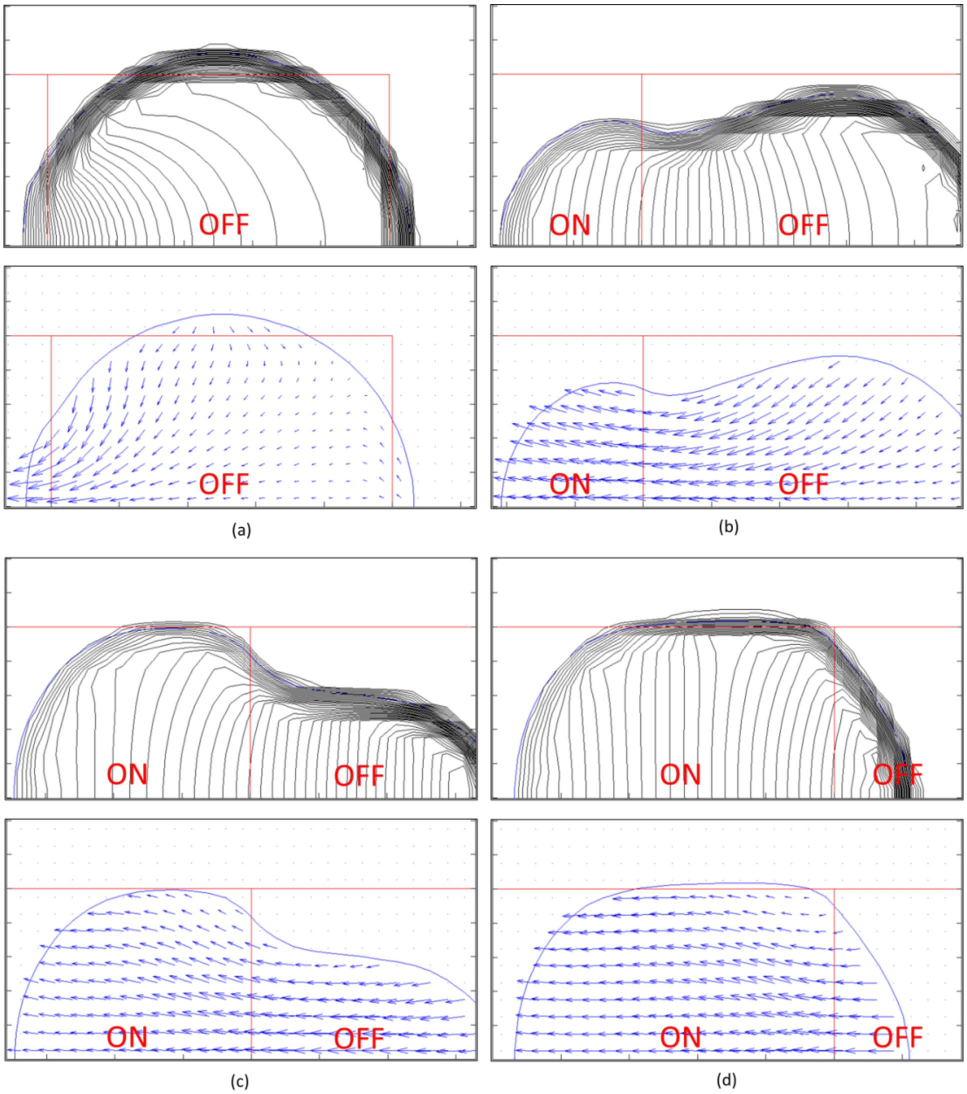

(a) (b)

(c) (d)

Figure 6-21 Pressure (Top) and Velocity Fields (bottom) for 1×1mm^2 Electrode Size at t=0.1ms (a); t=2.0ms (b); t=5.0ms (c); t=7.0ms (d)

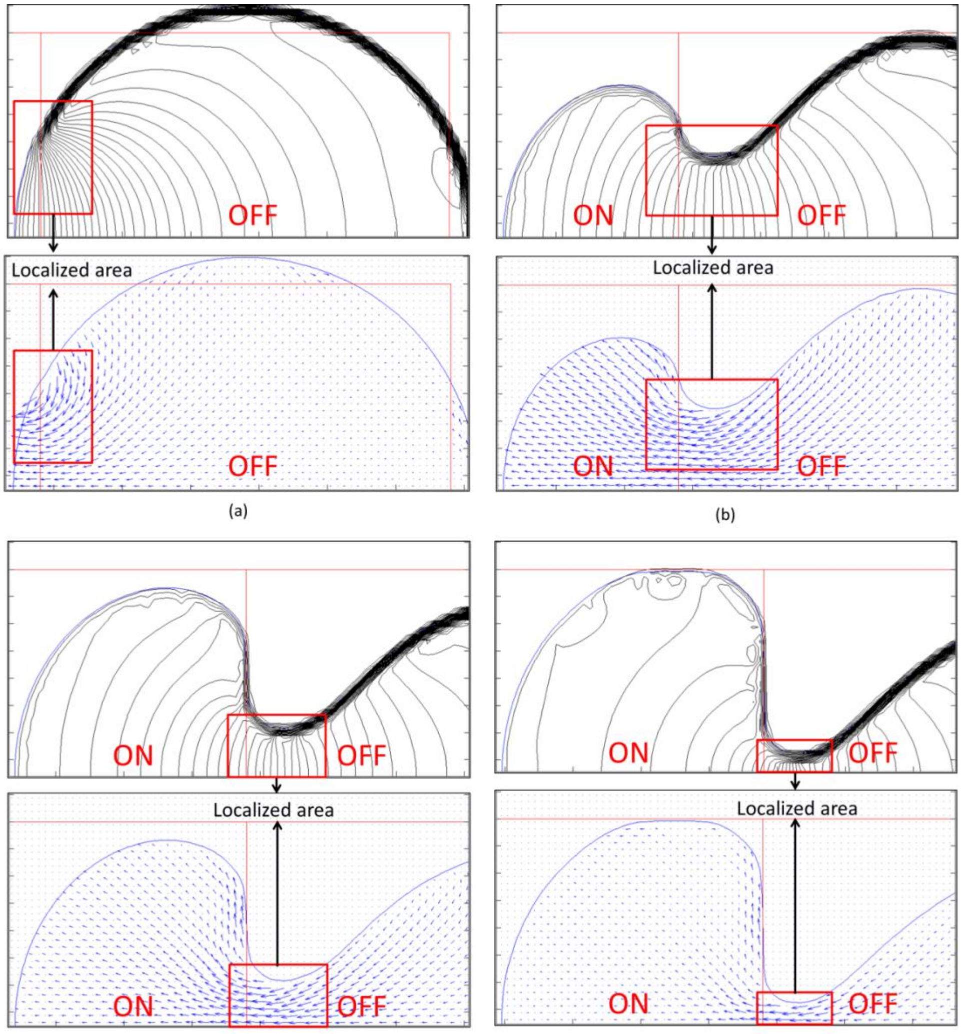

(a) (b) (c) (d)

Figure 6-22 Pressure (Top) and Velocity Fields (Bottom) for 3×3mm^2 Electrode Size at

t=0.1ms (a); t=14.0ms (b); t=28.0ms (c); t=42.0ms (d)

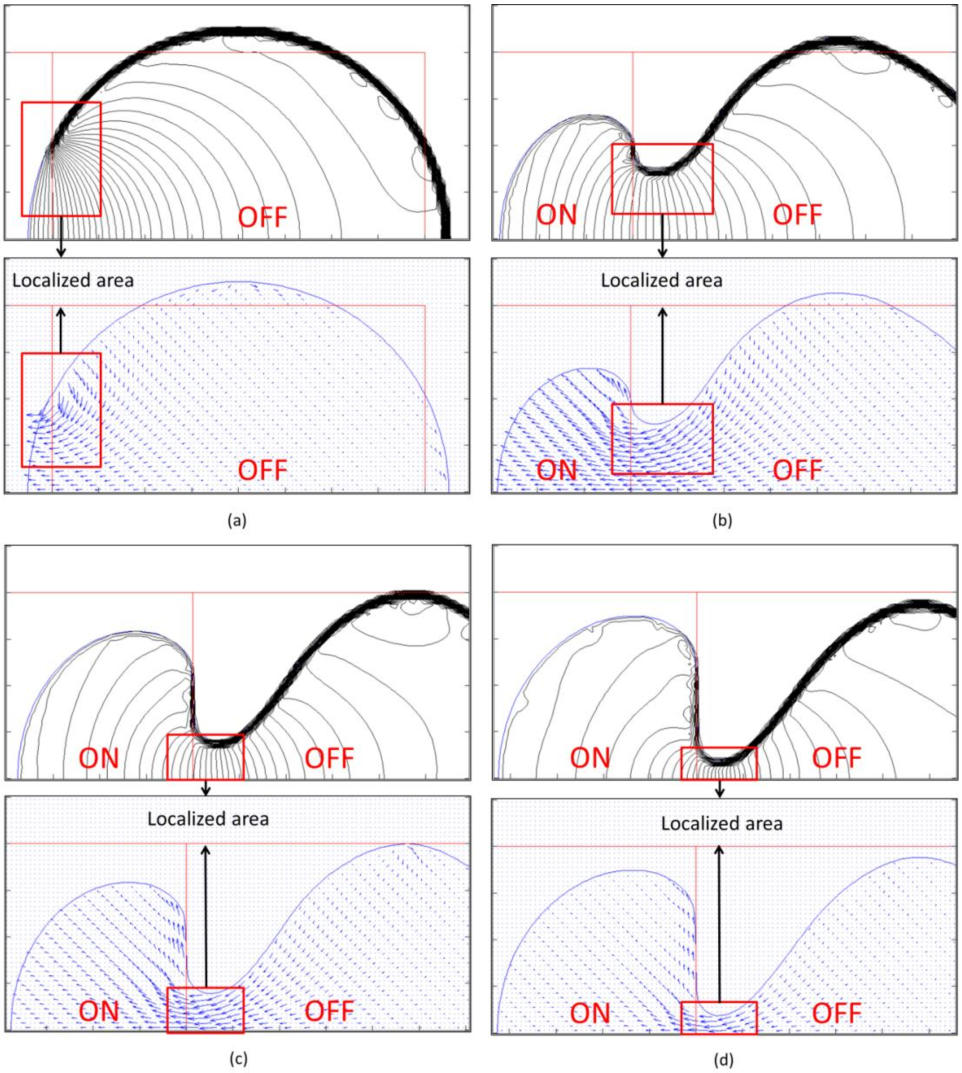

Figure 6-23 Pressure (Top) and Velocity Fields (Bottom) for 4×4mm^2 Electrode Size at

t=0.1ms (a); t=16.0ms (b); t=32.0ms (c); t=48.0ms (d)

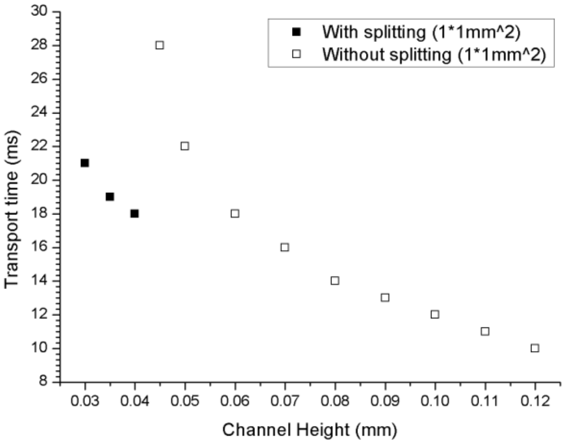

Figure 6-24 Droplet Transport Time versus Channel Height for 1×1mm^2 Electrode Size

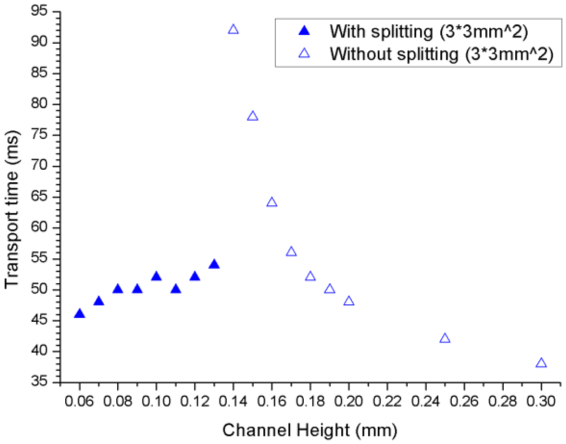

Figure 6-25 Droplet Transport Time versus Channel Height for 3×3mm^2 Electrode Size

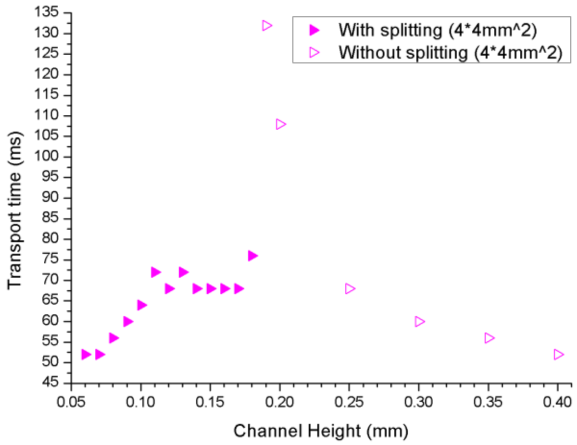

Figure 6-26 Droplet Transport Time versus Channel Height for 4×4mm^2 Electrode Size

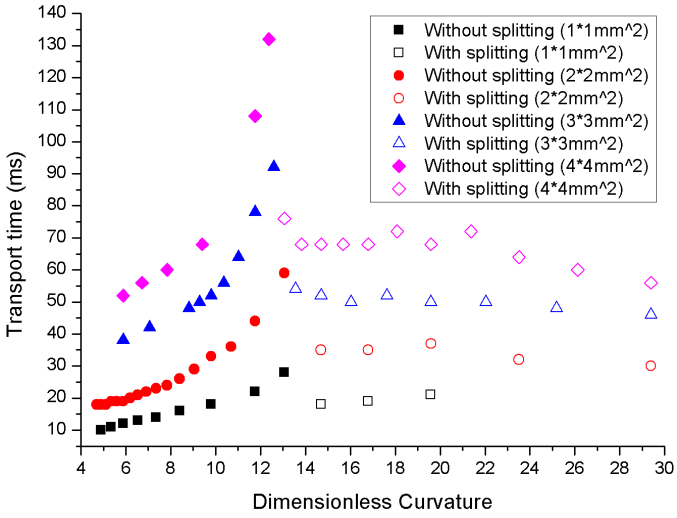

Figure 6-27 Droplet Transport Time versus Dimensionless Curvature for the Parametric Study of Channel Height and Electrode Size

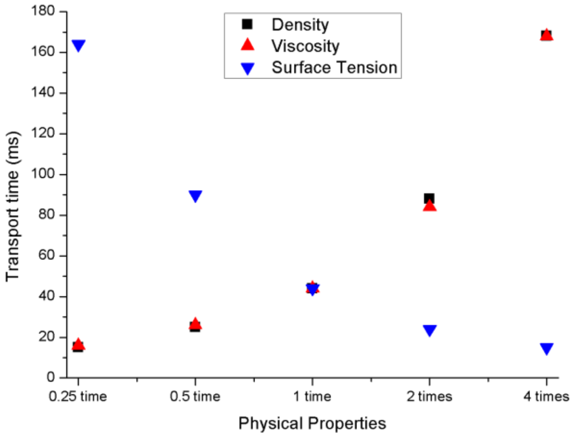

Figure 6-28 Droplet Transport Time versus Droplet Physical Properties

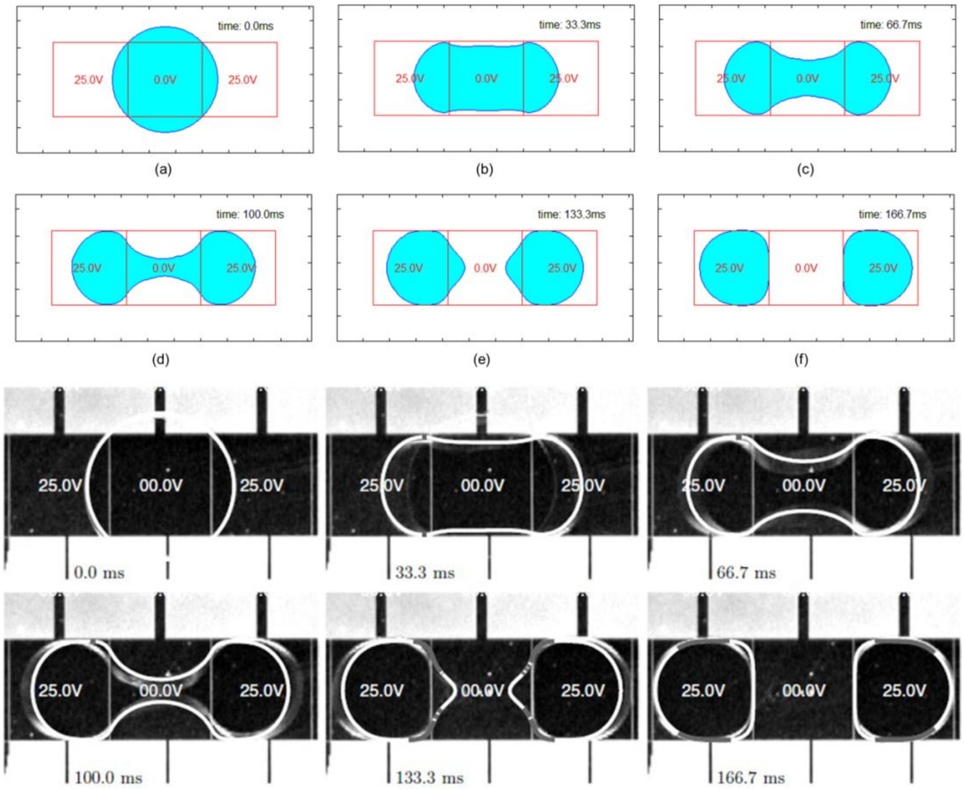

Figure 6-29 Droplet Splitting: Numerical (Top: Present Study); Experimental (Bottom): [20]

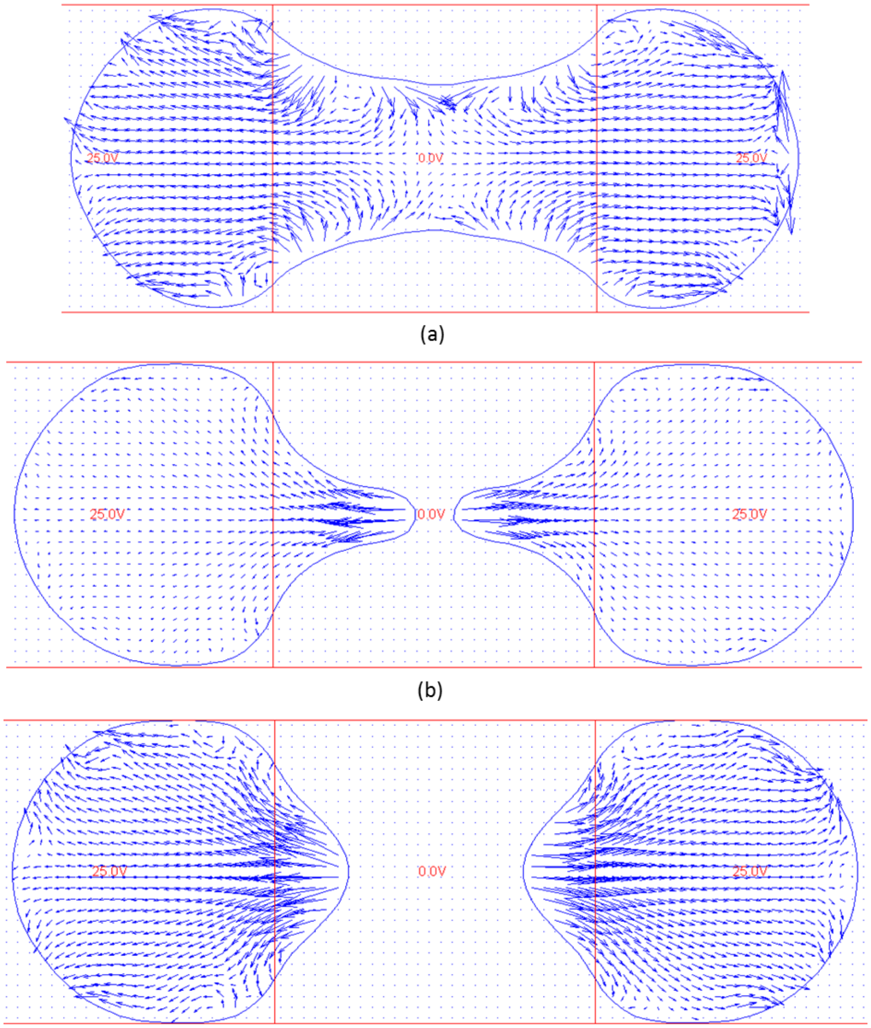

(a)

(b)

(c)

Figure 6-30 Flow Fields of Droplet Splitting at Selected Instants: 66.7ms (a); 128.7ms (b); 133.3ms (c)

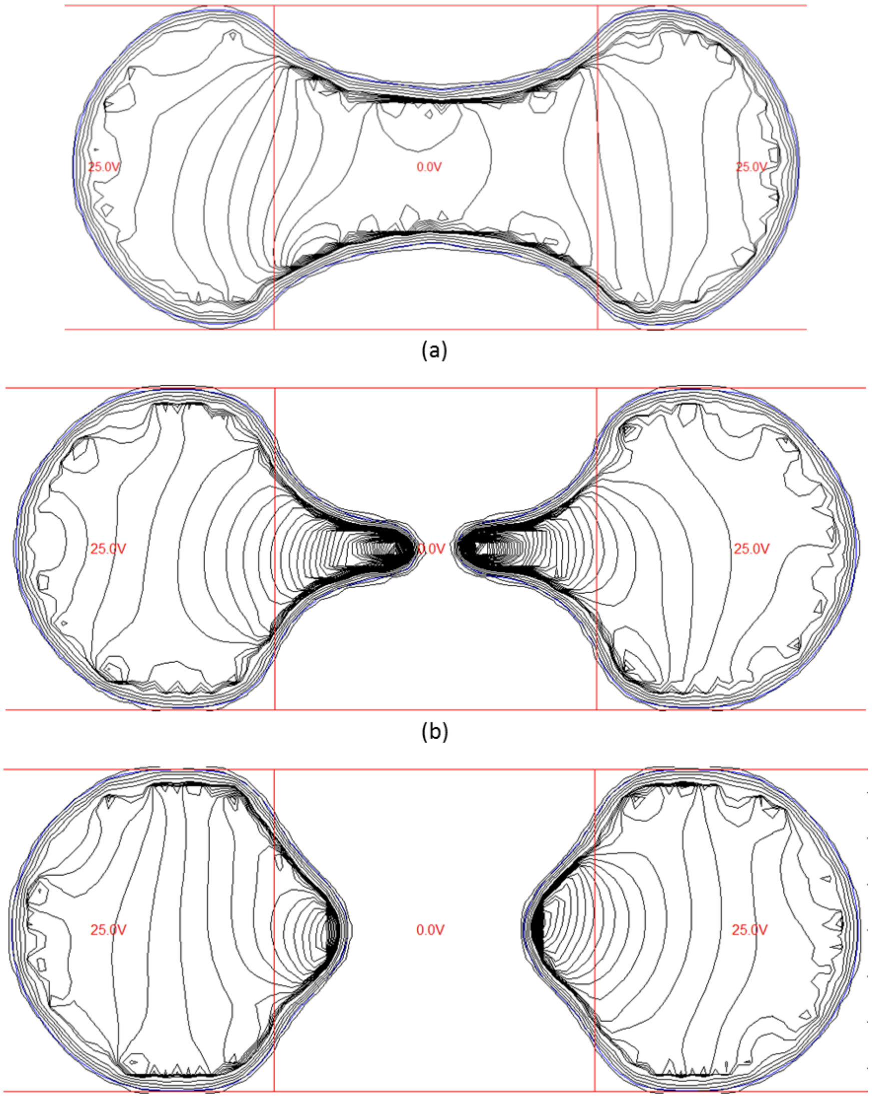

(a)

(b)

(c)

Figure 6-31 Pressure Fields of Droplet Splitting at Selected Instants: 66.7ms (a); 128.7ms (b); 133.3ms (c)

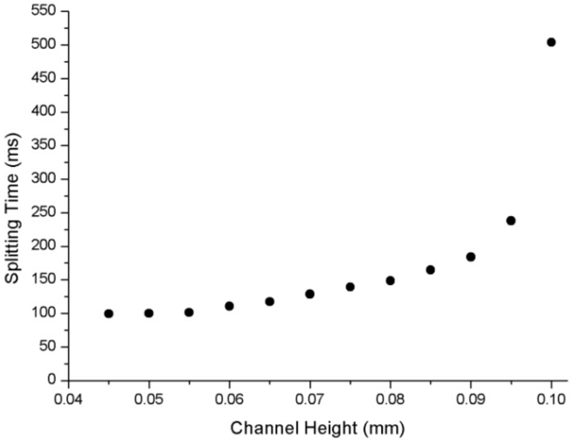

Figure 6-32 Droplet Splitting Time versus Channel Height

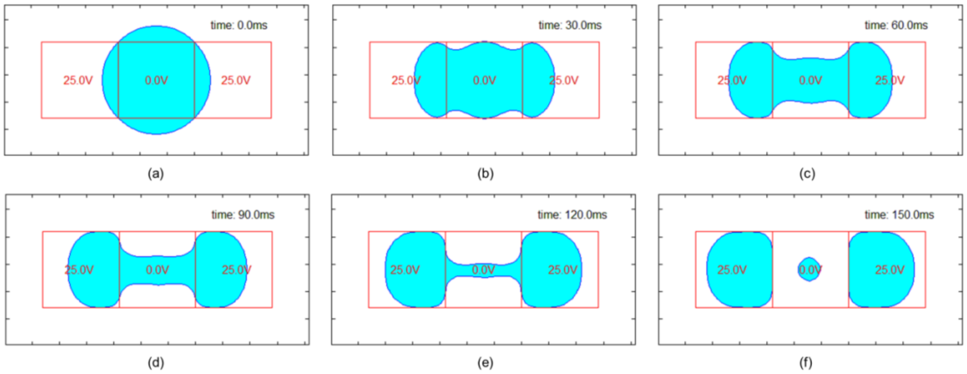

Figure 6-33 Droplet Splitting with Formation of a Satellite Droplet at H=0.035mm

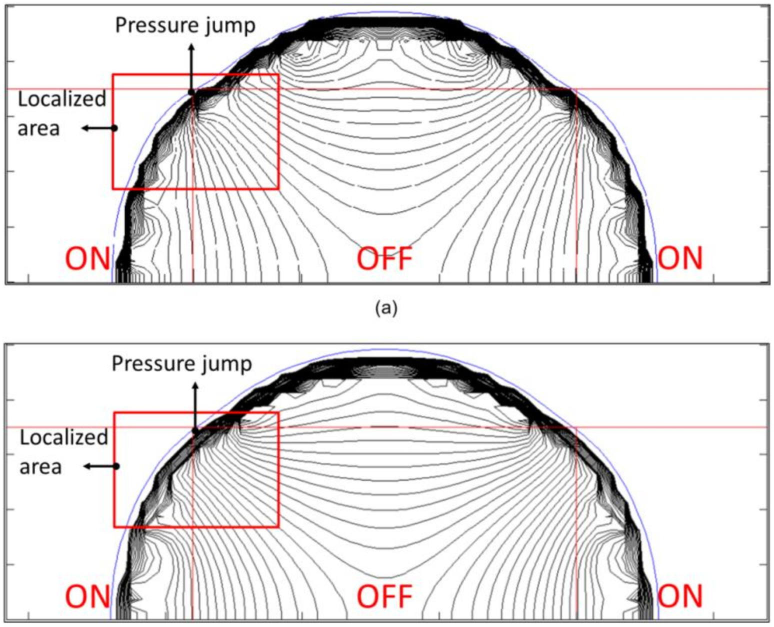

(a)

(b)

Figure 6-34 Pressure Fields of Droplet Splitting at t=1ms: H=0.035ms (a); H=0.07ms (b)

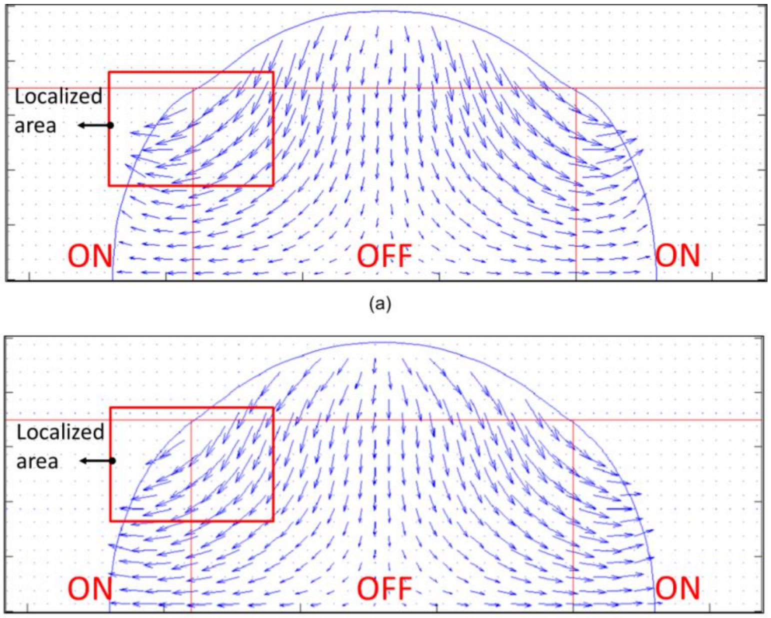

(a)

(b)

Figure 6-35 Velocity Fields of Droplet Splitting at t=1ms: H=0.035ms (a); H=0.07ms (b)

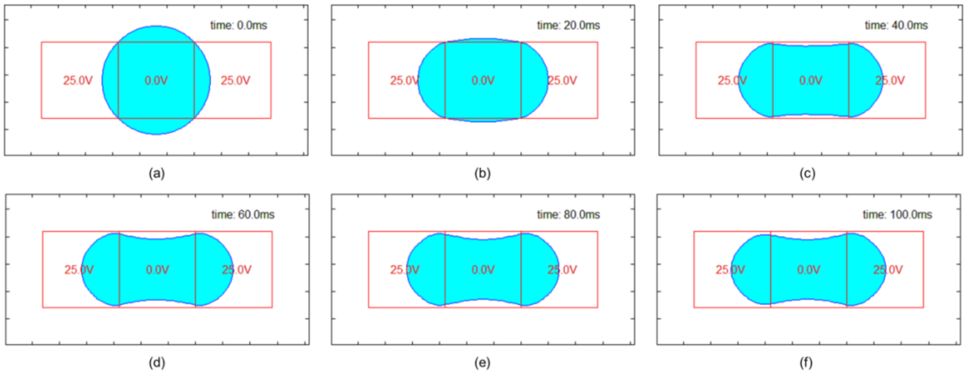

Figure 6-36 Droplet Splitting with H=0.15mm

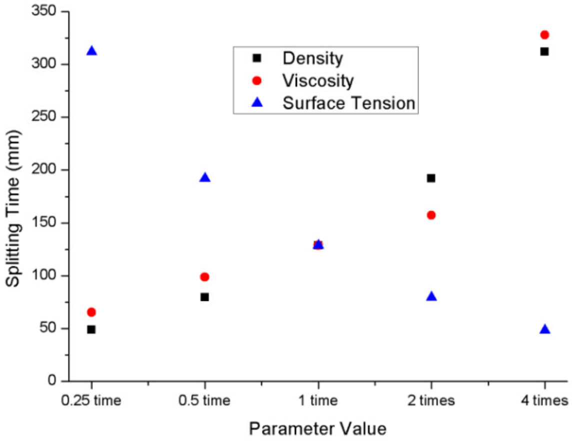

Figure 6-37 Parametric Study of Droplet Splitting Process

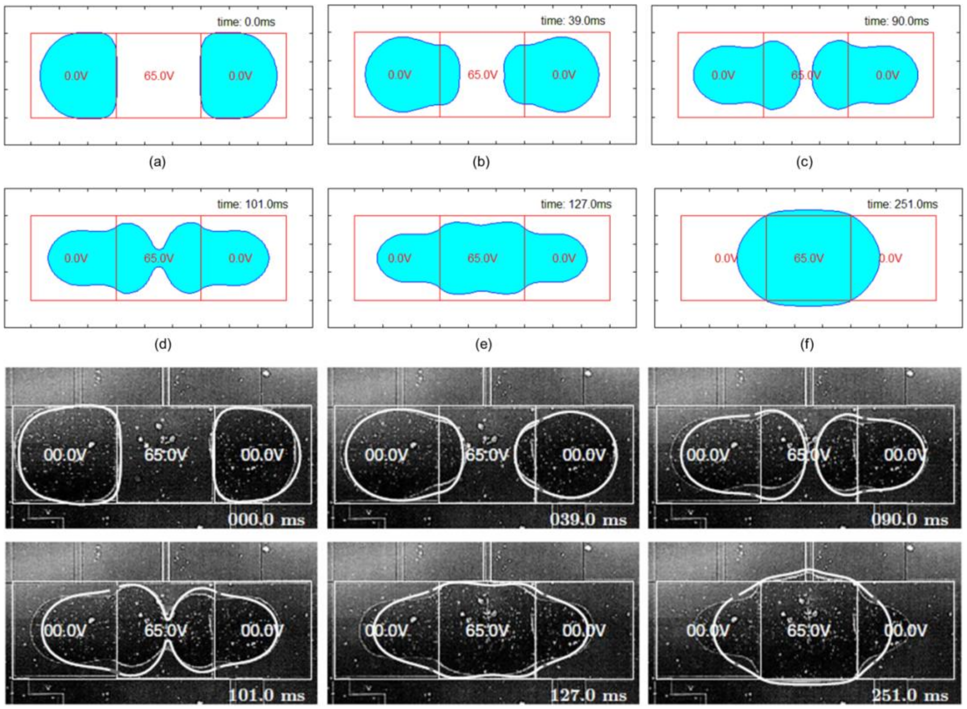

Figure 6-38 Droplet Merging: Numerical (Top: Present Study); Experimental (Bottom): [20]

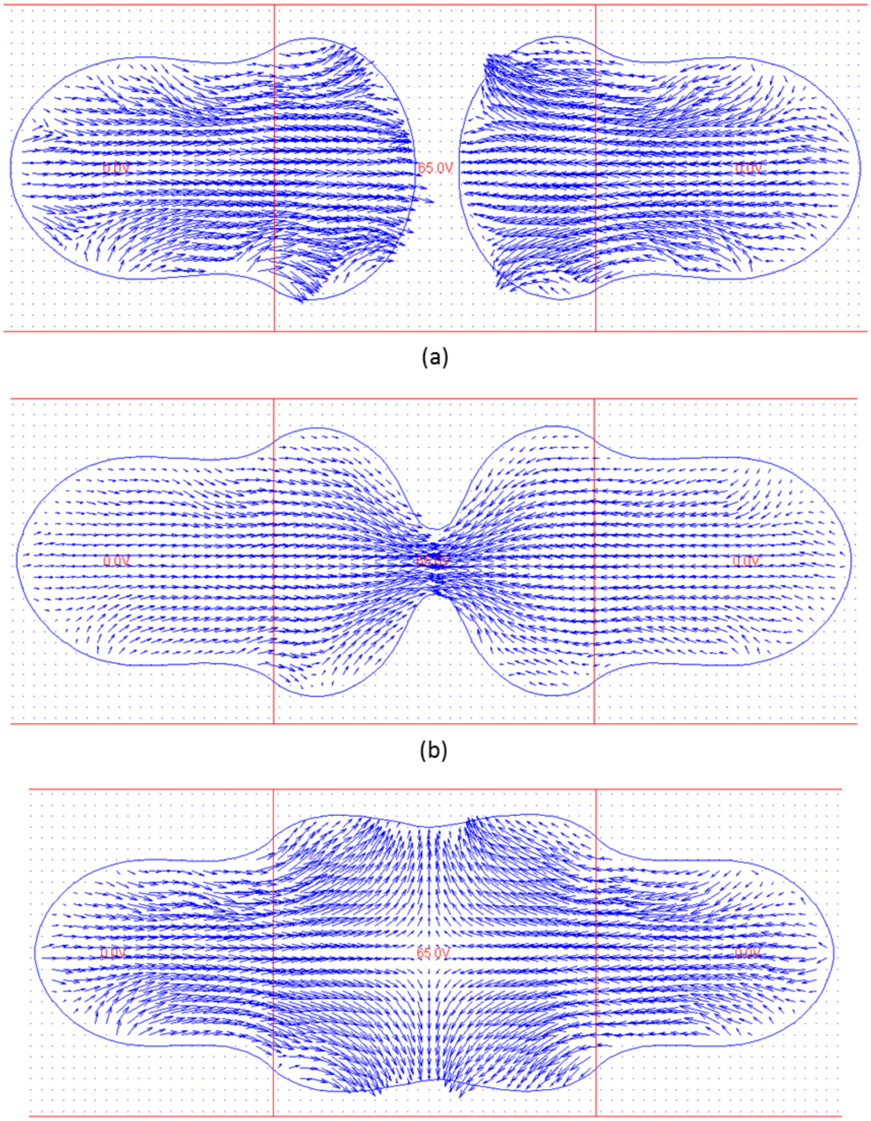

(a)

(b)

(c)

Figure 6-39 Flow Fields of Droplet Merging at Selected Instants: 90.0ms (a); 101.0ms (b); 127.0ms (c)

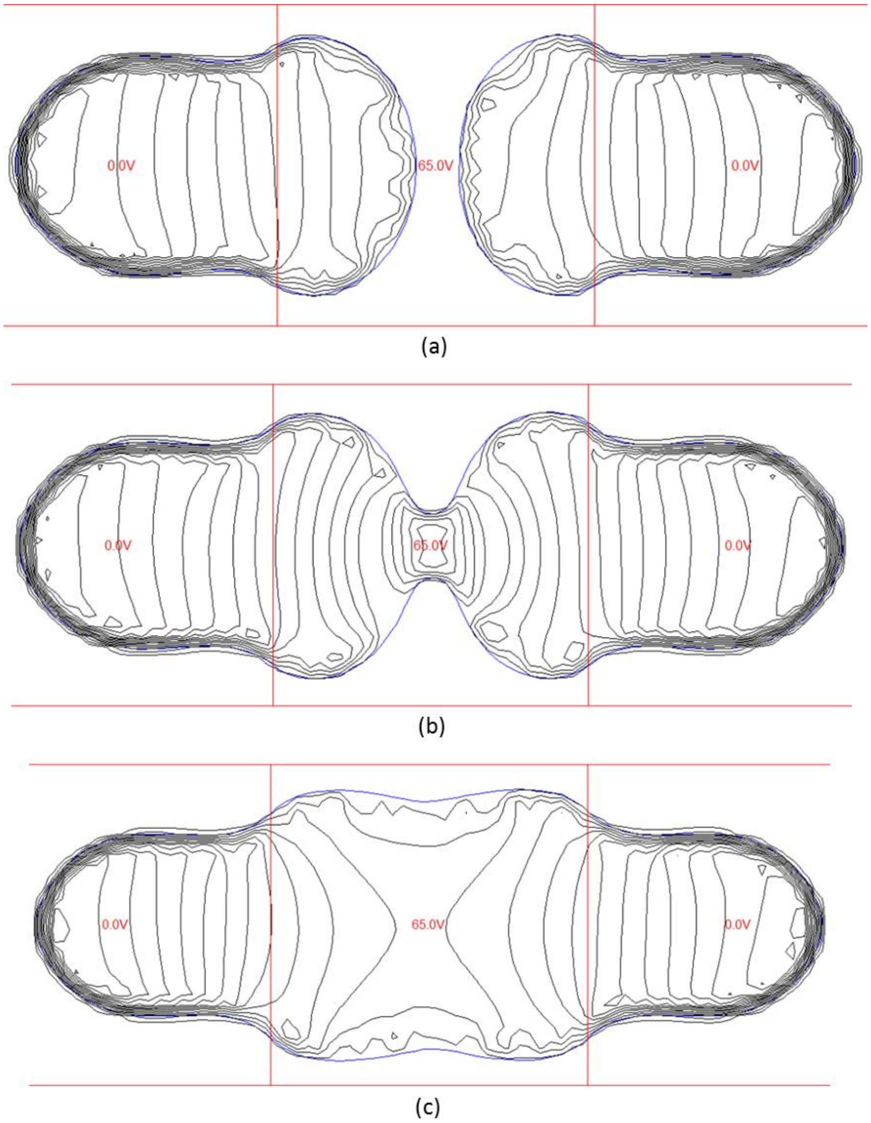

Figure 6-40 Pressure Fields of Droplet Merging at Selected Instants: 90.0ms (a); 101.0ms (b); 127.0ms (c)

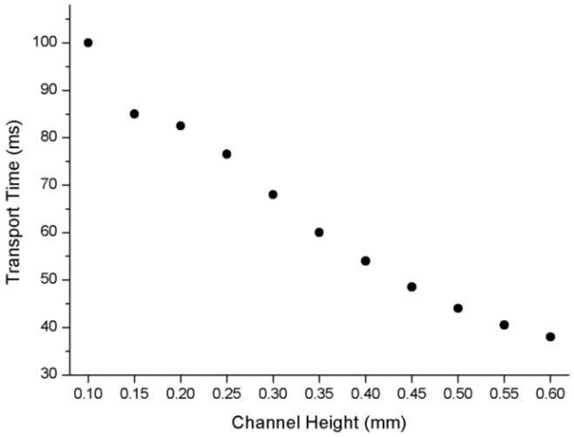

Figure 6-41 Droplet Transport Time before Merging versus Channel Height

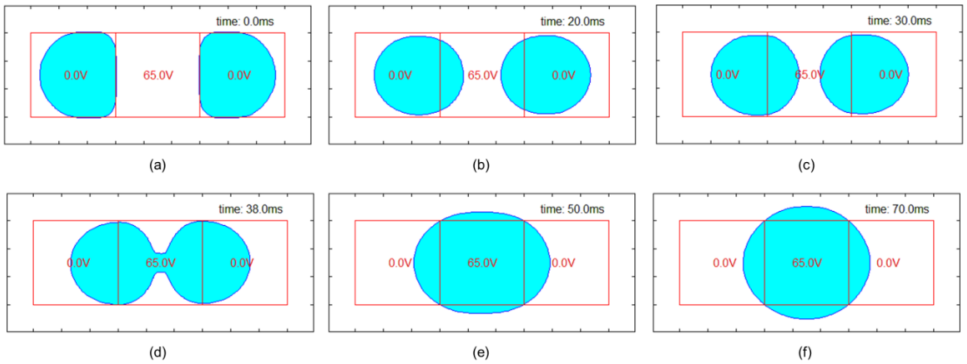

(a) (b) (c)

(d) (e) (f)

Figure 6-42 Droplet Merging with 0.60mm Channel Height

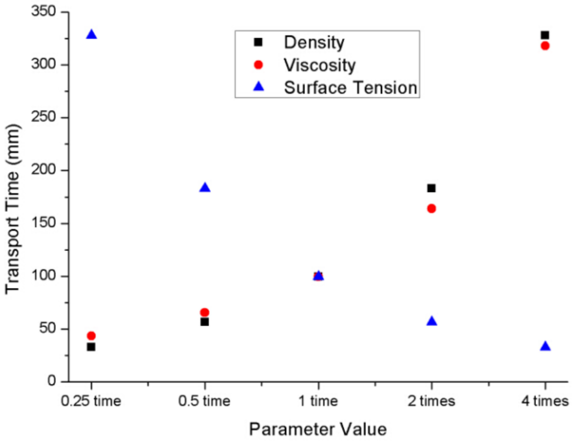

Figure 6-43 Parametric Study of Droplet Merging Process

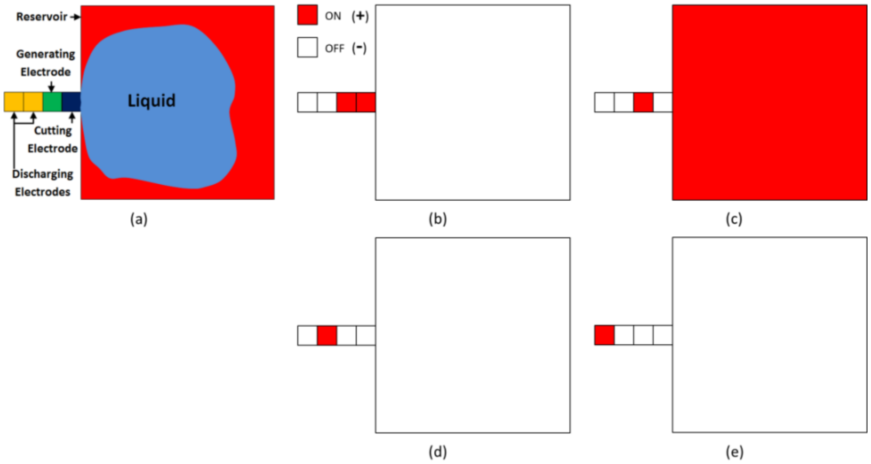

Figure 6-44 'Conventional Reservoir' Design: the Schematic (a); Four Stages of the Dispensing Process: Filling Stage (b); Cutting Stage (c); Discharging Stage (d)-(e)

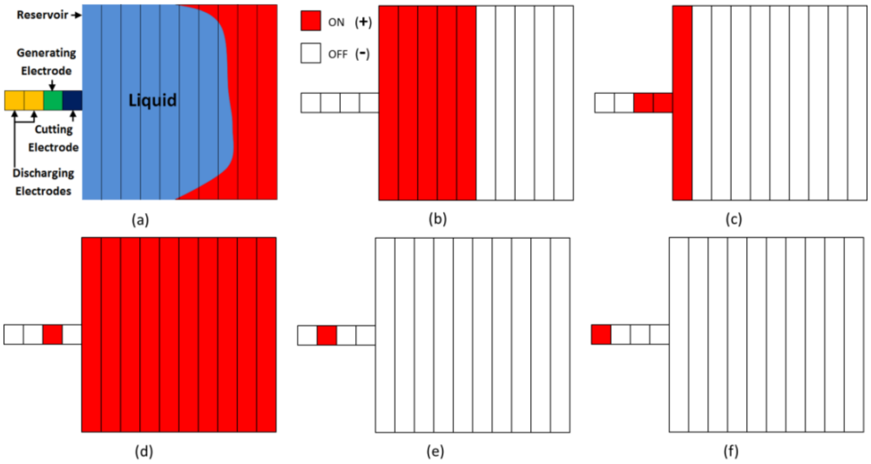

Figure 6-45 'Stripped Reservoir' Design: the Schematic (a); Five Stages of the Dispensing process: Filling Stage (b)-(c); Cutting Stage (d); Discharging Stage (e)-(f)

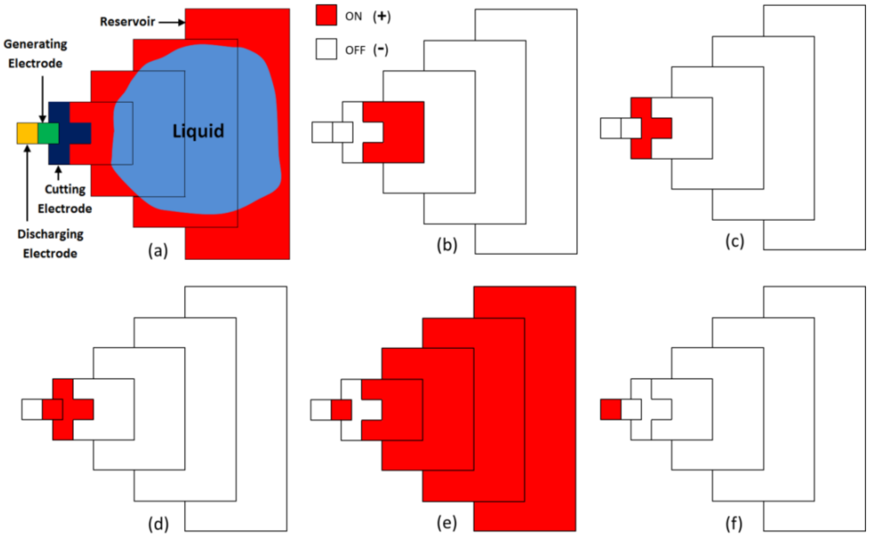

Figure 6-46 ‘TCC reservoir’ design: the Schematic (a); Five Stages of the Dispensing Process: Filling Stage (b)-(d); Cutting Stage (e); Discharging Stage (f)

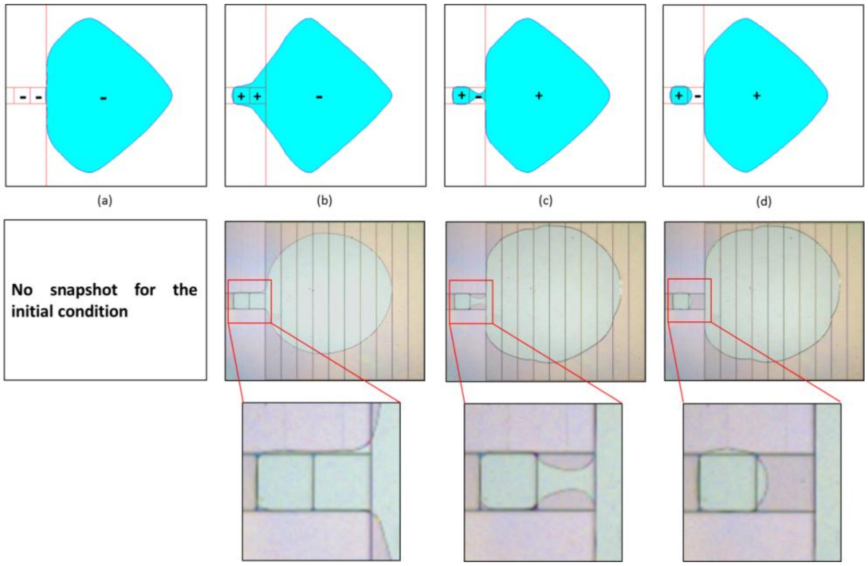

Figure 6-47 Dispensing Process for the 'Conventional Reservoir' Design: Numerical (Top: Present Study): Filling Stage (a)-(b); Cutting Stage (c)-(d); Experimental (Bottom)

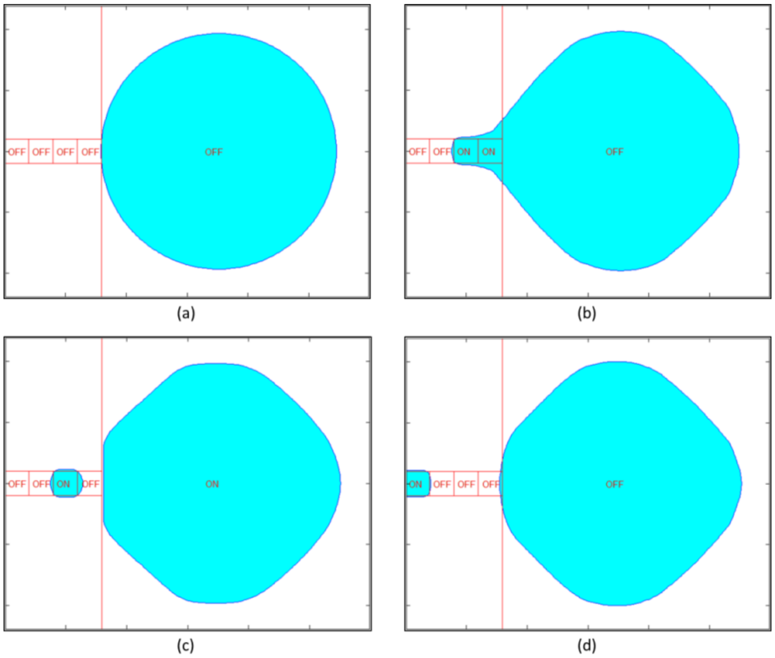

Figure 6-48 The Dispensing Process of the 1st Droplet: Initial Condition (a); End of the Filling Stage (b); End of the Cutting Stage (c); End of the Discharging Stage (d)

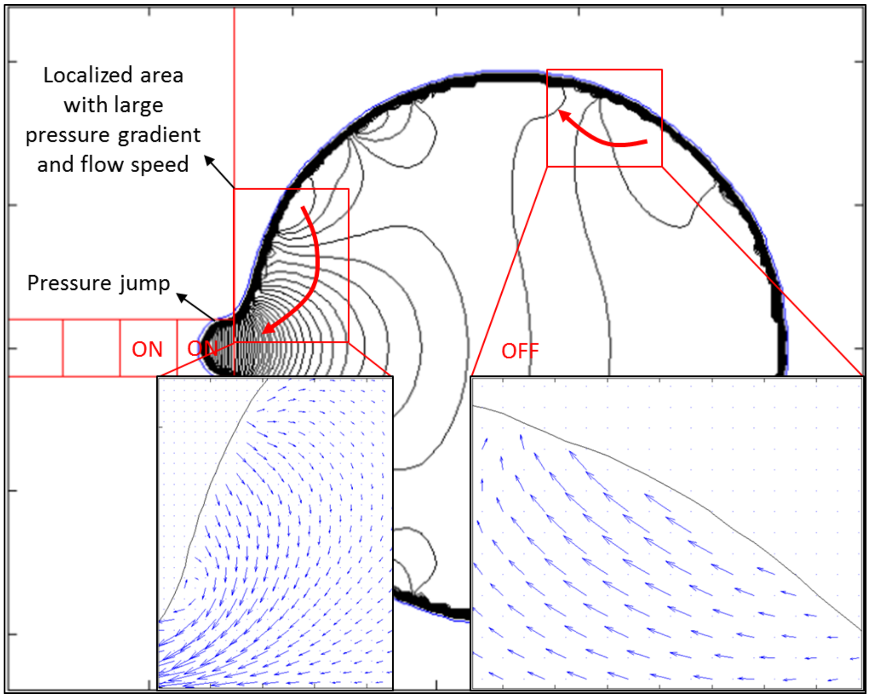

Figure 6-49 Pressure and Velocity Fields at the Beginning of the Filling Stage of the 1st Droplet in the ‘Conventional Reservoir’ Design

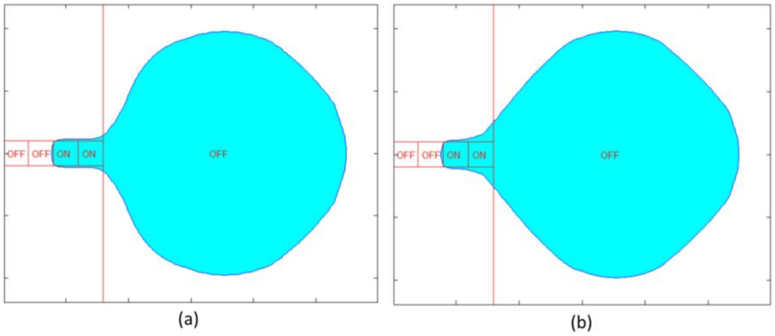

(a)

(b)

Figure 6-50 Liquid Contours of the 1st Droplet in the ‘Conventional Reservoir’ Design: t=525ms (a); t=1350ms (b)

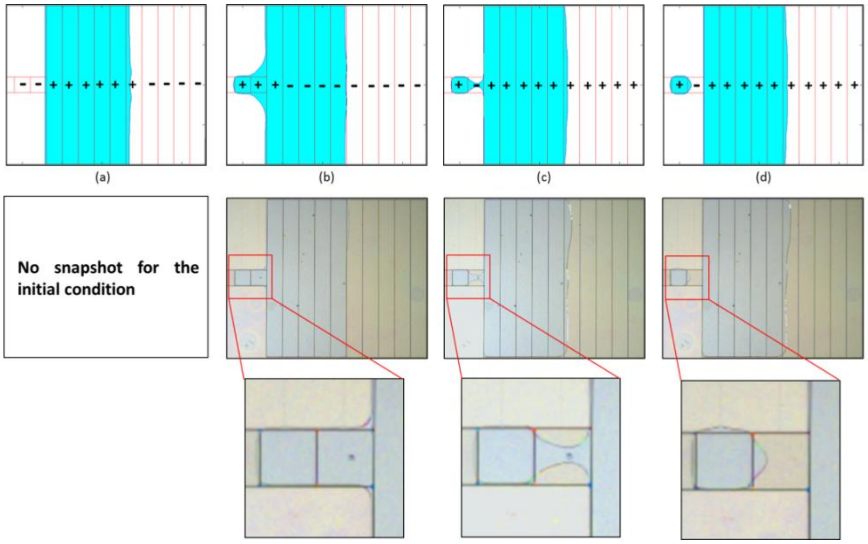

Figure 6-51 Dispensing Process for the 'Stripped Reservoir' Design: Numerical (Top: Present Study): Filling Stage (a)-(b); Cutting Stage (c)-(d); Experimental (Bottom)

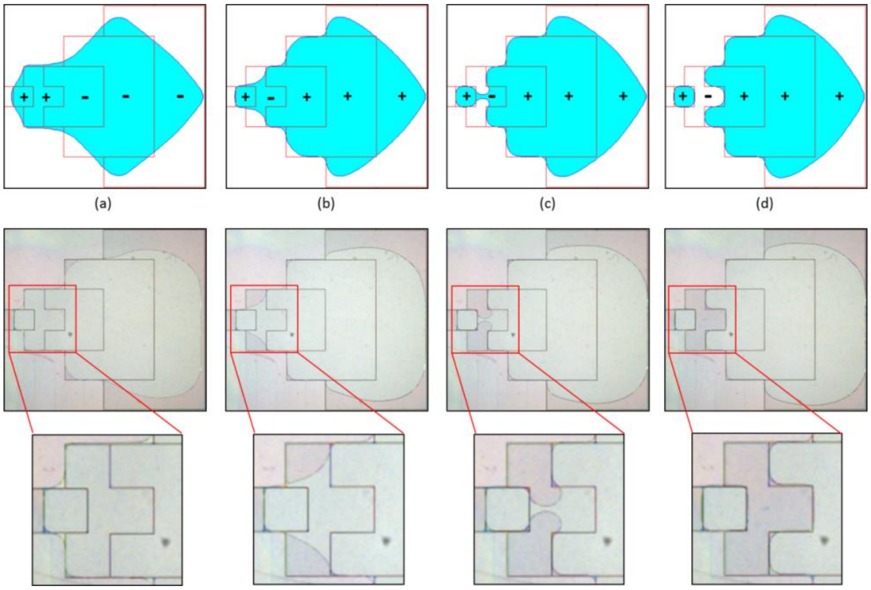

Figure 6-52 Dispensing Process for the 'TCC Reservoir' Design: Numerical (Top: Present Study): Filling Stage (a); Cutting Stage (b)-(d); Experimental (Bottom)

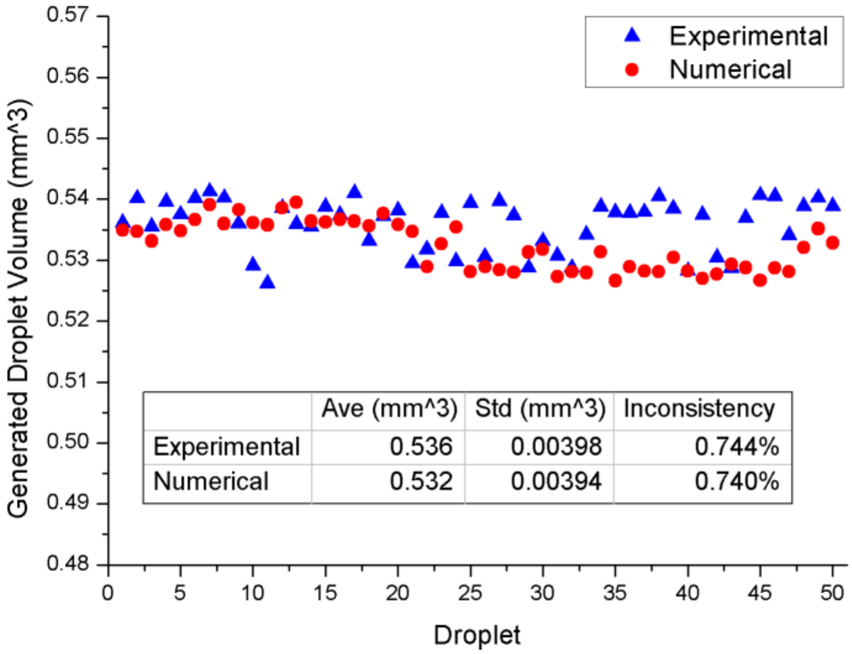

	Ave (mm^3)	Std (mm^3)	Inconsistency
Experimental	0.536	0.00398	0.744%
Numerical	0.532	0.00394	0.740%

Figure 6-53 Volume of Droplets Generated from the 'Conventional Reservoir' Design

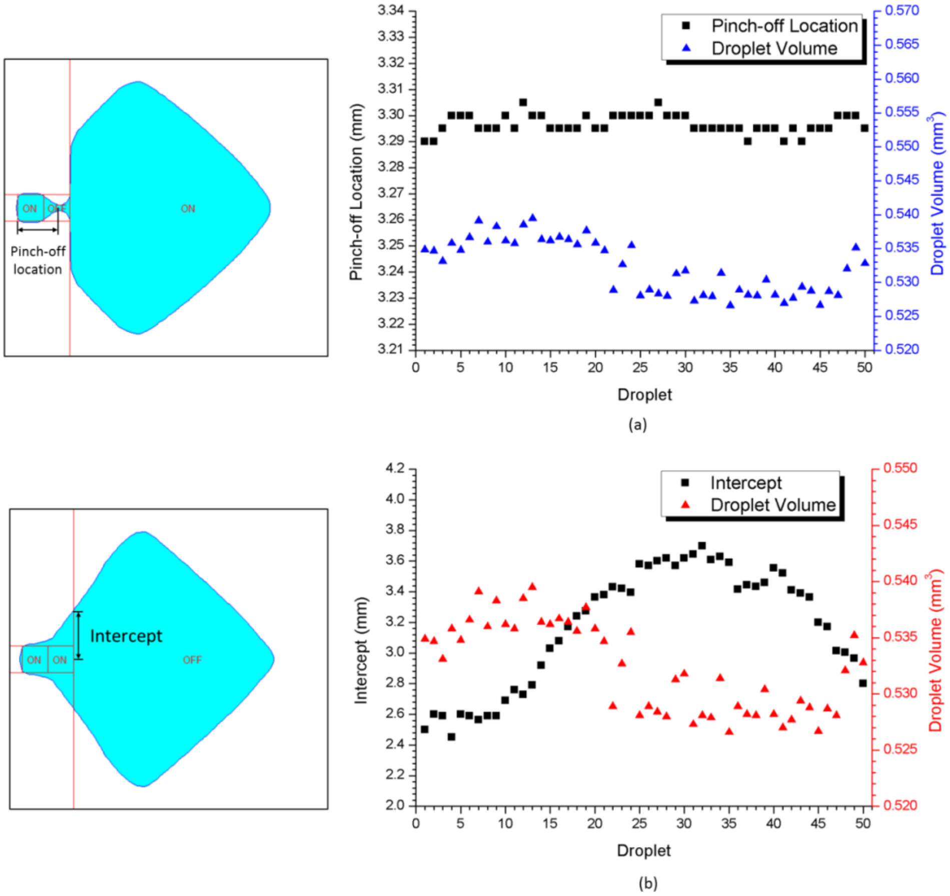

Figure 6-54 Pinch-off Locations (a) and Intercepts (b) versus Droplet Volumes for the 'Conventional Reservoir' Design

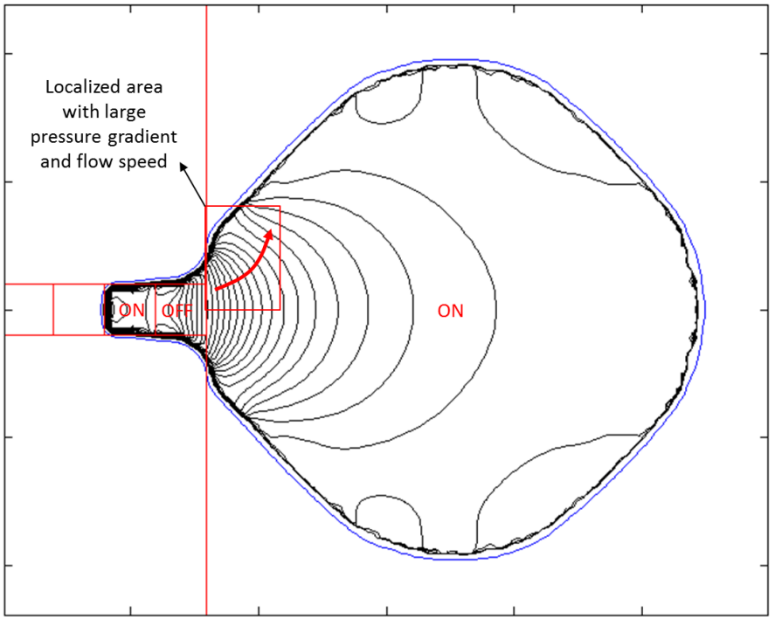

Figure 6-55 Pressure Field at the Beginning of Cutting Stage of the First Droplet in the ‘Conventional Reservoir’ Design

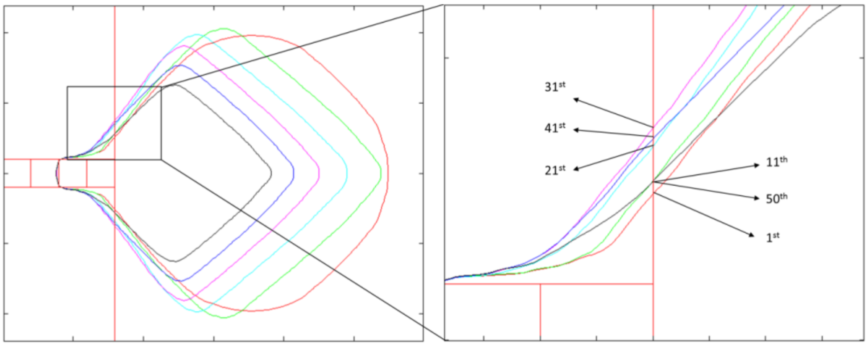

Figure 6-56 Intercepts of the 1st, 11th, 21st, 31st, 41st and 50th Droplet at the End of the Filling Stage for the ‘Conventional Reservoir’ Design

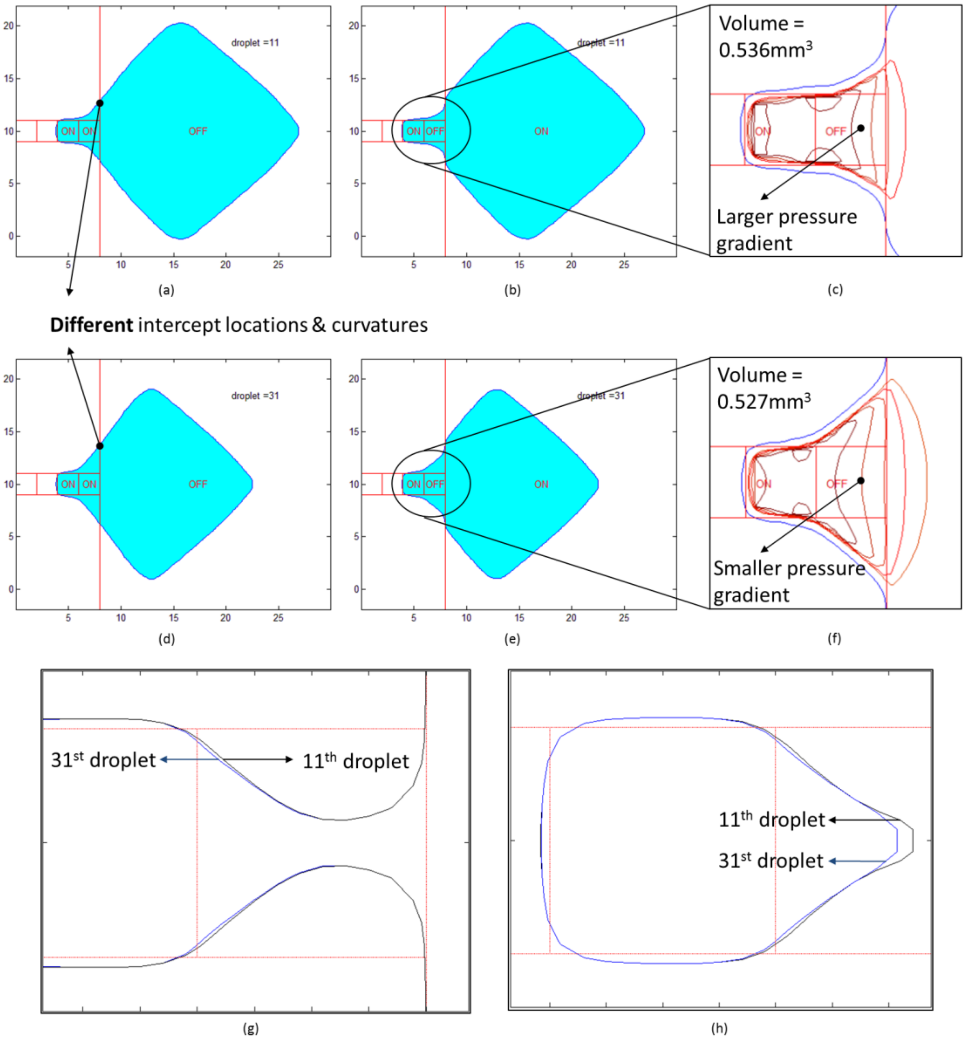

Figure 6-57 Numerical Results of the 11th and 31st Droplet for the 'Conventional Reservoir' Design: Liquid Shape at the End of the Filling Stage: 11th Droplet (a); 31st Droplet (d); Liquid Shape at the Beginning of the Cutting Stage: 11th Droplet (b); 31st Droplet (e); Pressure Fields at the Beginning of the Cutting Stage: 11th Droplet (c); 31st Droplet (f); Liquid Contour Right before the Pinch-off (g); Droplet Contour Right after the Pinch-off (h)

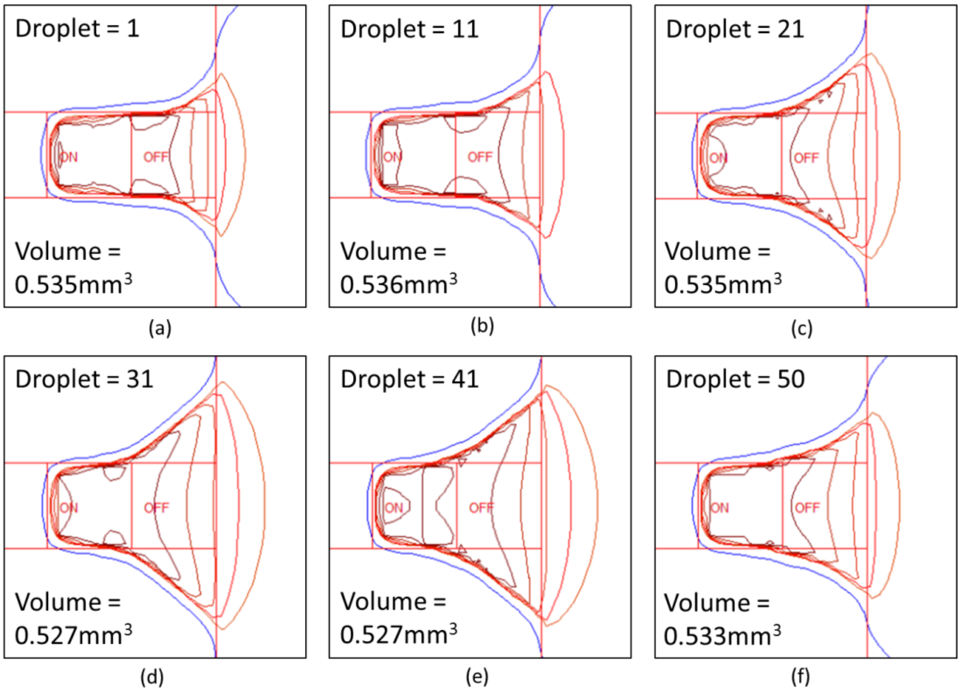

Figure 6-58 Pressure Fields on the Cutting Electrode at the Beginning of the Cutting Stage of the 1st, 11th, 21st, 31st, 41st and 50th Droplet (a-f) for the 'Conventional Reservoir' Design

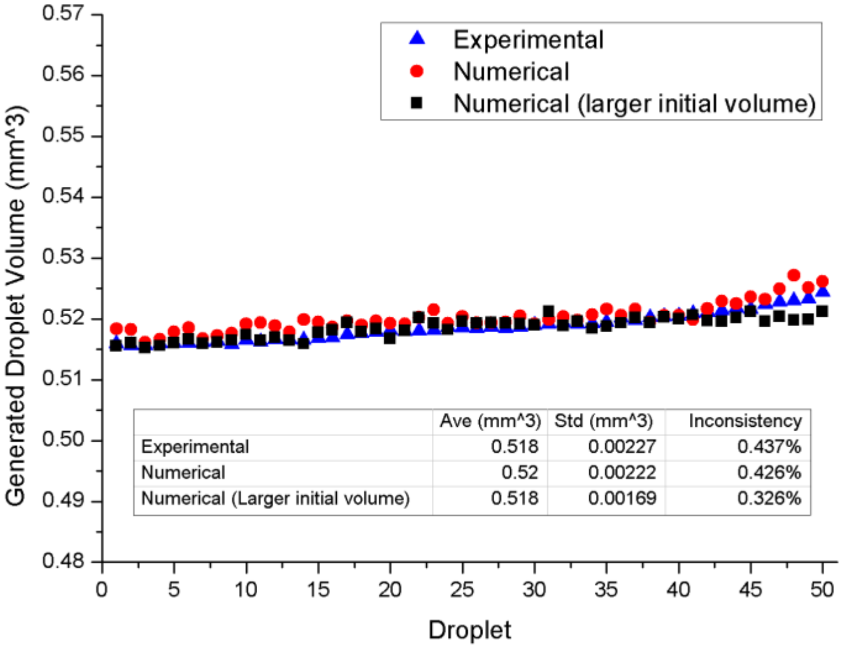

	Ave (mm^3)	Std (mm^3)	Inconsistency
Experimental	0.518	0.00227	0.437%
Numerical	0.52	0.00222	0.426%
Numerical (Larger initial volume)	0.518	0.00169	0.326%

Figure 6-59 Volume of Droplets Generated from the 'Stripped Reservoir' Design

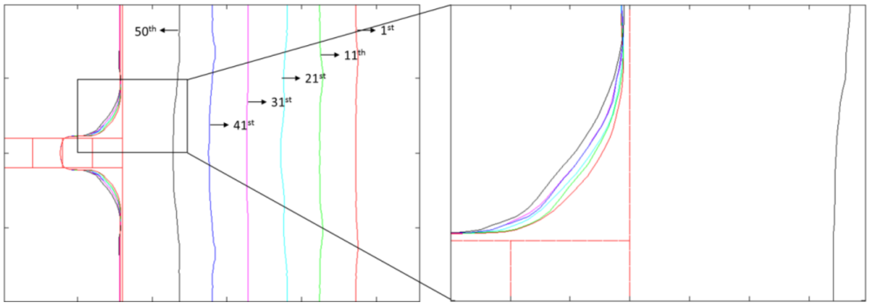

Figure 6-60 Free Surfaces of the 1st, 11th, 21st, 31st, 41st and 50th Droplet at the End of the Filling Stage for the ‘Stripped Reservoir’ Design

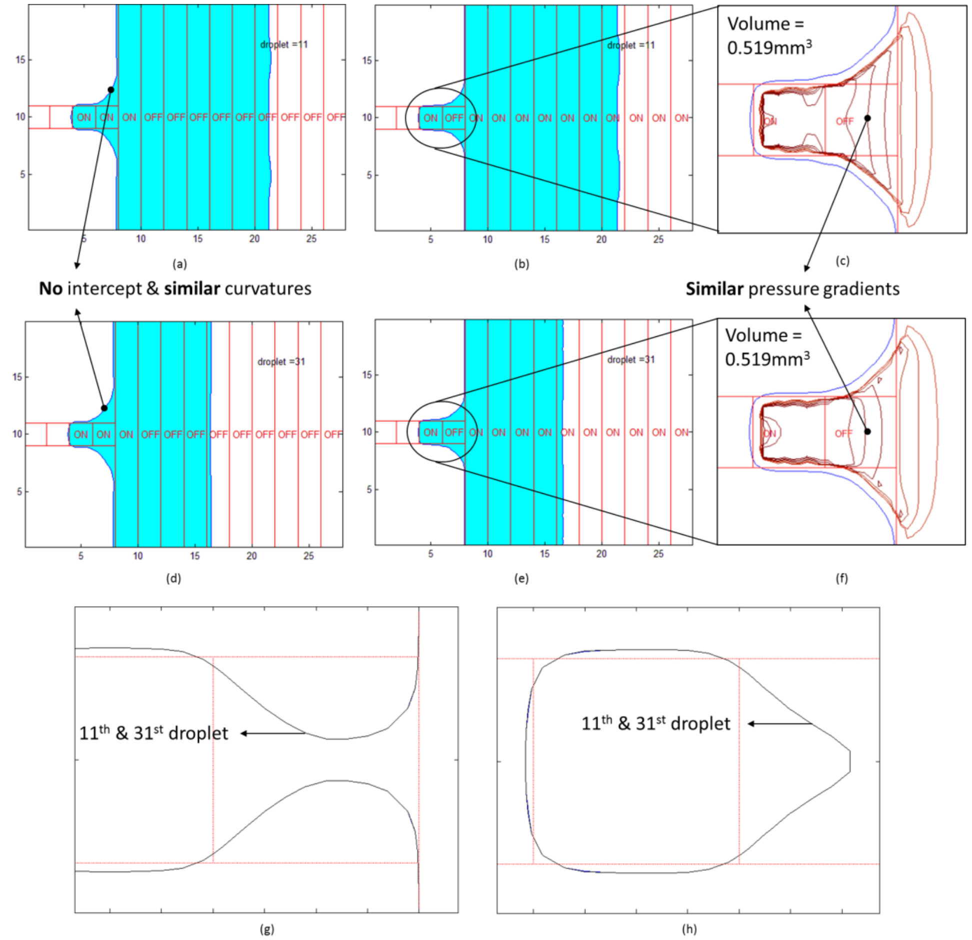

Figure 6-61 Numerical Results of the 11th and 31st Droplet for the ‘Stripped Reservoir’ Design: Liquid Shape at the End of the Filling Stage: 11th Droplet (a); 31st Droplet (d); Liquid Shape at the Beginning of the Cutting Stage: 11th Droplet (b); 31st Droplet (e); Pressure Fields at the Beginning of the Cutting Stage: 11th Droplet (c); 31st Droplet (f); Liquid Contour Right before the Pinch-off (g); Droplet Contour Right after the Pinch-off (h)

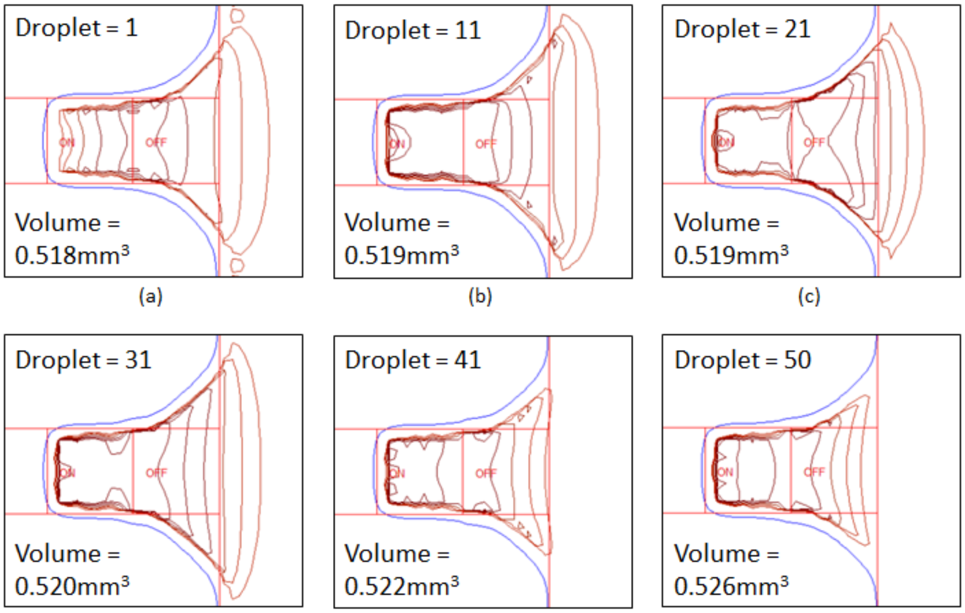

(a) (b) (c)

(d) (e) (f)

Figure 6-62 Pressure Fields on the Cutting Electrode of the 1st, 11th, 21st, 31st, 41st and 50th Droplet (a-f) at the Beginning of the Cutting Stage for the ‘Stripped Reservoir’ Design

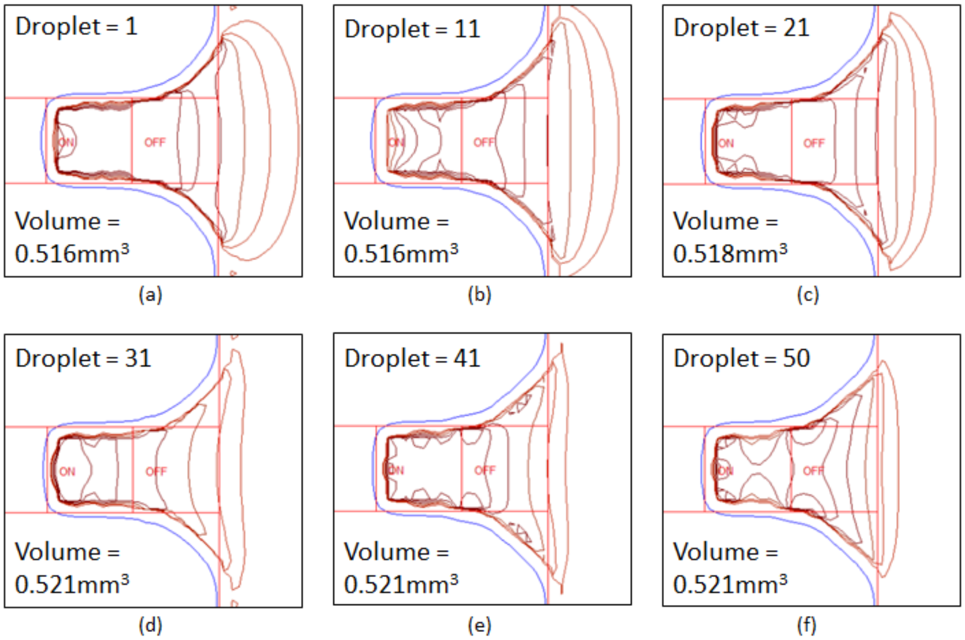

Figure 6-63 Pressure Fields on the Cutting Electrode of the 1st, 11th, 21st, 31st, 41st and 50th Droplet (a-f) at the Beginning of the Cutting Stage for the ‘Stripped Reservoir’ Design with Larger Initial Volume in the Reservoir

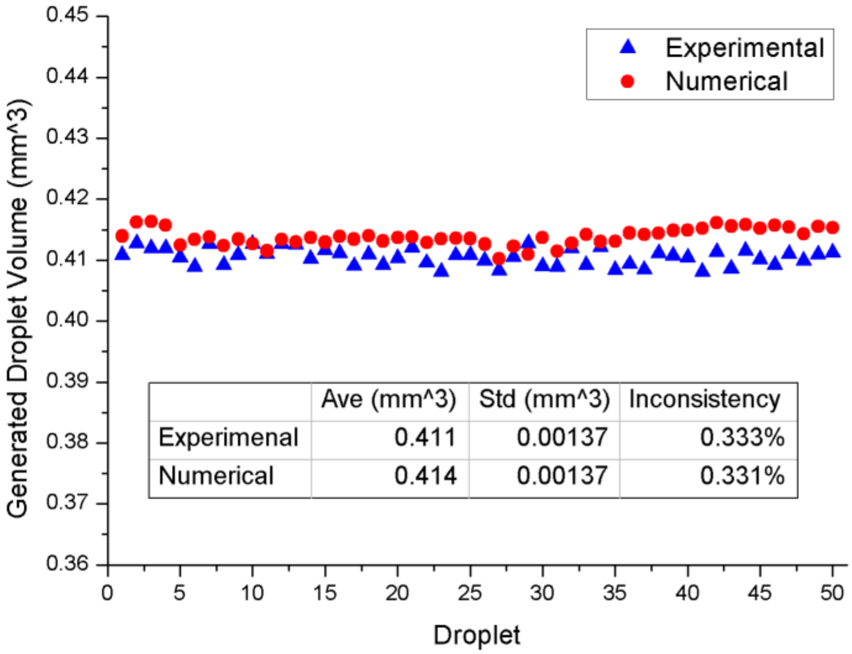

	Ave (mm^3)	Std (mm^3)	Inconsistency
Experimenal	0.411	0.00137	0.333%
Numerical	0.414	0.00137	0.331%

Figure 6-64 Volume of Droplets Generated from the 'TCC Reservoir' Design

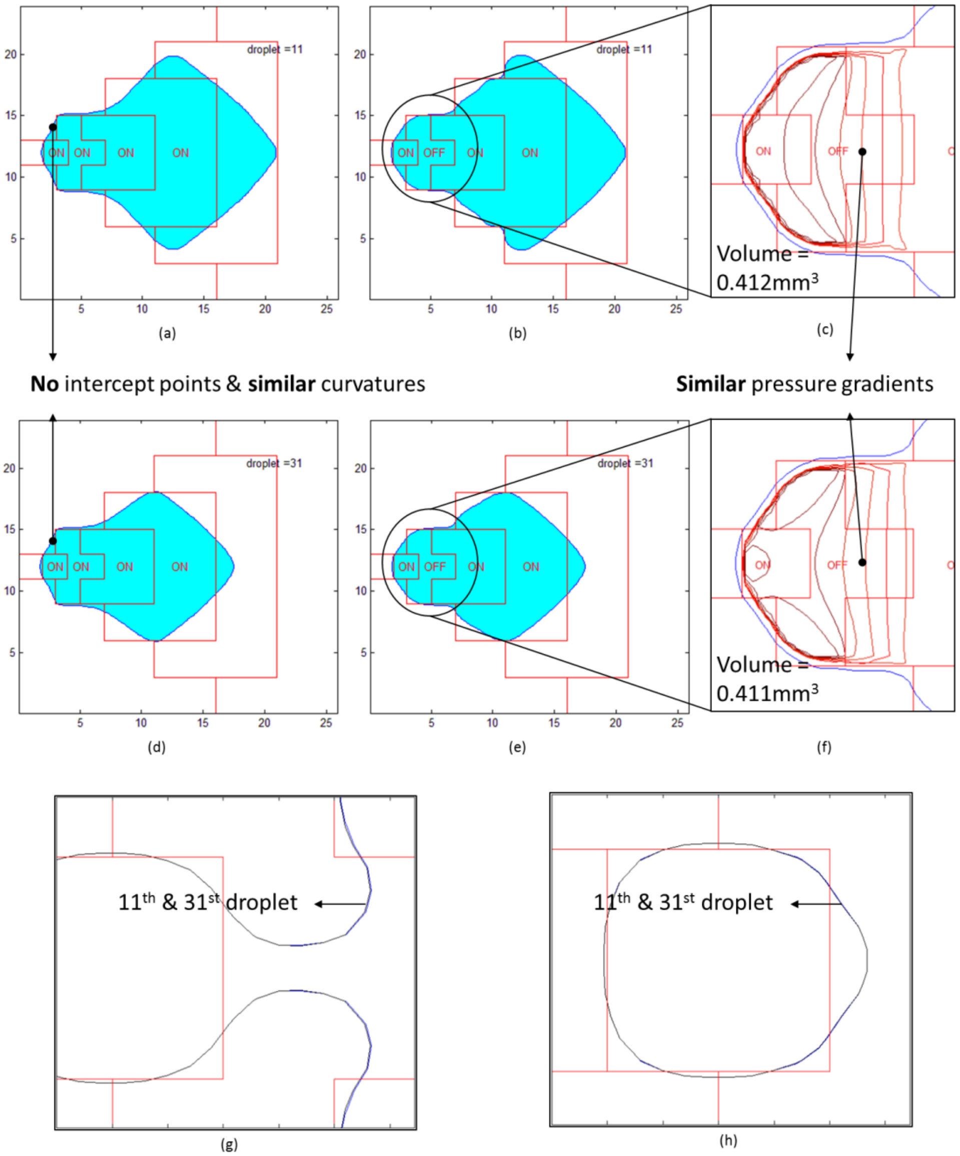

Figure 6-65 Numerical Results of the 11th and 31st Droplet for the 'TCC Reservoir' Design: Liquid Shape at the End of the Filling Stage: 11th Droplet (a); 31st Droplet (d); Liquid Shape at the Beginning of the Cutting Stage: 11th Droplet (b); 31st Droplet (e); Pressure Fields at the Beginning of the Cutting Stage: 11th Droplet (c); 31st Droplet (f); Liquid Contour Right before the Pinch-off (g); Droplet Contour Right after the Pinch-off (h)

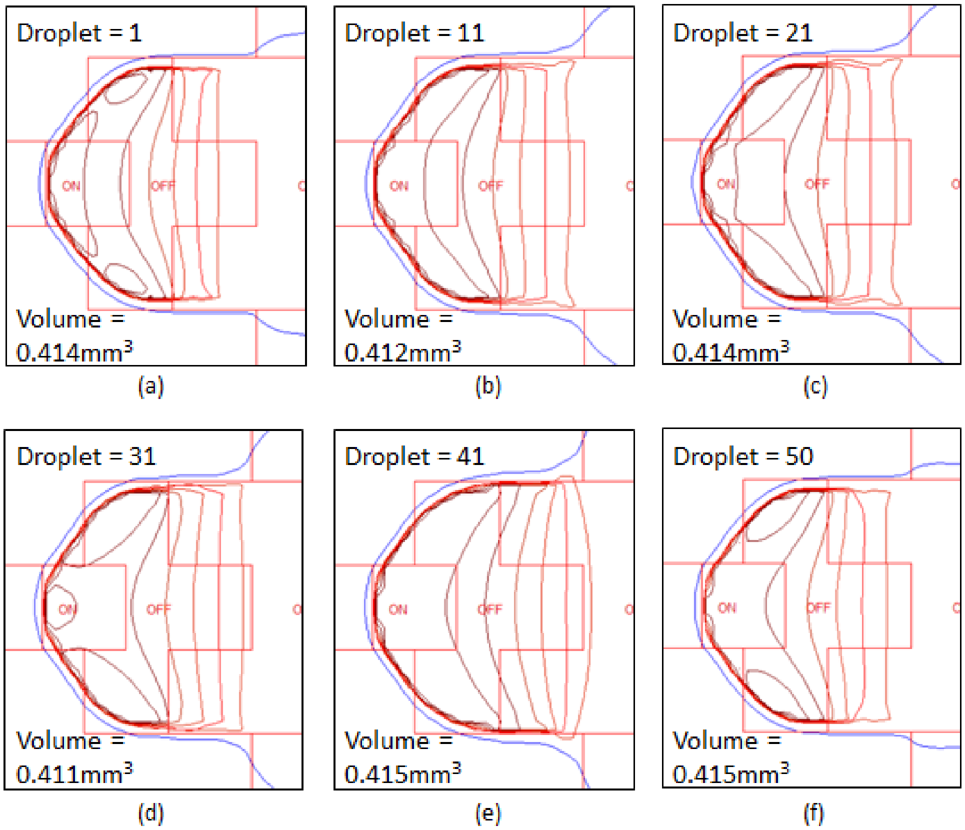

Figure 6-66 Pressure Fields on the Cutting Electrode of the 1st, 11th, 21st, 31st, 41st and 50th Droplet (a-f) at the Beginning of the Cutting Stage for the ‘TCC reservoir’ Design

Table 6-1 Parameters Used in the Current Study

Parameter	**Transport**	**Splitting**	**Merging**	**Dispensing**			**Unit**
				Conventional	**Stripped**	**TCC**	
ρ	996.93						kg/m^3
μ	0.89						g/m*s
σ	0.07199						N/m
L_E	2	1.4	1.5	N/A	N/A	N/A	mm
H	0.1	0.07	0.1	0.1	0.1	0.1	mm
V	N/A	25	65	N/A	N/A	N/A	volt
U_R	100	30	20	10	10	10	mm/s
Δ_A	4	8	8	3.1	4	3.8	degree
Δ_R	4	8	8	3.1	4	3.8	degree
$\theta_{s, OFF}$	117	117	111.62	117	117	117	degree
$\theta_{s, ON}$	54	90	70.01	90	90	90	degree
Ca	1.236×10^{-3}	3.709×10^{-4}	2.473×10^{-4}	1.236×10^{-4}	1.236×10^{-4}	1.236×10^{-4}	dimensionless
Re	11.201	2.352	2.240	1.120	1.120	1.120	dimensionless
We	1.385×10^{-2}	8.724×10^{-4}	5.539×10^{-4}	1.385×10^{-4}	1.385×10^{-4}	1.385×10^{-4}	dimensionless
Oh	1.051×10^{-2}	1.256×10^{-2}	1.051×10^{-2}	1.051×10^{-2}	1.051×10^{-2}	1.051×10^{-2}	dimensionless
Bo	1.357×10^{-3}	6.650×10^{-4}	1.357×10^{-3}	1.357×10^{-3}	1.357×10^{-3}	1.357×10^{-3}	dimensionless

Table 6-2 Droplet Transport Time versus Static Contact Angles

$\theta_{s,ON}$	$\theta_{s,OFF}$	$\theta_{s,OFF}-\theta_{s,ON}$	$\Delta\kappa_z$	$\tilde{k}$	**Transport time (ms)**
74	97	23	3.975	4.485	160
74	102	28	4.835	5.456	100
74	107	33	5.680	6.409	74
74	112	38	6.502	7.337	64
74	117	43	7.296	8.233	53
64	107	43	7.307	8.246	53
59	107	48	8.074	9.111	48
64	112	48	8.130	9.173	48
54	107	53	8.802	9.932	47
59	112	53	8.896	10.039	45
64	117	53	8.924	10.069	46
49	107	58	9.484	10.702	44
54	112	58	9.624	10.859	44
64	122	58	9.683	10.926	43
59	117	58	9.690	10.934	42
44	107	63	10.117	11.416	45
49	112	63	10.307	11.630	45
64	127	63	10.402	11.737	44
54	117	63	10.418	11.755	44
59	122	63	10.450	11.791	45
44	112	68	10.939	12.344	48
49	117	68	11.100	12.526	48
59	127	68	11.169	12.602	49
54	122	68	11.177	12.612	48
44	117	73	11.733	13.240	pinch-off @ 25
49	122	73	11.860	13.382	pinch-off @ 24
54	127	73	11.896	13.423	pinch-off @ 25
44	122	78	12.493	14.096	pinch-off @ 20
49	127	78	12.579	14.194	pinch-off @ 19
44	127	83	13.212	14.908	pinch-off @ 18

Table 6-3 Droplet Transport Time versus Electrode Size, Channel Height and Dimensionless Curvature

1×1 mm^2		
H (mm)	$\tilde{\boldsymbol{k}}$	**Transport time (ms)**
0.03	19.592	pinchoff @ 21
0.035	16.793	pinchoff @ 19
0.04	14.694	pinchoff @ 18
0.045	13.061	28
0.05	11.755	22
0.06	9.796	18
0.07	8.397	16
0.08	7.347	14
0.09	6.531	13
0.1	5.878	12
0.11	5.343	11
0.12	4.898	10
0.2	2.939	8

2×2 mm^2		
H (mm)	$\tilde{\boldsymbol{k}}$	**Transport time (ms)**
0.04	29.388	pinchoff @ 30
0.05	23.510	pinchoff @ 32
0.06	19.592	pinchoff @ 37
0.07	16.793	pinchoff @ 35
0.08	14.694	pinchoff @ 35
0.09	13.061	59
0.1	11.755	44
0.11	10.687	36
0.12	9.796	33
0.13	9.042	29
0.14	8.397	26
0.15	7.837	24
0.16	7.347	23
0.17	6.915	22
0.18	6.531	21
0.19	6.187	20
0.2	5.878	19
0.21	5.598	19
0.22	5.343	19
0.23	5.111	18
0.24	4.898	18
0.25	4.702	18

Table 6.3—*Continued*

3×3 mm^2		
H (mm)	$\tilde{k}$	**Transport time (ms)**
0.06	29.388	pinchoff @ 46
0.07	25.190	pinchoff @ 48
0.08	22.041	pinchoff @ 50
0.09	19.592	pinchoff @ 50
0.1	17.633	pinchoff @ 52
0.11	16.030	pinchoff @ 50
0.12	14.694	pinchoff @ 52
0.13	13.564	pinchoff @ 54
0.14	12.595	92
0.15	11.755	78
0.16	11.020	64
0.17	10.372	56
0.18	9.796	52
0.19	9.280	50
0.2	9.376	48
0.25	7.053	42
0.3	6.251	38

4×4 mm^2		
H (mm)	$\tilde{k}$	**Transport time (ms)**
0.06	39.184	pinchoff @ 52
0.07	33.586	pinchoff @ 52
0.08	29.388	pinchoff @ 56
0.09	26.123	pinchoff @ 60
0.1	23.510	pinchoff @ 64
0.11	21.373	pinchoff @ 72
0.12	19.592	pinchoff @ 68
0.13	18.085	pinchoff @ 72
0.14	16.793	pinchoff @ 68
0.15	15.674	pinchoff @ 68
0.16	14.694	pinchoff @ 68
0.17	13.830	pinchoff @ 68
0.18	13.061	pinchoff @ 76
0.19	12.374	132
0.2	11.755	108
0.25	9.404	68
0.3	7.837	60
0.35	6.717	56
0.4	5.878	52

Chapter 7

Conclusions and Future Work

The fluid dynamics of microfluidic droplet motions in parallel-plate EWOD devices including transport, splitting, merging and dispensing have been investigated via a numerical scheme. The Navier-Stokes equations are solved using a finite volume formulation with a two-step projection method on a fixed computational grid. A CLSVOF method is used for tracking the gas-liquid interface in conjunction with the CSF scheme for the surface tension calculation. Contact angle hysteresis which is a crucial element in EWOD modeling has been implemented. A simplified model has been adopted for the viscous stresses exerted by the parallel plates on the solid-liquid interface. The numerical results obtained from the current study are in good agreement with the corresponding experiments for all droplet operations.

For the droplet transport process, it has been discovered that the pressure jump at the ON/OFF electrode border may lead to the formation of two localized areas which directly determine the direction and speed of the fluid flow and consequently play a dominant role in the transport process. It has been found that the droplet experiences a larger deformation and even a splitting when the difference between $\theta_{s,OFF}$ and $\theta_{s,ON}$ is increased, when the channel height is reduced or when the electrode size is increased with the droplet diameter maintained at the same ratio with the electrode length. However, varying density, viscosity, surface tension or the viscous stresses exerted by the parallel plates appears to only alter the transport speed with the shape unchanged. A dimensionless curvature $\tilde{k}$ has been introduced which represents the relative significance between $\Delta\kappa_z$ and κ_{xy} in a particular droplet transport case. The critical value of $\tilde{k}$ beyond which the droplet splits into two small ones during the transport has been found which appears to be universal for all the transport cases studied.

Similar to the transport process, the results of droplet splitting and merging processes show that altering the channel height has a profound effect on droplet motions for both splitting and merging cases since it affects the surface tension induced pressure as well as the viscous force exerted by the plates. However, changing the values of density, viscosity and surface tension seems to only vary the liquid moving speed with the shape unaltered. For the splitting process, it has been discovered that a small satellite droplet is formed when the channel height is between 0.03mm and 0.04mm resulting from the more curved pressure contours in the localized areas near the ON/OFF electrode border. When the channel height is beyond 0.105mm, the splitting never occurs due to the insufficient pressure force across the droplet boundary in the middle of the splitting process. For the merging process, the merging always occurs regardless of the channel height but at a faster pace when the channel height is increased, which results from the less curved pressure contours in the localized areas.

The physics involved in the droplet dispensing process has been studied for three different reservoir designs and the volume inconsistency of generated droplets has been examined. It has been discovered that the pressure distribution on the cutting electrode at the beginning of the cutting stage is of considerable significance for the inconsistency of droplet volumes, which can be improved by stabilizing the intercept of the liquid interface at left reservoir boundary at the end of the filling stage. Smaller volume inconsistency can also be achieved by shortening the liquid cutting length, which reduces the size of the neck as well as the volume adding to the generated droplet after the pinch-off. It has been found that the ‘stripped reservoir’ design has smaller volume inconsistency than the ‘conventional reservoir’ design due to the elimination of the intercept at left reservoir boundary. However, the ‘stripped reservoir’ design becomes unreliable when the liquid in the reservoir is near depletion. The ‘TCC reservoir’ design is the best among the three designs since it is capable of generating droplet with excellent volume uniformity as well as a volume close to the size of the generating electrode due to a much shorter neck formed in the cutting stage.

The applications in the present study demonstrate the versatility and robustness of the numerical EWOD schemes which are capable of accurately modeling a variety of microfluidic droplet motions. However, it should be noted that the current methods are limited to the two dimensional case and the extension to three-dimensional problems is desirable but excepted to be more difficult and challenged (i.e., a more complex interface reconstruction scheme is needed). Besides, the current code is unable to solve low Reynolds number flow problems due to the explicit treatment of the viscous term in the Navier-Stokes equation. An implicit treatment of the viscous term will allow the code to model more viscous fluids and to eliminate the time step constraints due to the viscosity. Also, only the continuity and the momentum equations are solved in the current codes; adding an energy equation model with phase-change will allow the code to simulate two-phase interfacial flows with heat transfer and evaporation. With these further enhancements, the range and variety of current numerical EWOD model can be improved and extended to some interdisciplinary studies.

Appendix A

Computer Program Execution

All numerical computations were performed on the High Performance Computing (HPC) environment of The University of Texas at Arlington. The system operates with Compaq ES40 Alpha servers with quad 833MHz 64-bit EV68 and Compaq DS20E Alpha servers with dual 667MHz 64-bit EV67 processors. The servers operate on Intel Core i7 processor (Nahalem) architectures and use Red Hat Enterprise Linux for their operating environment.

The computational program used for the present study was developed based on a single-phase flow solver [121], which was written in the computer language FORTRAN under the UNIX/LINUX operating system. Major modifications were made to two subroutines of the original CLSVOF code, tension.f and vtilde.f. Subroutine tension.f was modified to account for electrode locations, interface moving directions, static contact angles at both plates and the hysteresis effect in the CSF method. The viscous stress exerted by the parallel plates was applied in the subroutine vtilde.f where the viscous terms in the Navier-Stokes equations are computed. Some minor changes have been made to comdk1.h and rinput.f for the new namelists added to the input file.

In setting up a problem for computation, three files are required to be placed in a same directory: (1) the input file in which the problem geometry, initial conditions, fluid properties, numerical parameters, the I/O (input/output), the surface reconstruction method and the free surface tracking scheme, either the VOF or the CLSVOF, are specified; (2) the file_nam.dat file which contains the number and names of output data; (3) the bjob file which contains the load sharing facility (LSF) instructions and the path of the compiled executable file ripple. The information from the input file is fed to file ripple, in which the variables are grouped into format-free namelists.

When the computation is in process, a data file is periodically generated by the program at the time instant following the outputting frequency specified in the input file.

The number of files to be generated is listed in the file_nam.dat file. If the program generates more than the numbers specified in the file_nam.dat file, the last file is overwritten until the program finishes the computation. Each output data file contains the solutions in a specified format as follows:

1. The first and last real cells in the x- and y-direction

2. Location of the left side of each computational cell in the x-direction and the lower side of each computational cell in the y-direction

3. Data: the velocity in the x-direction, the velocity in the y-direction, the volume fractions (VOF function value), the level set (LS) function value, the enthalpy and the pressure.

In the present study, the post processing of the data obtained from the simulation was done in MATLAB®, in which the output data files ripp*.dat, ripp*.da and ripp*.d are read and converted into the plots and graphs of the numerical simulations. Sample input and output files are given in Appendix B. Further information on setting up the problem can be found in [121] and [122].

Appendix B

Sample Input and Output

B.1 Sample INPUT

Two namelists $ewodrf and $gapspacing have been added to the original input file for the present study and the corresponding modifications have been made to the subroutines comdk1.h and rinput.f in the original CLSVOF code. In the namelist $ewodrf, the values of several EWOD parameters including the viscous stress coefficient λ_{vs}, the hysteresis deflections Δ_R and Δ_A and the static contact angles $\theta_{b,ON}$ and $\theta_{b,OFF}$ are provided. The magnitude of the channel height H is given in the namelist $gapspacing. All the other parameters are taken from a previous version of the code and the details are available in [121] and [122]. A sample input file is shown below.

```
Droplet transport process in EWOD devices by Yin Guan
$numparam
  alpha=1.0,
  conserve=.false.,
  autot=1.0,
  delt=0.25e-2,
  dtmax=0.25e-1,
  twfin=10000.0,
  con=0.3,
  fcvlim=0.5,
  idiv=1,
  dmpdt=3000000.0,
  prtdt=1000000.0,
  pltdt=1.0,
  sym=.true.,
```

```
  kt=2,
  kb=2,
  kl=2,
  kr=2,
$end
$fldparam
  gy=0.0,
  icyl=0,
  isurf10=1,
  psat = 0.0,
  xnu=8.927407e-4,
  rhof=0.99693,
  sigma=0.07199,
$end
$mesh
  nkx=1,
  xl=0.0,4.8,
  xc=2.4,
  nxl=48,
  nxr=48,
  dxmn=0.05,
  nky=1,
  yl=0.0,2.8,
  yc=1.4,
  nyl=28,
```

```
  nyr=28,
  dymn=0.05,
$end
$obstcl
  nobs=0,
$end
$freesurf
  nfrsrf=2,iequib=0,
  fc1(1)=-1.0, ifh(1)=1,
  fa2(2)=1.0, fa1(2)=-6.8, fb2(2)=1.0, fb1(2)=-2.8,
  fc1(2)=12.08, ifh(2)=0,
$end
$graphics
  plots=.true., dump=.false.,
  iout = 0, 1, 0, 0, 0, 0, 0, 0, 0, 0, 0, 0, 0,
         0, 0, 0, 0, 0, 0, 0, 0, 0, 0, 0, 0, 0,
         0, 0, 0, 0, 0, 0, 0, 1, 0, 0, 0, 0, 1,
  iysymplt=0,
$end
$heateq
  heat= .false.,
  ischeme=3,
$end
$coupled
  lsvof=.true.,
```

ls=.false.,

$end

$ewodrf

covs=18.0, <------ viscous stress coefficient λ_{vs}

cahaa=4.0, <------ hysteresis deflection on the advancing side Δ_A

cahra=4.0, <------ hysteresis deflection on the receding side Δ_R

caon=54.0, <------ static contact angle on the activated area $\theta_{b,ON}$

caoff=117.0, <------ static contact angle on the non-activated area $\theta_{b,OFF}$

$end

$gapspacing

gapsp=0.10, <------ channel height H

$end

B.2 Sample OUTPUT

The data files contains the solutions of the governing equations are named according to the file_nam.dat file. A sample output file and its explanations are given below.

0.00000E+000 <----- time

2, 96 <----- 1st real cell, last real cell in x-direction

2, 56 <----- 1st real cell, last real cell in y-direction

0.00000E+000 <----- location of the left side of each computational cell in the x-direction

1.00000E-001

2.00000E-001

3.00000E-001

4.00000E-001

5.00000E-001

6.00000E-001

.

.

.

.

0.00000E+000 <----- location of the left side of each computational cell in the y-direction

1.00000E-001

2.00000E-001

3.00000E-001

4.00000E-001

5.00000E-001

6.00000E-001

7.00000E-001

8.00000E-001

9.00000E-001

1.00000E+000

.

.

.

0.00000E+0, -4.50000E-1, 0.00000E+0, 1.00000E+6, 0.00000E+0, 0.00000E+0

0.00000E+0, -4.50000E-1, 0.00000E+0, 1.00000E+6, 0.00000E+0, 0.00000E+0

```
0.00000E+0, -4.50000E-1, 0.00000E+0, 1.00000E+6, 0.00000E+0, 0.00000E+0
0.00000E+0, -4.50000E-1, 0.00000E+0, 1.00000E+6, 0.00000E+0, 0.00000E+0
0.00000E+0, -4.50000E-1, 0.00000E+0, 1.00000E+6, 0.00000E+0, 0.00000E+0
.
.
.
(comp. 1),   (comp.2),     (comp. 3),   (comp. 4),   (comp.5),    (comp.6)
```

In the above six-column matrix, components from comp.1 to comp.6 show the following solutions:

comp.1: velocity component in x-direction

comp.2: velocity component in y-direction

comp.3: VOF function value

comp.4: LS function value

comp.5: enthalpy

comp.6: pressure

References

[1] M. J. Madou, *Fundamentals of Microfabrication: The Science of Miniaturization*: CRC Press, 2002.

[2] R. Fair, "Digital microfluidics: is a true lab-on-a-chip possible?," *Microfluidics and Nanofluidics,* vol. 3, pp. 245-281, 2007.

[3] J. Berthier, *Micro-drops and digital microfluidics*: William Andrew, 2012.

[4] M. Washizu, "Electrostatic actuation of liquid droplets for micro-reactor applications," *Industry Applications, IEEE Transactions on,* vol. 34, pp. 732-737, 1998.

[5] T. S. Sammarco and M. A. Burns, "Thermocapillary pumping of discrete drops in microfabricated analysis devices," *AIChE Journal,* vol. 45, pp. 350-366, 1999.

[6] A. A. Darhuber, J. M. Davis, S. M. Troian, and W. W. Reisner, "Thermocapillary Actuation of Liquid Flow on Chemically Patterned Surfaces," *Physics of Fluids,* vol. 15, pp. 1295-1304, 2003.

[7] S. Böhm, B. Timmer, W. Olthuis, and P. Bergveld, "A closed-loop controlled electrochemically actuated micro-dosing system," *Journal of Micromechanics and Microengineering,* vol. 10, p. 498, 2000.

[8] T. B. Jones, M. Gunji, M. Washizu, and M. Feldman, "Dielectrophoretic liquid actuation and nanodroplet formation," *Journal of Applied Physics,* vol. 89, pp. 1441-1448, 2001.

[9] N.-T. Nguyen, K. M. Ng, and X. Huang, "Manipulation of ferrofluid droplets using planar coils," *Applied physics letters,* vol. 89, pp. 052509-052509-3, 2006.

[10] M. G. Pollack, A. D. Shenderov, and R. B. Fair, "Electrowetting-Based Actuation of Droplets for Integrated Microfluidics," *Lab on a Chip,* vol. 2, pp. 96-101, May 2002.

[11] S. K. Cho, H. Moon, and C.-J. Kim, "Creating, Transporting, Cutting, and Merging Liquid Droplets by Electrowetting-Based Actuation for Digital Microfluidic Circuits," *Journal of Microelectromechanical Systems,* vol. 12, pp. 70-80, 2003.

[12] G. Lippmann, "Relations entre les phénomènes électriques et capillaires," Gauthier-Villars, 1875.

[13] A. Klingner and F. Mugele, "Electrowetting-induced Morphological Transitions of Fluid Microstructures," *Journal of Applied Physics,* vol. 95, pp. 2918-2920, 2004.

[14] F. Mugele and J.-C. Baret, "Electrowetting: from Basics to Applications," *Journal of Physics: Condensed Matter,* vol. 17, pp. R705-R774, 2005.

[15] A. A. Darhuber and S. M. Troian, "Principles of Microfluidic Actuation by Modulation of Surface Stresses," *Annual Review of Fluid Mechanics,* vol. 37, pp. 425-455, 2005.

[16] F. Mugele, M. Duits, and D. van den Ende, "Electrowetting: a versatile tool for drop manipulation, generation, and characterization," *Adv Colloid Interface Sci,* vol. 161, pp. 115-23, Dec 15 2010.

[17] L. S. Jang, G. H. Lin, Y. L. Lin, C. Y. Hsu, W. H. Kan, and C. H. Chen, "Simulation and Experimentation of a Microfluidic Device Based on Electrowetting on Dielectric," *Biomed Microdevices,* vol. 9, pp. 777-86, Dec 2007.

[18] J. Gong and C. J. Kim, "All-electronic droplet generation on-chip with real-time feedback control for EWOD digital microfluidics," *Lab Chip,* vol. 8, pp. 898-906, Jun 2008.

[19] S. W. Walker and B. Shapiro, "Modeling the Fluid Dynamics of Electrowetting on Dielectric (EWOD)," *Journal of Microelectromechanical Systems,* vol. 15, pp. 986-1000, 2006.

[20] S. W. Walker, B. Shapiro, and R. H. Nochetto, "Electrowetting with Contact Line Pinning: Computational Modeling and Comparisons with Experiments," *Physics of Fluids,* vol. 21, p. 102103, 2009.

[21] W. Wang, "On-chip double emulsion droplet assembly using electrowetting-on-dielectric and dielectrophoresis," University of Rochester, 2012.

[22] H. W. Lu, K. Glasner, A. L. Bertozzi, and C. J. Kim, "A diffuse-interface model for electrowetting drops in a Hele-Shaw cell," *Journal of Fluid Mechanics,* vol. 590, 2007.

[23] K.-L. Wang and T. Jones, "Electrowetting Dynamics of Microfluidic Actuation," *Langmuir,* vol. 21, pp. 4211-4217, 2005.

[24] C. Decamps and J. De Coninck, "Dynamics of Spontaneous Spreading under Electrowetting Conditions," *Langmuir,* vol. 16, pp. 10150-10153, 2000.

[25] J. M. Oh, S. H. Ko, and K. H. Kang, "Analysis of Electrowetting-Driven Spreading of a Drop in Air," *Physics of Fluids,* vol. 22, p. 032002, 2010.

[26] K. Hoshino, S. Triteyaprasert, K. Matsumoto, and I. Shimoyama, "Electrowetting-Based Actuation for Microinjection," in *Proc. TRANSDUCERS, Solid-State Sensors, Actuators and Microsystems, 12th International Conference on*, 2003, pp. 1800-1803.

[27] A. R. Wheeler, H. Moon, C.-J. C. Kim, J. A. Loo, and R. L. Garrell, "Electrowetting-Based Microfluidics for Analysis of Peptides and Proteins by Matrix-Assisted Laser Desorption/Ionization Mass Spectrometry," *Analytical Chemistry,* vol. 76, pp. 4833-4838, 2004.

[28] B. Berge, "Electrocapillarité et mouillage de films isolants par l'eau," *Comptes rendus de l'Académie des sciences. Série 2, Mécanique, Physique, Chimie, Sciences de l'univers, Sciences de la Terre,* vol. 317, pp. 157-163, 1993.

[29] L. Minnema, H. Barneveld, and P. Rinkel, "An Investigation into the Mechanism of Water Treeing in Polyethylene High-Voltage Cables," *Electrical Insulation, IEEE Transactions on,* pp. 461-472, 1980.

[30] H. Moon, S. K. Cho, R. L. Garrell, and C.-J. C. Kim, "Low voltage electrowetting-on-dielectric," *Journal of Applied Physics,* vol. 92, p. 4080, 2002.

[31] J. B. Yaddessalage, "Study Of The Capabilities Of Electrowetting On Dielectric Digital Microfluidics (EWOD DMF) Towards The High Efficient Thin-film Evaporative Cooling Platform," 2013.

[32] M. G. Pollack, R. B. Fair, and A. D. Shenderov, "Electrowetting-based actuation of liquid droplets for microfluidic applications," *Applied Physics Letters,* vol. 77, p. 1725, 2000.

[33] J.-h. Chang and J. J. Pak, "Effect of contact angle hysteresis on electrowetting threshold for droplet transport," *Journal of Adhesion Science and Technology,* vol. 26, pp. 2105-2111, 2012.

[34] M. G. Pollack, "Electrowetting-based microactuation of droplets for digital microfluidics," Duke University, 2001.

[35] J. Zeng and T. Korsmeyer, "Principles of droplet electrohydrodynamics for lab-on-a-chip," *Lab Chip,* vol. 4, pp. 265-77, Aug 2004.

[36] K. Mohseni, A. Arzpeyma, and A. Dolatabadi, "Behaviour of a moving droplet under electrowetting actuation: numerical simulation," *The Canadian Journal of Chemical Engineering,* vol. 84, pp. 17-21, 2006.

[37] V. Bahadur and S. V. Garimella, "An energy-based model for electrowetting-induced droplet actuation," *Journal of Micromechanics and Microengineering,* vol. 16, pp. 1494-1503, 2006.

[38] A. Arzpeyma, S. Bhaseen, A. Dolatabadi, and P. Wood-Adams, "A coupled electro-hydrodynamic numerical modeling of droplet actuation by electrowetting," *Colloids and Surfaces A: Physicochemical and Engineering Aspects,* vol. 323, pp. 28-35, 2008.

[39] L. Clime, D. Brassard, and T. Veres, "Numerical modeling of electrowetting processes in digital microfluidic devices," *Computers & Fluids,* vol. 39, pp. 1510-1515, 2010.

[40] Z. Keshavarz-Motamed, L. Kadem, and A. Dolatabadi, "Effects of Dynamic Contact Angle on Numerical Modeling of Electrowetting in Parallel Plate Microchannels," *Microfluidics and Nanofluidics,* vol. 8, pp. 47-56, 2009.

[41] H. Ren, R. B. Fair, and M. G. Pollack, "Automated on-chip droplet dispensing with volume control by electro-wetting actuation and capacitance metering," *Sensors and Actuators B: Chemical,* vol. 98, pp. 319-327, 2004.

[42] B. J. Kirby, *Micro-and nanoscale fluid mechanics: transport in microfluidic devices*: Cambridge University Press, 2010.

[43] D. Rose, "Microdispensing technologies in drug discovery," *Drug discovery today,* vol. 4, pp. 411-419, 1999.

[44] P. S. Dittrich and A. Manz, "Lab-on-a-chip: microfluidics in drug discovery," *Nature Reviews Drug Discovery,* vol. 5, pp. 210-218, 2006.

[45] J. Berthier, P. Clementz, O. Raccurt, D. Jary, P. Claustre, C. Peponnet*, et al.*, "Computer aided design of an EWOD microdevice," *Sensors and Actuators A: Physical,* vol. 127, pp. 283-294, 2006.

[46] Y. Fouillet, D. Jary, C. Chabrol, P. Claustre, and C. Peponnet, "Digital microfluidic design and optimization of classic and new fluidic functions for lab on a chip systems," *Microfluidics and Nanofluidics,* vol. 4, pp. 159-165, 2008.

[47] K. S. Elvira, R. Leatherbarrow, and J. Edel, "Droplet dispensing in digital microfluidic devices: Assessment of long-term reproducibility," *Biomicrofluidics,* vol. 6, p. 022003, 2012.

[48] W. C. Nelson and C.-J. C. Kim, "Droplet actuation by electrowetting-on-dielectric (EWOD): a review," *Journal of Adhesion Science and Technology,* vol. 26, pp. 1747-1771, 2012.

[49] H. Matsumoto and J. E. Colgate, "Preliminary Investigation of Micropumping Based on Electrical Control of Interfacial Tension," in *Proceedings: IEEE Micro Electro Mechanical Systems. An Investigation of Micro Structures, Sensors, Actuators, Machines and Robots*, 1990, pp. 105-110.

[50] B. Shapiro, H. Moon, R. L. Garrell, and C.-J. C. Kim, "Equilibrium behavior of sessile drops under surface tension, applied external fields, and material variations," *Journal of Applied Physics,* vol. 93, p. 5794, 2003.

[51] F. Mugele, "Fundamental challenges in electrowetting: from equilibrium shapes to contact angle saturation and drop dynamics," *Soft Matter,* vol. 5, p. 3377, 2009.

[52] A. Quinn, R. Sedev, and J. Ralston, "Contact angle saturation in electrowetting," *The journal of physical chemistry B,* vol. 109, pp. 6268-6275, 2005.

[53] M. Vallet, M. Vallade, and B. Berge, "Limiting phenomena for the spreading of water on polymer films by electrowetting," *The European Physical Journal B-Condensed Matter and Complex Systems,* vol. 11, pp. 583-591, 1999.

[54] F. Mugele and S. Herminghaus, "Electrostatic stabilization of fluid microstructures," *Applied physics letters,* vol. 81, pp. 2303-2305, 2002.

[55] H. Verheijen and M. Prins, "Reversible electrowetting and trapping of charge: model and experiments," *Langmuir,* vol. 15, pp. 6616-6620, 1999.

[56] V. Peykov, A. Quinn, and J. Ralston, "Electrowetting: a model for contact-angle saturation," *Colloid and Polymer Science,* vol. 278, pp. 789-793, 2000.

[57] A. I. Drygiannakis, A. G. Papathanasiou, and A. G. Boudouvis, "On the connection between dielectric breakdown strength, trapping of charge, and contact angle saturation in electrowetting," *Langmuir,* vol. 25, pp. 147-152, 2008.

[58] A. Papathanasiou and A. Boudouvis, "Manifestation of the connection between dielectric breakdown strength and contact angle saturation in electrowetting," *Applied Physics Letters,* vol. 86, p. 164102, 2005.

[59] A. Papathanasiou, A. Papaioannou, and A. Boudouvis, "Illuminating the connection between contact angle saturation and dielectric breakdown in electrowetting through leakage current measurementsa)," *Journal of Applied Physics,* vol. 103, p. 034901, 2008.

[60] G. K. Batchelor, *An Introduction to Fluid Dynamics*: Cambridge University Press, 2000.

[61] L. Gao and T. J. McCarthy, "Contact angle hysteresis explained," *Langmuir,* vol. 22, pp. 6234-6237, 2006.

[62] A. Hennig, K.-J. Eichhorn, U. Staudinger, K. Sahre, M. Rogalli, M. Stamm*, et al.*, "Contact angle hysteresis: study by dynamic cycling contact angle measurements and variable angle spectroscopic ellipsometry on polyimide," *Langmuir,* vol. 20, pp. 6685-6691, 2004.

[63] F. Li and F. Mugele, "How to make sticky surfaces slippery: Contact angle hysteresis in electrowetting with alternating voltage," *Applied Physics Letters,* vol. 92, p. 244108, 2008.

[64] R. Gupta, D. M. Sheth, T. K. Boone, A. B. Sevilla, and J. Frechette, "Impact of Pinning of the Triple Contact Line on Electrowetting Performance," *Langmuir,* vol. 27, pp. 14923-9, Dec 20 2011.

[65] L. Tanguy, T. Leïchlé, and L. Nicu, "Dynamic spreading of a liquid finger driven by electrowetting: Theory and experimental validation," *Journal of Applied Physics,* vol. 101, p. 044907, 2007.

[66] F. Hong, P. Cheng, Z. Sun, and H. Wu, "Simulation of spreading dynamics of a EWOD droplet with dynamic contact angle and contact angle hysteresis," 2009.

[67] T. Blake and J. Haynes, "Kinetics of liquidliquid displacement," *Journal of colloid and interface science,* vol. 30, pp. 421-423, 1969.

[68] P.-G. De Gennes, "Wetting: statics and dynamics," *Reviews of modern physics,* vol. 57, p. 827, 1985.

[69] E. Schäffer and P.-z. Wong, "Dynamics of contact line pinning in capillary rise and fall," *Physical review letters,* vol. 80, p. 3069, 1998.

[70] H. Ren, R. B. Fair, M. G. Pollack, and E. J. Shaughnessy, "Dynamics of electro-wetting droplet transport," *Sensors and actuators B: chemical,* vol. 87, pp. 201-206, 2002.

[71] R. Scardovelli and S. Zaleski, "Direct numerical simulation of free-surface and interfacial flow," *Annual Review of Fluid Mechanics,* vol. 31, pp. 567-603, 1999.

[72] W. Shyy, H. Udaykumar, M. M. Rao, and R. W. Smith, *Computational fluid dynamics with moving boundaries*: Courier Dover Publications, 2012.

[73] F. H. Harlow and J. E. Welch, "Numerical Study of Large-Amplitude Free-Surface Motions," *Physics of Fluids (1958-1988),* vol. 9, pp. 842-851, 1966.

[74] B. J. Daly, "Numerical Study of Two Fluid Rayleigh-Taylor Instability," *Physics of Fluids (1958-1988),* vol. 10, pp. 297-307, 1967.

[75] J. Glimm, C. Klingenberg, O. McBryan, B. Plohr, D. Sharp, and S. Yaniv, "Front tracking and two-dimensional Riemann problems," *Advances in Applied Mathematics,* vol. 6, pp. 259-290, 1985.

[76] I.-L. Chern, J. Glimm, O. McBryan, B. Plohr, and S. Yaniv, "Front tracking for gas dynamics," *Journal of Computational Physics,* vol. 62, pp. 83-110, 1986.

[77] S. O. Unverdi and G. Tryggvason, "A front-tracking method for viscous, incompressible, multi-fluid flows," *Journal of computational physics,* vol. 100, pp. 25-37, 1992.

[78] D. Juric and G. Tryggvason, "A front-tracking method for dendritic solidification," *Journal of Computational Physics,* vol. 123, pp. 127-148, 1996.

[79] G. Ryskin and L. Leal, "Numerical solution of free-boundary problems in fluid mechanics. Part 1. The finite-difference technique," *Journal of Fluid Mechanics,* vol. 148, pp. 1-17, 1984.

[80] G. Ryskin and L. Leal, "Numerical solution of free-boundary problems in fluid mechanics. Part 2. Buoyancy-driven motion of a gas bubble through a quiescent liquid," *Journal of Fluid Mechanics,* vol. 148, pp. 19-35, 1984.

[81] D. S. Dandy and L. G. Leal, "Buoyancy-driven motion of a deformable drop through a quiescent liquid at intermediate Reynolds numbers," *Journal of Fluid Mechanics,* vol. 208, pp. 161-192, 1989.

[82] C. Hirt, J. Cook, and T. Butler, "A Lagrangian method for calculating the dynamics of an incompressible fluid with free surface," *Journal of Computational Physics,* vol. 5, pp. 103-124, 1970.

[83] C. Hirt, A. A. Amsden, and J. Cook, "An arbitrary Lagrangian-Eulerian computing method for all flow speeds," *Journal of Computational Physics,* vol. 14, pp. 227-253, 1974.

[84] J. M. Hyman, "Numerical methods for tracking interfaces," *Physica D: Nonlinear Phenomena,* vol. 12, pp. 396-407, 1984.

[85] F. H. Harlow, "PIC and its progeny," *Computer Physics Communications,* vol. 48, pp. 1-10, 1988.

[86] J. J. Monaghan, "Smoothed particle hydrodynamics," *Annual review of astronomy and astrophysics,* vol. 30, pp. 543-574, 1992.

[87] T. Belytschko, Y. Krongauz, D. Organ, M. Fleming, and P. Krysl, "Meshless methods: an overview and recent developments," *Computer methods in applied mechanics and engineering,* vol. 139, pp. 3-47, 1996.

[88] H. A. Stone, B. Bentley, and L. Leal, "An experimental study of transient effects in the breakup of viscous drops," *Journal of Fluid Mechanics,* vol. 173, pp. 131-158, 1986.

[89] H. A. Stone and L. Leal, "Relaxation and breakup of an initially extended drop in an otherwise quiescent fluid," *Journal of Fluid Mechanics,* vol. 198, pp. 399-427, 1989.

[90] W. S. Hall, *Boundary Element Method*: Springer, 1994.

[91] B. Van Leer, "Towards the ultimate conservative difference scheme. IV. A new approach to numerical convection," *Journal of computational physics,* vol. 23, pp. 276-299, 1977.

[92] P. Colella and P. R. Woodward, "The piecewise parabolic method (PPM) for gas-dynamical simulations," *Journal of computational physics,* vol. 54, pp. 174-201, 1984.

[93] T. Yabe and F. Xiao, "Description of complex and sharp interface with fixed grids in incompressible and compressible fluid," *Computers & Mathematics with Applications,* vol. 29, pp. 15-25, 1995.

[94] B. Nichols and C. Hirt, "Technical Report LA-UR-75-1932," *Los Alamos National Laboratory,* 1975.
[95] C. W. Hirt and B. D. Nichols, "Volume of fluid (VOF) method for the dynamics of free boundaries," *Journal of computational physics,* vol. 39, pp. 201-225, 1981.
[96] W. J. Rider and D. B. Kothe, "Reconstructing volume tracking," *Journal of computational physics,* vol. 141, pp. 112-152, 1998.
[97] M. Rudman, "Volume-Tracking Methods for Interfacial Flow Calculations," *International Journal for Numerical Methods in Fluids,* vol. 24, pp. 671-691, 1997.
[98] M. Rudman, "A volume-tracking method for incompressible multifluid flows with large density variations," *International Journal for Numerical Methods in Fluids,* vol. 28, pp. 357-378, 1998.
[99] S. Osher and J. A. Sethian, "Fronts propagating with curvature-dependent speed: algorithms based on Hamilton-Jacobi formulations," *Journal of computational physics,* vol. 79, pp. 12-49, 1988.
[100] S. O. R. Fedkiw, "Level set methods and dynamic implicit surfaces," 2003.
[101] J. Sethian and P. Smereka, "Level set methods for fluid interfaces," *Annual Review of Fluid Mechanics,* vol. 35, pp. 341-372, 2003.
[102] M. Sussman, P. Smereka, and S. Osher, "A Level Set Approach for Computing Solutions to Incompressible Two-Phase Flow," *Journal of Computational Physics,* vol. 114, pp. 146-159, 1994.
[103] G. Tryggvason, B. Bunner, A. Esmaeeli, D. Juric, N. Al-Rawahi, W. Tauber*, et al.*, "A front-tracking method for the computations of multiphase flow," *Journal of Computational Physics,* vol. 169, pp. 708-759, 2001.
[104] S. Shin and D. Juric, "Modeling three-dimensional multiphase flow using a level contour reconstruction method for front tracking without connectivity," *Journal of Computational Physics,* vol. 180, pp. 427-470, 2002.
[105] S. Shin, S. Abdel-Khalik, V. Daru, and D. Juric, "Accurate representation of surface tension using the level contour reconstruction method," *Journal of Computational Physics,* vol. 203, pp. 493-516, 2005.
[106] M. Kang, R. P. Fedkiw, and X.-D. Liu, "A boundary condition capturing method for multiphase incompressible flow," *Journal of Scientific Computing,* vol. 15, pp. 323-360, 2000.
[107] M. D. Torrey, L. D. Cloutman, R. C. Mjolsness, and C. Hirt, "NASA-VOF2D: a computer program for incompressible flows with free surfaces," *NASA STI/Recon Technical Report N,* vol. 86, p. 30116, 1985.
[108] N. Mangiavacchi, A. Castelo, M. F. Tomé, J. A. Cuminato, M. L. B. de Oliveira, and S. McKee, "An effective implementation of surface tension using the marker and cell method for axisymmetric and planar flows," *SIAM Journal on Scientific Computing,* vol. 26, pp. 1340-1368, 2005.
[109] J. Brackbill, D. B. Kothe, and C. Zemach, "A Continuum Method for Modeling Surface Tension," *Journal of Computational Physics,* vol. 100, pp. 335-354, 1992.
[110] Y. Renardy and M. Renardy, "PROST: a parabolic reconstruction of surface tension for the volume-of-fluid method," *Journal of Computational Physics,* vol. 183, pp. 400-421, 2002.
[111] M. Meier, G. Yadigaroglu, and B. L. Smith, "A novel technique for including surface tension in PLIC-VOF methods," *European Journal of Mechanics-B/Fluids,* vol. 21, pp. 61-73, 2002.

[112] D. S. Kershaw, "The incomplete Cholesky—conjugate gradient method for the iterative solution of systems of linear equations," *Journal of Computational Physics,* vol. 26, pp. 43-65, 1978.

[113] W. Rider, D. Kothe, E. Puckett, and I. Aleinov, "Accurate and robust methods for variable density incompressible flows with discontinuities," in *Barriers and challenges in computational fluid dynamics*, ed: Springer, 1998, pp. 213-230.

[114] A. Y. Tong and Z. Wang, "A Numerical Method for Capillarity-Dominant Free Surface Flows," *Journal of Computational Physics,* vol. 221, pp. 506-523, 2007.

[115] M. Sussman and E. G. Puckett, "A Coupled Level Set and Volume-of-Fluid Method for Computing 3D and Axisymmetric Incompressible Two-Phase Flows," *Journal of Computational Physics,* vol. 162, pp. 301-337, 2000.

[116] A. Bourlioux, "A coupled level-set volume-of-fluid algorithm for tracking material interfaces," in *Proceedings of the 6th International Symposium on Computational Fluid Dynamics, Lake Tahoe, CA*, 1995.

[117] G. Son and N. Hur, "A Coupled Level Set and Volume-of-Fluid Method for the Buoyancy-Driven Motion of Fluid Particles," *Numerical Heat Transfer: Part B: Fundamentals,* vol. 42, pp. 523-542, 2002.

[118] G. Son, "Efficient implementation of a coupled level-set and volume-of-fluid method for three-dimensional incompressible two-phase flows," *Numerical Heat Transfer: Part B: Fundamentals,* vol. 43, pp. 549-565, 2003.

[119] M. Sussman, "A second order coupled level set and volume-of-fluid method for computing growth and collapse of vapor bubbles," *Journal of Computational Physics,* vol. 187, pp. 110-136, 2003.

[120] X. Yang, A. J. James, J. Lowengrub, X. Zheng, and V. Cristini, "An adaptive coupled level-set/volume-of-fluid interface capturing method for unstructured triangular grids," *Journal of Computational Physics,* vol. 217, pp. 364-394, 2006.

[121] D. B. Kothe, R. C. Mjolsness, and M. D. Torrey, *RIPPLE: A computer program for incompressible flows with free surfaces*: available to DOE and DOE contractors from OSTI, 1991.

[122] Z. Wang, "Numerical study on capillarity-dominant free surface and interfacial flows," 2007.

[123] F. Harlow and A. Amsden, "Fluid dynamics: A LASL monograph(Mathematical solutions for problems in fluid dynamics)," 1971.

Biographical Information

Yin Guan was born in Wuhan, China. He received his B.E. degree in Building Environment and Equipment Engineering from Huazhong University of Science and Technology, Wuhan, China, in June 2008. He entered The University of Texas at Arlington for his PhD study in Mechanical Engineering in August 2009. He received his PhD degree in May 2015. His research interests are computational fluid dynamics, electrowetting-based microfluidic droplet motions, free surface and interface tracking methods and surface tension modeling schemes.